Copyright Undertaking

This thesis is protected by copyright, with all rights reserved.

By reading and using the thesis, the reader understands and agrees to the following terms:

1. The reader will abide by the rules and legal ordinances governing copyright regarding the use of the thesis.
2. The reader will use the thesis for the purpose of research or private study only and not for distribution or further reproduction or any other purpose.
3. The reader agrees to indemnify and hold the University harmless from and against any loss, damage, cost, liability or expenses arising from copyright infringement or unauthorized usage.

IMPORTANT

If you have reasons to believe that any materials in this thesis are deemed not suitable to be distributed in this form, or a copyright owner having difficulty with the material being included in our database, please contact lbsys@polyu.edu.hk providing details. The Library will look into your claim and consider taking remedial action upon receipt of the written requests.

Pao Yue-kong Library, The Hong Kong Polytechnic University, Hung Hom, Kowloon, Hong Kong

http://www.lib.polyu.edu.hk

This thesis in electronic version is provided to the Library by the author. In the case where its contents is different from the printed version, the printed version shall prevail.

The Hong Kong Polytechnic University

Department of Applied Physics

Physical Properties of (Zn, Mg)O Thin Films and Related Heterojunctions

Wong Hon Fai

A thesis submitted in partial fulfillment of the

requirements for the degree of Master of Philosophy

September 2009

THE **H**ONG **K**ONG **P**OLYTECHNIC **U**NIVERSITY

Certificate of Originality

I hereby declare that this thesis is my own work and that, to the best of my knowledge and belief, it reproduces no material previously published or written, nor material that has been accepted for the award of any other degree or diploma, except where due acknowledgement has been made in the text.

____

Wong Hon Fai

Abstract

Transparent cubic phase $Mg_{0.5}Zn_{0.5}O$ (c-MZO) films of about 500 nm thickness were successfully fabricated on single crystal MgO(001) and LAO(001) substrates by Pulsed Laser Deposition (PLD) method. X-ray diffraction (XRD) studies showed that typical cube-on-cube epitaxy was obtained for c-MZO films grown on MgO substrate. Films deposited on LAO substrates, however, exhibited excellent epitaxy with 45° in-plane twisted relative to the substrate. Upon introducing an appropriate Indium (In) content, the optical bandgap energy of c-MZO films can be widely tuned from 6.17 to 4.29 eV. All In doped $Mg_{0.5}Zn_{0.5}O$ (IMZO) films displayed excellent optical transmittance of over 90 % for the whole visible spectrum, while the resistivity of these films can be brought down to 10^{-2} Ω-cm when alloyed with the In content of 0.18 in the target. Therefore, these IMZO films can be used as tunable UV filter and transparent conducting oxide (TCO) for various optoelectronics applications.

$Li_{0.15}Ni_{0.85}O$ (LNO) is a *p*-type TCO. Epitaxial and transparent IMZO based *p*-LNO/*n*-IMZO junctions were fabricated on MgO(100) substrate. They all have demonstrated good rectifying property at room temperature. Moreover, the temperature dependence of *I-V* characteristic showed that the current transportation mechanism of these heterojunctions was dominated by tunneling through the barrier or the generation-recombination process occurring in the depletion region. In the optical response measurement, responsivity of these photodetectors can be varied from 307 to 315 nm by changing the In content in the *n*-IMZO thin films. These results showed that such all-oxide heterojunctions with good electrical and optical properties are a promising material for optoelectronic applications.

The *p*-LNO/*n*-IMZO heterojunctions have been successfully integrated on TiN buffered Si substrate. These *p*-*n* junctions exhibited even better rectifying characteristics than those fabricated on MgO substrate, and their structural and electrical properties can be effectively tuned by bandgap engineering of *n*-IMZO. By increasing the In content in *n*-IMZO layer, electrical resistivity and bandgap are lowered. These can lead to higher current rectifying ratio, higher threshold voltage and higher leakage current in the bias voltage of -4V. Furthermore, heterojunctions grown on TiN buffered Si possess higher current rectifying ratio, lower series resistance and lower leakage current than those grown on MgO substrate. These results suggested that all-oxide *p*-LNO/*n*-IMZO heterojunctions can be integrated on Si with better electrical performances than those grown on MgO substrate.

Acknowledgements

I would like to express my sincere appreciation to my supervisor, Prof. K. H. Wong for his close guidance throughout these two years. His opinions help me through many difficulties in my study, research and even life. I specially thank Dr. C. W. Leung, Dr. C. L. Mak, Dr. Stephen Sin, Dr. Chingyee Lam, and Irene Pang gives me enlightening suggestions and discussions on my research works. Special thanks are also due to Dr. Hardy Lui for his help in the optical measurement. I would like to thank my research companions: Matthew Wong, Flora Ng, Willy Li, CK Lau, Victoria Li, Janet Ng, Alfa Lau, Dr. W. C. Liu and Y. B. Yao, for their useful suggestions. Finally, I would like to thank my parents for their patience and endless support throughout my life.

Table of Contents

Certificate of Originality i

Abstract ii

Acknowledgements iv

Table of Contents v

List of Figures ix

List of Tables xv

Chapter 1. Introduction 16

1.1. Background 16

1.2. Outline of thesis 18

1.3. Literature review 20

1.3.1. Crystal structure and lattice parameter of Zinc oxide 20

1.3.2. Physical properties of ZnO 20

1.3.3. Intrinsic defect and doping in ZnO 22

1.3.4. Bandgap engineering of ZnO based semiconductor 22

1.3.5. Structural and optical properties of MZO 25

1.3.6. Optoelectronic application of MZO 26

Chapter 2. Experimental Equipment 29

2.1. Pulsed Laser Deposition (PLD) 29

2.1.1. Introduction 29

2.1.2. Mechanism of PLD 29

2.1.3. Thin film growth modes 30

2.1.4. Epitaxial growth 31

2.1.5. PLD setup 32

2.2. Experiment procedure 34

2.2.1. Target fabrication 34

2.2.2. Substrate preparation 34

2.3. Structural measurement 34

2.3.1. Surface profiling 34

2.3.2. X-ray diffraction 35

2.3.3. Scanning Electron Microscope 37

2.3.4. Atomic Force Microscope 37

2.4. Electrical measurement 38

2.4.1. Temperature dependent resistivity 38

2.4.2. Current-Voltage measurement 39

2.4.3. Hall Effect Measurement 39

2.5. Optical measurement 41

2.5.1. Transmittance 41

2.5.2. Spectral response 42

2.5.3. Raman spectroscopy 44

Chapter 3. Bandgap engineering of IMZO films with different In content 46

3.1. Introduction 46

3.2. Experimental details 47

3.3. Structural properties 47

3.3.1. Structural properties of IMZO target 48

3.3.2. Structural properties and surface morphology of IMZO films 49

3.4. Electrical properties 55

3.5. Optical properties 57

3.6. Summary 60

Chapter 4. Structural, electrical and optical properties of IMZO films with different thickness 61

4.1. Introduction 61

4.2. Experimental details 62

4.3. Structural properties of IMZO films of different thickness 62

4.4. Electrical properties of IMZO films with different thickness 64

4.5. Optical properties of IMZO films with different thickness 66

4.6. Summary 68

Chapter 5. Structural, electrical and optical properties of LNO/IMZO heteroepitaxial junctions grown on MgO(100) substrates 69

5.1. Introduction 69

5.2. Structural, electrical and optical characterization of $Li_{0.15}Ni_{0.85}O$ 71

5.2.1. Structural characterization of LNO ceramics target 71

5.2.2. Deposition of LNO Layer 72

5.2.3. Structural characterization of LNO layer 73

5.2.4. Electrical and optical properties of LNO layer 75

5.3. Experimental details 77

5.4. Structural properties of heterojunctions grown on MgO substrates 79

5.5. Electrical properties of heterojunctions grown on MgO substrates 82

5.5.1. Temperature dependence of *I-V* characteristics 87

5.6. Optical properties of heterojunctions grown on MgO substrates 90

5.7. Summary 97

Chapter 6. Structural, electrical and optical properties of LNO/IMZO heteroepitaxial junctions grown on TiN buffered Si(001) substrates 98

6.1. Introduction 98

6.2. Experimental details 100

6.3. Characterization of TiN deposited on Si(001) substrates 102

6.3.1. TiN bulk Target 102

6.3.2. Structural properties and surface morphology of TiN film 103

6.4. Structural properties of heterojunctions on TiN buffered Si 105

6.5. Electrical properties of heterojunctions on TiN buffered Si 108

6.6. Optical properties of heterojunctions on TiN buffered Si 116

6.7. Summary 118

Chapter 7. Conclusion and Further Work 119

References 123

List of Figures

Fig. 1.1 The phase diagram of ZnO-MgO binary [1.30]. 23

Fig. 1.2 The bandgap and phase transformation of MZO films as a function of Mg content in the lattice of ZnO grown by using PLD method [1.33]. 23

Fig. 2.1 The three types of thin film growth mode: (i) Volumer-Weber growth or 3D Island growth mode, (ii) Frank-van der Merme or layer-by-layer growth mode and (iii) Stranski-Krastinov growth mode. 30

Fig. 2.2 Schematic diagram of Pulsed Laser Deposition (PLD) system. 33

Fig. 2.3 Schematic diagram of Alfa step profiler. 35

Fig. 2.4 Schematic diagram of resistivity measurement. 38

Fig. 2.5 Schematic diagram of the spectral response measurement. 43

Fig. 2.6 Energy level diagrams of Rayleigh scattering, Stokes Raman scattering, and anti-Stokes Raman scattering. 44

Fig. 3.1 XRD powder diffractions of IMZO targets with different In content (x) of 0, 0.04, 0.08, 0.16 and 0.18 respectively. 48

Fig. 3.2 XRD pattern θ-2θ scans of $Mg_{0.5}Zn_{0.5}O$ films deposited on: a) LAO(001), and b) MgO(001) substrates at 600°C with 3 x 10^{-5} Torr ambient pressure. 50

Fig. 3.3 Phi scans of the $Zn_{0.5}Mg_{0.5}O$ (202) and the LAO (202) reflections of the $Zn_{0.5}Mg_{0.5}O$ film on LAO substrate. 50

Fig. 3.4 XRD pattern θ-2θ scans of IMZO films deposited on MgO(001)

substrates with different In content (x) of 0.04, 0.08, 0.16 and 0.18 in the target. 51

Fig. 3.5 Lattice mismatch between IMZO and MgO, *a*-axis parameter and FWHM values of IMZO(002) with different In content (x) of 0.04, 0.08, 0.16 and 0.18 in the target. 51

Fig. 3.6 Phi scan of the IMZO(202) and the MgO(202) reflections of the IMZO film on MgO (001) substrate with x =0.18 in the target. 52

Fig. 3.7 AFM images of IMZO films with different In content (x): a) 0, b) 0.08, c) 0.16 and d) 0.18 in the target, measured over 3 x 3 μm^2 scanning size. 54

Fig. 3.8 Resistivity of IMZO films as a function of temperature for the In content (x) of 0.16 in the target. 55

Fig. 3.9 Electrical resistivity (ρ), Hall mobility (μ) and carrier concentration (n_e) of IMZO films as a function of In content (x) of 0, 0.04, 0.08, 0.16 and 0.18 in the target. 57

Fig. 3.10 Transmittance spectrum of IMZO films as a function of In content (x) in the target. 58

Fig. 3.11 The square of absorption coefficient versus photon energy for IMZO films with different In content (x) of 0, 0.04, 0.08, 0.16, and 0.18 in the target. 59

Fig. 4.1 XRD pattern θ-2θ scans of IMZO films (when x= 0.18 in the target) with various deposition times of 5, 7, 15, 30, and 45 min, which corresponded to the film thickness of 120, 193, 343, 555, and 943 nm respectively. 62

Fig. 4.2 FWHM of (002) rocking curves for IMZO films (when x= 0.18 in the target) with different thickness. 63

Fig. 4.3 Electrical resistivity (ρ), hall mobility (μ) and carrier concentration (n_e) with different thickness of IMZO films, when x=0.18 in the target. 64

Fig. 4.4 Optical transmittance spectra with IMZO films (x=0.18 in the target) as a function of film thickness. 66

Fig. 4.5 Relationship between the square of absorption coefficient (α^2) and photon energy (eV) of IMZO films with thickness. The inset is the optical bandgap as a function of film thickness. 67

Fig. 5.1 The X-ray diffraction pattern of densely sintered $Li_{0.15}Ni_{0.85}O$ ceramics target. 71

Fig. 5.2 X- Ray diffraction patterns for LNO films deposited on MgO(100) at 500°C with 100 mTorr oxygen pressure: (a) θ-2θ scan, (b) the rocking curve of (002) peak of LNO, (c) Phi scan measured from (202) LNO and (202) MgO. 74

Fig. 5.3 UV-visible transmission and absorption spectra of LNO film on MgO(100) substrate showing a strong absorption at 341nm. 76

Fig. 5.4 Schematic structure of LNO/ IMZO *p-n* heteroepitaxial diode. The red arrow is the current flow direction under forward bias voltage. 78

Fig. 5.5 X-Ray diffraction patterns for *p*-LNO/*n*-IMZO heterojunctions deposited on MgO(001) with different In content (x) in the target: (a) θ-2θ scan, (b) the rocking curve of (002) peak of LNO and IMZO when x=0.18, (c) Phi scan measured from LNO(202), IMZO(202) and MgO(202) when x=0.18. 81

Fig. 5.6 *I-V* curve of *p*-LNO/*n*-IMZO heterojunctions on MgO(001) substrate with different In content (x) a) 0.08, b) 0.16 and c) 0.18 in the target. 83

Fig. 5.7 *I-V* characteristics between the two platinum electrodes on the a) IMZO film with different In content (x) of 0.08, 0.16 and 0.18 in the target, b) LNO film. 84

Fig. 5.8 Forward bias Ln(*I*)-*V* curve of *p*-LNO/*n*-IMZO heterojunctions on MgO substrate. Exponential fit lines corresponding to ideality factor: in low voltage region: 2.54, 3.03 and 4.02; in large voltage: 95.3, 56.5 and 55.3 with different In content (x) of 0.08, 0.16 and 0.18 in the *n*-type layer (target). 86

Fig. 5.9 Current-Voltage characteristics of *p*-LNO/*n*-IMZO heterojunction as a function of temperature, when the In content (x) in the target is equal to 0.16. The inset is the plot of threshold voltage against temperatures. 88

Fig. 5.10 Leakage current at -5V and the ideality factor as a function of temperature. 89

Fig. 5.11 Optical transmittance spectra of *p*-LNO/*n*-IMZO heterojunctions with different In content (x) of 0.08, 0.16 and 0.18 in the target respectively. The inset is the configuration of front-side and back-side illumination. 90

Fig. 5.12 Optical transmittance spectra of *n*-IMZO film with different In content (x) in the target. 91

Fig. 5.13 Spectral responsivity of the *p*-LNO/*n*-IMZO heterojunctions on MgO substrate under back-side illumination when x=0.16 in the target. The corresponding Lorentzian fit peaks are 307, 330 and 375 nm respectively. The inset shows the spectral response of these heterojunction under front-side illumination. 92

Fig. 5.14 Quantum Efficiency of the *p*-LNO/*n*-IMZO heterojunctions on

MgO substrate under back-side illumination when x=0.16 in the target. 93

Fig. 5.15 Spectral responsivity of the *p*-LNO/*n*-IMZO heterojunctions on MgO substrate under back-side illumination when x=0.18 in the target. The corresponding Lorentzian fit peaks are 315, 343 and 402 nm respectively. The inset shows the spectral response of these heterojunction under front-side illumination. 95

Fig. 5.16 Quantum Efficiency of the *p*-LNO/*n*-IMZO heterojunctions on MgO substrate under back-side illumination when x=0.18 in the target. 96

Fig. 6.1 The schematic diagram of *p*-LNO/*n*-IMZO heterojunctions on TiN buffered Si. The arrow is the flow of the electron. 100

Fig. 6.2 The X-ray diffraction pattern of hot-press sintered TiN ceramics target. 102

Fig. 6.3 X- Ray diffraction patterns of θ-2θ scan of TiN deposited on Si(100) substrate. The inset is the rocking curve of (002) peak of TiN film. 103

Fig. 6.4 The SEM and AFM images of the surface morphology of TiN deposited on Si substrate. 104

Fig. 6.5 XRD for *p*-LNO/*n*-IMZO heterojunctions deposited on TiN buffered Si(001) with different In content of 0.08, 0.16 and 0.18 in the target: (a) θ-2θ scans, (b) the rocking curves of (002) peak of IMZO, TiN and LNO when x=0.18, (c) Phi scan measured from (202)LNO, (202)IMZO, (202)TiN and (404)Si when x=0.18. 106

Fig. 6.6 The lattice mismatch between LNO and IMZO, $f_{LNO \vartheta IMZO}$, and the 2 theta values of IMZO with different In content (x) in the target. 107

Fig. 6.7 *I*-*V* curve of *p*-LNO/*n*-IMZO heterojunctions on TiN buffered Si(001) substrate with different In content (x) 0.08, 0.16 and 0.18 in the target respectively. 108

Fig. 6.8 *I*-*V* characteristics between the two platinum electrodes on the IMZO film with different In content (x) in the target. 109

Fig. 6.9 The current rectifying ratio $\frac{I_{4v}}{I_{-4v}}$ of heterojunction fabricated on TiN buffered Si and MgO substrate with different In content (x) in the target. 110

Fig. 6.10 *I*-*V* curves of *p*-LNO/*n*-IMZO heterojunctions grown on TiN buffered Si(001) and MgO(001) substrate when x= 0.18 in the target. 111

Fig. 6.11 Threshold voltage (V_{th}) and leakage current (I_{leak}) in *p*-LNO/*n*-IMZO heterojunctions with different In content (x) of 0.08, 0.16 and 0.18 in the *n*-IMZO layer (target). 112

Fig. 6.12 Forward bias Ln(*I*)-*V* curves of *p*-LNO/*n*-IMZO heterojunctions on TiN buffered Si(001) substrates. Exponential fit lines corresponding to ideality factor: in low voltage region (red line): 2.31, 3.42 and 3.46; in large voltage (blue line): 11.83, 24.74 and 32.29 with different In content in the *n*-type layer (target). 114

Fig. 6.13 The ideality factor of the heterojunctions with different In content (target) grown on TiN buffered Si and MgO substrate, which are measured at high forward bias voltage. 115

Fig. 6.14 Spectral responsivity of the *p*-LNO/*n*-IMZO heterojunctions on TiN buffered Si substrate with x=0.08, 0.16 and 0.18 in the target. 116

List of Tables

Table 1.1 The fundamental properties of ZnO and GaN [1.15-1.17]. 21

Table 5.1 Resistivity, Hall mobility and carrier density for LNO films deposited on single crystal MgO substrate under the deposition conditions (T_s=500°C and Po_2=100 m Torr). 75

Table 5.2 Lattice mismatch between IMZO and LNO, 2 theta angle of LNO and IMZO for *p-n* heterojunctions with different In content (x) in the target. 81

Table 5.3 Threshold voltage, current rectifying ratio of +4 /-4 and the leakage current at -4V values for the heterojunction with different In content in the target. 84

Chapter 1. Introduction

1.1. Background

Silicon (Si) has been very useful for the development of microelectronics. It still dominates the present commercial market in integrated circuits for computing, data storage and communication. One limitation of these materials is that the bandgap is indirect. This implies that the emission and absorption coefficient of Si is very low when compared with other direct bandgap materials. Furthermore Si has a bandgap of only ~ 1 eV. It is clear that Si is undesirable for many important functions. For some optoelectronic applications, in particular, we need to turn to other materials. Oxide-based materials are promising semiconductors. They can be synthesized easily and possess excellent properties such as ferromagnetism [1.1, 1.2], superconductivity [1.3-1.5], photo-electricity [1.6] and high-k dielectricity [1.7]. Their bandgap values make them useful in high temperature/power electronics and UV light emitter diodes applications. Many oxide-based materials have bandgaps greater than 3 eV. They exhibit excellent properties such as higher optical transparency, higher stability and higher breakdown field strength. Therefore, they are suitable for robust electronic devices and short wavelength optoelectronics.

With a direct bandgap of 3.27eV and a high exciton blinding energy of 60 meV, ZnO has become a promising candidate for blue/UV light emitting diode, UV detector, transparent conducting oxide, piezoelectric transducer and more recently the ferromagnetic spintronics application [1.8, 1.9]. By alloying MgO with ZnO, the bandgap energy can be tuned from 3.34 to 6.8eV. Indeed, bandgap engineering of $Zn_xCd_{1-x}O$ and $Zn_xMg_{1-x}O$ (MZO) films has been demonstrated [1.10, 1.11]. Our goal is to fabricate c-MZO to form high quality *p-n* junction diodes on different substrates,

such as (100) oriented single crystal MgO substrate and TiN buffered Si substrates. Up-to-date *p*-type doping of ZnO or MZO remains an issue and homoepitaxial MZO *p*-*n* junction has not been realized. An alternative approach is to grow *n*-type MZO on other lattice matched *p*-type semiconducting oxides such as $Li_xNi_{1-x}O$ (LNO) to form heteroepitaxial junctions. TiN has a simple cubic structure with a lattice constant of 4.2 Å. In these respects, the cubic phase MZO is highly desirable.

Choopun *et.al* reported that phase transformation from hexagonal to a rocksalt simple cubic structure occurred in the MZO films grown by PLD technique with Mg content higher than 45% [1.12]. This structural change came about originally from the two phase structures of ZnO: wurtzite and cubic structure. Wurtzite ZnO is very stable in ambient pressure. In contrast, the cubic form of ZnO only exists under high pressure at 100 kbar or above [1.13]. Apparently the high concentration of cubic rocksalt MgO induces formation of the cubic ZnO phase. We also believe that epitaxial growth on appropriate lattice matched cubic phase single crystal substrate can also help to stabilize the cubic MZO under the normal ambient. We have successfully demonstrated single-phase domain matching growth of epitaxial cubic MZO films on $LaAlO_3$ substrates. Fabrication of high quality of cubic MZO films has the following advantages: i) it forms stable cubic crystalline structure with a lattice constant of 0.42 nm, which is a very convenient size for lattice matched heteroepitaxial growth of many oxides, such as perovskites and transition metal monoxides; ii) by varying the content of MgO, the bandgap of MZO films can be extended to deep UV range; iii) it can be doped with metals, such as In and Sn, to become TCO; iv) if the band-to-band transition of cubic MZO film is direct, c-MZO will become the premier photonic materials. The cubic structure of MZO provides the parallel set of crystal planes that allow the formation of natural optical resonator for laser. In hexagonal structure based GaN laser, mechanical

etching/polishing is required to produce the needed (parallel) resonator.

1.2. Outline of thesis

This thesis describes the experimental investigation of cubic phase MZO thin films deposited by PLD. The objectives of this research are to study the structural, electrical and optical properties of wide bandgap MZO films with cubic phase and to fabricate all oxide *p-n* junction diodes on (001) oriented single crystal MgO substrate and TiN buffered Si substrates using MZO as the active layer. Literature review on basic properties and the optoelectronic application of ZnO-based devices will be discussed after this section.

In Chapter 2 we provide brief information of the pulsed laser deposition system. We also describe the optical, electrical and structural characterization techniques, which were used in theses research. Furthermore, equipments such as X-Ray Diffractometer (XRD), Atomic Force Microscope (AFM), Scanning Electron Microscope (SEM), Current-Voltage characteristics, Hall Effect measurements, Transmittance and experimental setup for spectral response, are introduced.

In Chapter 3, we put our focus on the bandgap engineering of cubic phase In doped $Mg_{0.5}Zn_{0.5}O$ (IMZO) thin films grown on MgO (001) substrates. The systematic changes in the structural, electrical and optical properties of these films with different In content (target) in the IMZO films will be presented.

Chapter 4 deals with epitaxial IMZO film with cubic phase. High transparency and low resistivity arise from different film thickness as well as detail discussion in the structural, electrical and optical properties.

Fabrication and characterization of all-oxide *p*-LNO/*n*-IMZO heterojunctions with bandgap engineering of IMZO grown on MgO substrate is described in Chapter 5. The heterojunctions exhibited good rectifying *I-V* characteristics in different samples. Due to the wide bandgap of LNO and IMZO, UV response of these heterojunctions under front and backside illumination was examined. We demonstrated that structural, electrical and optical properties of the *p*-LNO/*n*-IMZO heterojunctions can be tuned under different In content in the *n*-type layer. We conclude that the IMZO based heterojunctions are promising candidates for optoelectronic applications.

Chapter 6 concerns with the characterization of *p*-LNO/*n*-IMZO heterojunctions integrated with TiN buffered Si substrates. Comparison between the *p-n* junction grown on MgO and those on TiN buffered Si has been made. We report that the *p*-LNO/*n*-IMZO heterojunctions can be satisfactorily integrated with Si substrate while retaining excellent electrical properties and low leakage current.

The present experimental results and the important findings are summarized in Chapter 7. In view of the successes of IMZO thin film and IMZO based *p-n* junction, as demonstrated in our work, suggestions for future work are provided.

1.3. Literature review

These sections introduce a review of the general properties of ZnO, including its crystal structure and other physical parameters. The basic concept of bandgap engineering and optoelectronic properties of ZnO-based semiconductor will also be discussed.

1.3.1. Crystal structure and lattice parameter of Zinc oxide

Under ambient pressure and temperature, ZnO crystallizes into hexagonal lattice of space group $P6_3m$. The zinc atoms are surrounded by four oxygen atoms with the tetrahedral configuration. This coordination originates from the polar symmetry of hexagonal axis, which is responsible for different attractive properties in ZnO materials, such as piezoelectricity, and spontaneous polarization. This wurtzite structure of ZnO has a lattice constant of a = 3.2495 Å and c = 5.2069 Å with a density of 5.605 gcm^{-3}[1.14].

Besides the hexagonal structure, a metastable cubic phase with the rocksalt structure of space group F*m3m* is known. At a high pressure of 100 kbar at 300K, a phase transition from hexagonal wurtzite to cubic structure of ZnO that exhibits the rocksalt (NaCl) occurs [1.13]. These cubic structure have lattice constant a = 4.2Å. Upon decreasing pressure, this phase transition is reversible at a certain pressure which is temperature dependent. It is concluded that cubic phase ZnO is not stable at ambient pressure.

1.3.2. Physical properties of ZnO

Table 1.1 lists the physical parameters of ZnO and GaN semiconductors [1.15-1.17]. Both ZnO and GaN are of wurtzite structure with direct bandgap of about 3.5 eV. For device community, GaN is lack of native substrate and lattice-matched substrates, which is an obstacle for the development of high quality UV detector, laser and

high-power electronic devices. Nowadays, most GaN devices are grown on (0001) sapphire substrates and need to cope with a 16% lattice mismatch [1.18], which results a dislocation density as high as 10^7-10^8 cm^{-2}. This high dislocation density will shorten the life-time of GaN based devices. However, ZnO substrate is a good candidate for epitaxial growth of GaN because of a 2 % lattice mismatch only. High quality, epitaxy and low dislocation defect GaN has been successfully fabricated on (0001) ZnO substrate via MBE. These approaches make ZnO an attractive alternative to sapphire substrate for fabrication of high quality optoelectronic devices.

Table 1.1The fundamental properties of ZnO and GaN [1.15-1.17].

Material	ZnO	GaN
Lattice constant (Å)	a_0 =3.2495	a_0 =3.189
	c_0 =5.5069	c_0 =5.185
Density (g cm^{-3})	5.61	6.15
Melting point (K)	2250	2770
Thermal conductivity (Wcm^{-1} K^{-1})	0.6	1.3
Thermal expansion coefficient	a_0 =6.50	a_0 =5.59
(μK^{-1})	c_0 =3.00	c_0 =7.75
Bandgap energy (eV)	3.37 (direct)	3.39 (direct)
Index of refraction	2.33	1.85
Saturation velocity (cm s^{-1})	3.0 x 10^7	2.5 x 10^7
Breakdown voltage(V cm^{-1})	5.0 x 10^6	5.0 x 10^6

Moreover, many scientists have recognized the potential for ZnO as a promising material to replace GaN for optoelectronics industries. The exciton energy of ZnO is 60

meV whersa that of GaN is 25 meV. In principle, the higher exciton energy of ZnO enhances the luminescence efficiency of the excitonic recombination, thus reduces the power threshold for optical pumping at the room temperature. P.Yu *et al.* have reported UV laser emission from ZnO thin films at room temperature [1.19]. The electron Hall mobility of single crystal ZnO is slightly lower than that in GaN, but ZnO possess a higher saturation velocity. The better radiation resistance capability of ZnO-based devices also helps to promote ZnO for space and harsh environmental applications.

1.3.3. Intrinsic defect and doping in ZnO

Undoped hexagonal phase ZnO has been found to be *n*-type semiconductor with electron carrier concentration about 10^{16} cm^{-3}. The conduction mechanism in undoped ZnO has been widely studied [1.20-1.22]. Kohan *et al.* showed that theoretically oxygen vacancies (V_O) and Zn interstitial (Zn_I) acts as deep donors, rather than shallow donors [20]. Therefore, ZnO exhibits intrinsic *n*-type conduction and difficult to be doped by intrinsic acceptor defects. For cubic phase ZnO, there are lack of experimental and theoretical studies in these aspects.

1.3.4. Bandgap engineering of ZnO based semiconductor

Bandgap engineering of semiconductor is an important step in optoelectronic applications. By alloying different semiconductor of different bandgap with basic materials, the bandgap of these alloys can be tuned, thus the structural, electrical and optical properties can be changed. In ZnO system, alloying with MgO and CdO can be effectively tuned the bandgap from deep UV to visible range [1.23, 1.24]. Ohtomo *et al.* [1.24], Minemoto *et al.* [1.25], Narayan *et al.* [1.26] and Park *et al.* [1.27] demonstrated that the bandgap engineering of MZO are useful for the optoelectronic application. The performance of optoelectronic devices can be remarkably enhanced when using ZnO

and MZO based quantum well and superlattice structure. Indeed, the ZnO based heterostructure has been widely studied [1.28].

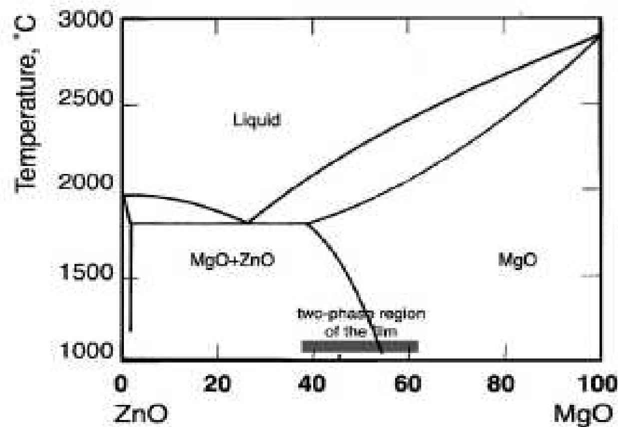

Fig. 1.1 The phase diagram of ZnO-MgO binary [1.30].

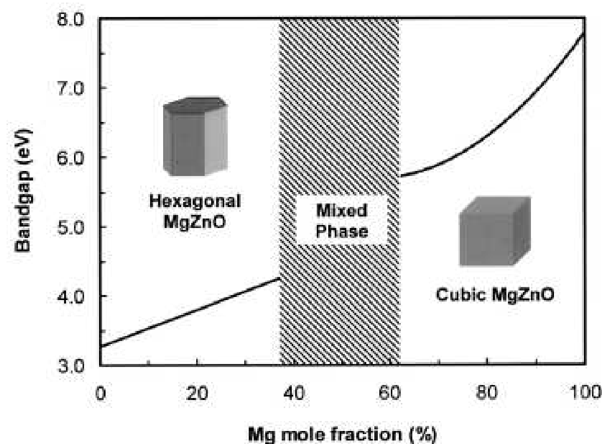

Fig. 1.2 The bandgap and phase transformation of MZO films as a function of Mg content in the lattice of ZnO grown by using PLD method [1.33].

The lattice structure of ZnO is hexagonal, while MgO has a NaCl type of rocksalt cubic structure. However, the similar ionic radius between Zn^{2+} (0.60 Å) and Mg^{2+} (0.57 Å) allows substitution for each other [1.29]. According to the phase diagram of the ZnO-MgO binary diagram as shown in Fig. 1.1, the thermodynamics solubility limit of MgO in ZnO is less than 4% [1.30]. However, Ohtomo et *al.* has demonstrated that

using PLD method, $Zn_{1-x}Mg_xO$ (MZO) binary films can be grown on quartz substrates with Mg content up to 33%, achieving a bandgap of 3.99 eV with a linear shift relationship between the bandgap of MZO and composition of Mg [1.24]. These films maintain favorable optical characteristics of wide bandgap materials, such as excellent transparency in the visible range and high exciton energy. A complete mapping of the phase transition in MZO alloys system has been reported. Figure 1.2 shows the bandgap and phase transformation of MZO as a function of Mg content in the films prepared by PLD methods. The crystallographic structure of $Mg_xZn_{1-x}O$ alloys can be tuned from wurtzite phase of ZnO for a low value of x to the cubic phase of MgO (x>60) by changing the Mg content. The MZO films with composition range of 0.37<x<0.6 exhibit intermediate phase, in which both cubic and wurtzite phases coexist. In this phase segregation, the nano-grains of cubic MZO phase embedded in the host matrix of wurtzite MZO is observed [1.31]. The bandgap can not be well defined in this region due to the phase segregation of cubic and hexagonal MZO, which is called as metastable phase region. We also believed that epitaxial growth on appropriate lattice matched cubic phase single crystal substrate can also help stabilize the metastable MZO films with cubic phase only under the normal ambient with high Zn content. We have successfully demonstrated single-phase domain matching growth of epitaxial cubic MZO films on $LaAlO_3$ substrates [1.32]. A non-linear increase of the bandgap in the form from 5.4 to 7.8 eV with x>0.62 are reported in the cubic phase region. The virtual crystal approximation of bandgap energy of hexagonal and cubic phase can be expressed as [1.12]:

$$E_g(Mg_xZn_{1-x}O) = 4.63x+3.27 \quad (\text{For hexagonal phase}, \ 0 \le x \le 0.33)$$

$$E_g(Mg_xZn_{1-x}O) = 4x+3.2 \quad (\text{For cubic phase}, \ 0.62 \le x \le 0.80)$$

The tuning of composition (bandgap) of the MZO alloys films was accomplished by controlling the content of ZnO and MgO in the ceramics target [1.12, 1.33]. MZO alloys films were prepared by PLD on (0001) sapphire substrate using the $Zn_{0.5}Mg_{0.5}O$ target at substrate temperature ranging from room temperature to 750°C. A linear relationship between the substrate temperature and the content of Mg in MZO films was observed. For room temperature deposition, the composition of the MZO alloy films was close to the target composition. It was noted that at high substrate temperature, the relative Zn content decreases. This is due to the fact that the vapor pressure of Zn is larger than those of Mg. The Zn atoms can easily escape from the surface of MZO films. Tunable bandgap from 5 to 6 eV in epitaxial MZO films with single cubic phase was achieved by controlling the deposition temperature. For metastable MZO films subjected to a rapid thermal annealing at 750°C for 1 min, two absorption edges at 350 and 250nm were observed. They are due to the phase segregation between cubic phase of MgO and hexagonal phase of ZnO in the MZO alloy films.

In 2001, J. Narayan *et al*. demonstrated that epitaxial growth of cubic phase MZO was successfully fabricated on TiN buffered Si substrate by PLD. These works have paved the way that cubic phase MZO with excellent transparency can be completely integrated with Si [1.34]. This simple cubic structure of MZO with bandgap value larger than 4 eV is a promising semiconductor, which is a premier material for the development of electronic and optoelectronic application such as UV laser, light emitting diode(LED), deep UV detector and transparent conducting oxide(TCO).

1.3.5. Structural and optical properties of MZO

Ohtomo *et al.* studied high quality and single hexagonal phase of MZO films on sapphire substrate at 600°C, and reported a trend of increase of *a*-axis length, and

decrease of *c*-axis length with Mg content up to 33%. These changes in lattice constant are due to the substitution of Mg into the lattice of ZnO. The near band emission in photoluminescence peak in 4.2K was found to shift from 3.36 to 3.87 eV with Mg content up to 33%. They are consistent with the estimated bandgap values obtained from transmittance measurements [1.24]. Schmidt *et al.* studied the wurtzite MZO film using ellipsometry for photon energy from 1 to 5eV and reported the bandgap increases from 3.369 to 4.101 eV with Mg content from 0 to 29%. Moreover, the exciton energy decreases from 60(x=0) to 50 meV(x=0.17) and increases to 58 meV(x=0.29) [1.35].

1.3.6. Optoelectronic application of MZO

With a direct bandgap of 3.27eV with a high exciton blinding energy of 60 meV, ZnO, will be an important material for the development of optoelectronic devices such as UV detector, UV and visible LED. ZnO-based materials have some advantages over GaN. Different fabrication techniques such as magnetron sputtering, PLD, e-beam evaporation and hydrothermal methods, have been successfully demonstrated to fabricate high quality ZnO films. However, high quality GaN films can only be fabricated by MOCVD. Moreover, the larger excitonic energy and the ability to grow on native substrates make ZnO based materials become promising materials in the development of devices for operation under a harsh and high temperature environment. In 2000, Ohta *et al.* first demonstrated that a UV light was emitted from *p*-$SrCu_2O2$/*n*-ZnO heterojunctions. A sharp emission band at 382 nm was generated under a forward bias exceeded the turn-on voltage [1.36]. And P. Chen *et al.* demonstrated that *n*-ZnO/p^+-Si heterojunction was electroluminescent to a UV light due to the defect related emission [1.37]. Moreover, Sun *et al.* has demonstrated the ZnO/Si based heterostructure can be electroluminescent with a wide emission ranging from 350 to 850 nm [1.38]. The above results have proved that ZnO-based semiconductor is a

promising candidate for developing of low cost and high performance of LED integrated with Si.

UV photodetector based on wide bandgap semiconductors, such as ZnO have been widely studied because the extensive application in civil and military areas. The advantage of ZnO based UV photodetector is that the UV/visible rejection ratio is much larger than narrow bandgap semiconductor, such as Si (E_g=1.12eV). However, the photodetector based on ZnO/Si diode can be used to sense both UV and visible radiation, via controlling the polarity of the voltage applied on the heterojunction [1.39-1.41]. These results indicate that the peak optical response of this heterojunction is 350nm, which corresponds to band-to-band transition of ZnO.

For photodetector working in the solar-blind spectral range (220-280 nm), MZO alloy photodetector possess unique figure of merits, such as availability of lattice-matched substrate (cubic and hexagonal phase of MZO), tunable bandgap energy from 3.3 to 7.8 eV and low fabrication temperature. For hexagonal phase MZO based photodetector, Yang and Vispute *et al.* reported that UV photodetector based on epitaxial $Mg_{0.34}Zn_{0.66}O$ film grown on sapphire substrate can be prepared by PLD. A high responsivity of 1200A/W under photoconductive mode can be achieved at 308 nm with the maximum UV/visible rejection ratio of about 4 orders of magnitude [1.42]. In order to further approach the solar blind region, the cubic MZO are more favorable due to tunable bandgap from 4 to 5 eV, with different Mg content in the cubic MZO films. Yang *et al.* first proposed that metal-semiconductor-metal (MSM) structured cubic MZO grown on Si substrate can be operated at 230nm, but the UV/visible rejection ratio is about one order of magnitude, revealing that the performance of these cubic MZO based photodetector has lots of room to be improved [1.33]. Recently, Ju *et al.*

demonstrated that MSM structured cubic MZO solar blind photodetector can be prepared by MOCVD. Upon varying Mg content, the cut-off wavelength of the photodetector can be covered from 225 to 287 nm. The UV/visible rejection ratio of about 4 orders of magnitude and a dark current of 15 pA under 10 V bias were reported in this photodetector [1.43].

Chapter 2. Experimental Equipment

2.1. Pulsed Laser Deposition (PLD)

2.1.1. Introduction

The Physical Vapor Deposition (PVD) techniques can be divided into four categories: evaporation, sputtering, cathodic arc deposition and pulsed laser deposition (PLD). The deposition process can be considered to have four stages: (1) The deposition materials are converted into physical vapor forms; (2) the vaporized atoms or molecules are transported to the substrate with minimal collisions from other gas atoms or molecules; (3) the condensation of a vapor onto the substrate. (4) the nucleation and growth of film on the substrate surface. Among all the PVD, PLD has some unique advantages over other deposition techniques. For example, PLD can be utilized to fabricate high quality epitaxial oxide films at a relatively low deposition temperature (500-600°C). Thin films of high Tc superconducting oxides [2.1], nitride [2.2], ferroelectric [2.3], metallic multilayers and various superlattices [2.4] have been realized by these methods.

2.1.2. Mechanism of PLD

The basic principle of PLD is that high energy laser pulses strike on the desired target under desired vacuum pressure. The strong absorption of electromagnetic radiation by the target leads to rapid congruent evaporation, which consist of highly stoichiometric species. These evaporated species will form a plasma plume that contains a mixture of energetic species including atoms, molecules, ions, electrons and large particulars. The plume rapidly expands and the ablated materials finally deposit on the substrate surface.

2.1.3. Thin film growth modes

A lattice mismatch and surface energy between substrate and film materials is a key parameter to determine the growth mode. Generally in heteroepitaxy, growth mode can be classified into three categories, as shown in Fig 2.1.

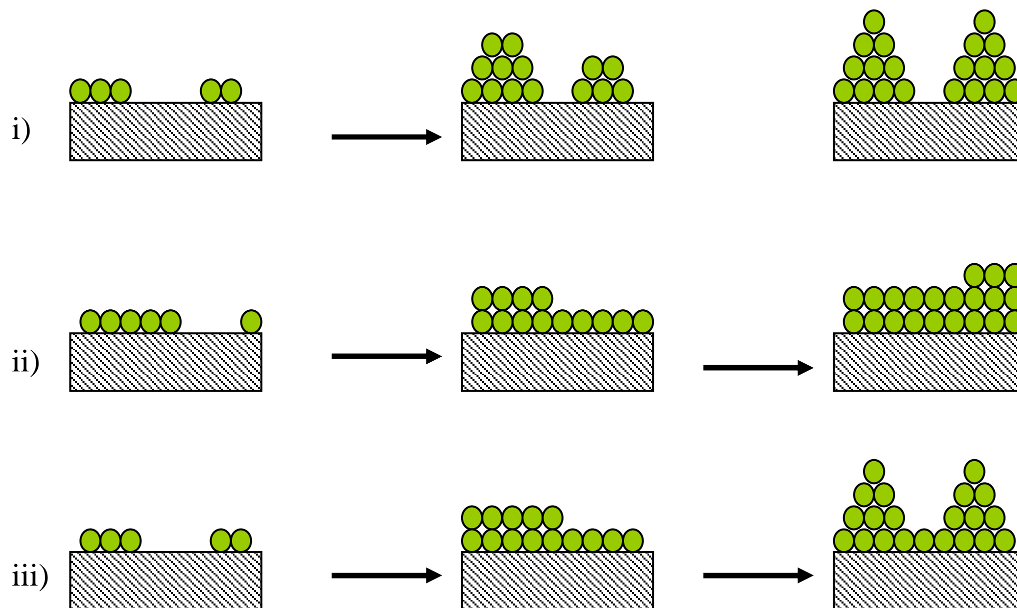

Fig. 2.1 The three types of thin film growth mode: (i) Volumer-Weber growth or 3D Island growth mode, (ii) Frank-van der Merme or layer-by-layer growth mode and (iii) Stranski-Krastinov growth mode.

They are: (i) Volumer-Weber growth or 3D island growth involving the film materials being formed as isolated island on the substrate. It is because the interatomic interactions between different atomic species of the film material are stronger than those between the substrate and film materials; (ii) Frank-van der Merme or layer-by-layer growth mode involving the interatomic interactions between substrate and the film materials are stronger than those between the different atomic species of the film. Full coverage monolayer growth is preferred and excellent epitaxy can be obtained; (iii) Stranski-Krastinov growth mode involving a combination of layer by layer mode and

3D island growth modes. Full-monolayer growth mode is dominated at the early stage. The lattice mismatch between the film materials and substrate will revert to the formation of 3D islands as few monolayers are formed.

2.1.4. Epitaxial growth

Epitaxy (the Greek-term meaning to "arrange upon") is a recrystallization process in which the crystal symmetry and in-plane lattice constant of the film materials have significantly influenced by the substrate. Generally the epitaxial growth can be classified into two categories. These are: (1) Homoepitaxial growth in which the material of film is the same as the substrate. It has been applied to grow different layers of different dopants or dopant concentrations. (2) Heteroepitaxial growth in which the film and substrate are of different materials, such as the $Mg_xZn_{1-x}O$ film grown on Sapphire substrate. The crystal symmetry of film and substrate should be similar in order to form a desired crystalline structure. The crystalline of films can be greatly influenced by these several factors.

In-plane lattice constant matching between the film and substrate is also an important parameter to warrant an epitaxial growth. The lattice mismatch f can be quantified as:

$$f = \frac{a_{film} - a_{substrate}}{a_{substrate}}; \qquad (2\text{-}1)$$

where a_{film} and $a_{substrate}$ are the lattice constants of the substrate and the film respectively. This lattice mismatch should be as small as possible in order to reduce the strain and dislocation at the interfaces. In the case of large lattice mismatch, in-plane orientation of the film is rotated with respect to that of substrate. This rotation can remain the films

remain quasi-epitaxial.

Similar thermal expansion coefficient of the film and the substrate materials are another criterion to form a good epitaxial film. The total strain in the films can be divided into three factors: intrinsic strain during growth, transformation strain, and strain induced by the mismatch from thermal expansion coefficient. Normally, the resultant strain will be dominated by thermal expansion coefficient, and can be defined as

$$\sigma_{th} = \frac{E_f}{1-v_f}\varepsilon_{th} = \frac{E_f}{1-v_f}\int_{T_o}^{T}(\alpha_f - \alpha_s)dT \ ; \qquad (2\text{-}2)$$

where E_f is the film Young's modulus, v_f is the Poisson ratio, α is the thermal expansion coefficient and T represents the temperature. When the resultant strain is greater than the elastic limit of the film, the relaxation of strain simultaneously affects the surface morphology of this film.

2.1.5. PLD setup

The schematic diagram of the PLD system in our laboratory, which is used for the growth of MZO films, is shown in Fig 2.2. A KrF Excimer laser with 248 nm wavelength is employed. This system consists of a simple vacuum chamber with rotary pump and diffusion pump. It can be evacuated to a base pressure of 6 x 10^{-6} Torr. Pressure of the chamber is monitored by an ionization gauge (ULVAC 122A). A 25 mm diameter ablation target is mounted on the target carrousel with smooth rotating speed. The laser windows and focusing lens were made of UV-grade fused silica (transmittance about 90%) of 248nm wavelength. The laser fluence of about 4 Jcm^{-2} is irradiated on the target with incident angle of 45°. A stable substrate heater capable of

heating the substrates up to 750 ^{o}C (few mTorr to 10^{-5} Torr) was used. The flat platform of the substrate heater is placed parallel to the target surface at a desired distance (4 cm). The substrate temperature is measured by a K-type thermal couple (Nickel-Chromium, Nickel-Aluminum) embedded underneath the face plate of the substrate holder. Tiny substrate (1cm^{2}) can be easily fixed onto the substrate heater using a conducting silver epoxy, which provides a good thermal conduction and adhesion between the substrate and the heater.

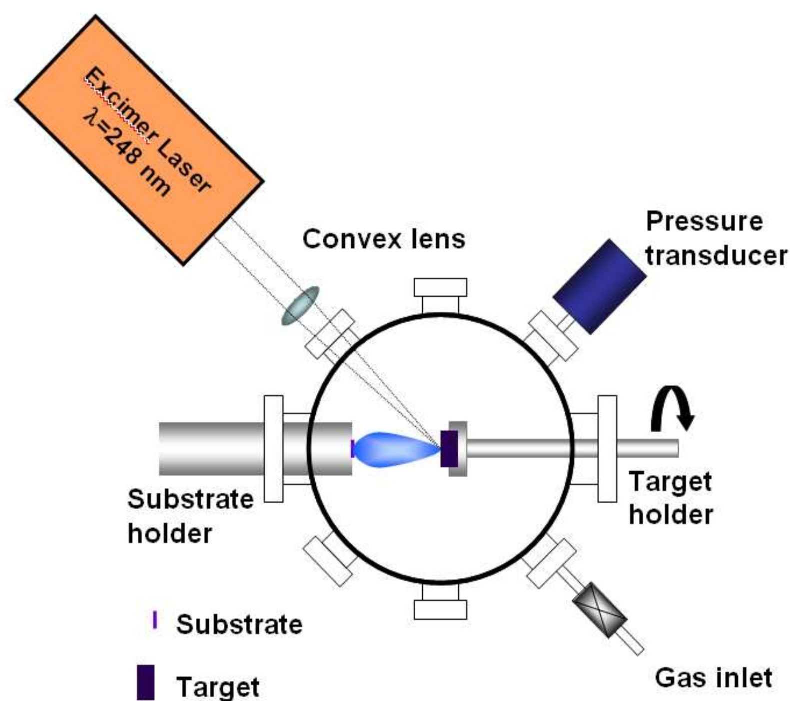

Fig. 2.2 Schematic diagram of Pulsed Laser Deposition (PLD) system.

2.2. Experiment procedure

2.2.1. Target fabrication

Oxide-based ceramic targets for pulsed laser ablation were prepared by conventional solid state reaction. Proper amount of constituent oxides were weighed, mixed and grounded by ball milling for 6 hours. The lengthy ball milling is an important step to obtain a homogenous solid solution. Calcinations for 10 hours in air were carried out in order to get rid of the organic component from mixed powder and initiate the chemical reaction between the mixed oxides. The calcined powder was re-grounded, and was compressed into pellets of 2.5 cm in diameter. Finally, these pellets were sintering for 10 hours in air in order to increase the density of the oxide-based ceramics target.

2.2.2. Substrate preparation

Prior to loading into the vacuum chamber, single crystal of $LaAlO_3$ (LAO), Al_2O_3, MgO and Si substrates were ultrasonically cleaned with acetone and then ethanol. For Si substrate, the native oxide is an obstacle to fabricate high quality and epitaxial thin films on Si substrate. 10% HF was employed to remove these native oxides.

2.3. Structural measurement

2.3.1. Surface profiling

The surface profiler machine (Alpha step profiler, Tencor Instrument, model P-10), shown schematically in Fig.2.3, was employed to determine the thickness of thin films. The working principle of these Alfa step profiler is that the needle probe with diameter of 10μm is scanned through the step. Film thickness can be determined by the height of this step. Generally, the resolution of this thickness can be as small as 1 nm. SEM image of the cross-section of the film will be employed to confirm the accuracy of this

thickness measurement.

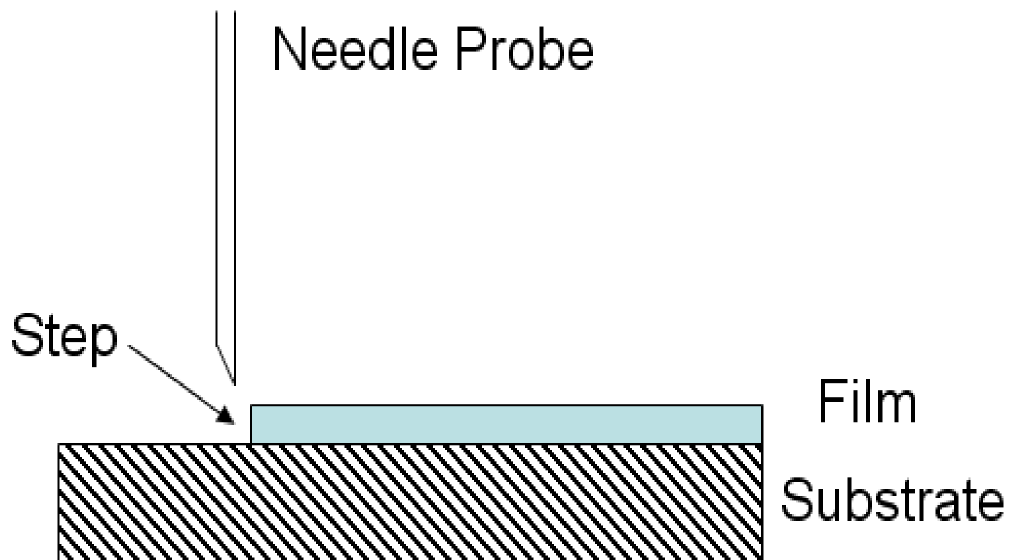

Fig. 2.3 Schematic diagram of Alfa step profiler.

2.3.2. X-ray diffraction

X-ray diffraction (XRD) is a non-destructive technique which reveals information regarding unit cell dimensions, crystalline and phase identification of materials. The structural properties of MZO thin films and targets are characterized by a Bruker D8 Discover and a Philip X'pert x-ray diffractometer in a four-circle mode. The x-ray source gives out K_α radiation of Cu at wavelength of 1.54 Å. The K_β emission at wavelength of 1.39 Å is blocked by a Ni filter.

The working principle of XRD is that a parallel monochromatic x-ray beam is impinged on a testing sample, a portion of beam will be scattered by the crystal plane of the sample, which will interfere with one and other to form diffraction centers and constructive interferences in certain angles. This constructive diffraction interference of

the sample should obey the Bragg's Law;

$$2d_{hkl}\sin\theta = n\lambda \tag{2-3}$$

where n is an integer , d_{hkl} is the inter-planar spacing, θ is the angle of diffracted beam, λ is the wavelength of the incident x-ray beam. For a material with a cubic structure, the inter-planar spacing can de deduced from this equation:

$$d_{hkl} = \frac{a}{\sqrt{h^2 + k^2 + l^2}} \tag{2-4}$$

where h, k and l are the Miller indices.

Generally, we will perform three different scan modes in XRD for characterization of the crystal structure of thin films. These are (1) θ-2θ scan mode to identify the crystalline phases and orientation of the film; (2) ω scan, in which the x-ray source and detector are fixed at a selected diffraction peak; and the sample is rocked a few degrees about the ω scan, to obtain a measure of the crystallities from the full width half maximum (FWHM) in the rocking curve, and (3) 360° φ scan to study the in-plane alignment of films relative to the substrate. For the case of cubic structure with (002) plane, it can be done by fixing θ and 2θ angles corresponding to (202) plane and setting φ value to 45°. Cubic structure will display four-fold symmetry with separation 90° in the 360°φ scan. If the four characterized peaks of the film coincide with those four of the substrate, it is the so-called 'cube-on-cube epitaxy'.

2.3.3. Scanning Electron Microscope

Scanning Electron Microscope (SEM) is a high resolution electron microscope that images the specimen's surface. A high energy beam of electrons is scanned over the sample in a raster scan pattern. As the electrons interact with the specimen, they produce secondary electrons, back-scattered electrons, auger electrons, x-ray and etc. By collecting the signal from secondary electrons, high resolution images of specimen can be obtained. Back-scattered electron images can provide information about the distribution of elements in the specimen. And the collection of x-rays is used to give information in the composition of specimen.

In this project, target composition, surface morphology and the cross-section image of thin films are characterized by JSM-6335F Field Emission Scanning Electron Microscope.

2.3.4. Atomic Force Microscope

Atomic force microscope (AFM) is a non-destructive technique that can be used to measure the surface roughness on a scale from angstroms to 100 microns, more than 1000 times better than the optical diffraction limit. The basic principle of AFM is to image surface topologies by a microscale cantilever with a tip. The topographic image of the surface is recorded while the tip is scanned repeatedly across the sample. In this project, the surface roughness of thin films is examined by trapping mode of a Digital Instruments, Nanoscope IV AFM.

2.4. Electrical measurement

2.4.1. Temperature dependent resistivity

The experimental setup for measuring the resistivity of MZO films is shown in Fig. 2.4. Due to the high resistivity of sample (few MΩ), two point probe is adequate to obtain accurate measurements. Two strips of platinum electrode are deposited on the surface of the films. The resistivity of the film can be obtained by the equation:

$$\rho = R\frac{d \times W}{L} \tag{2-5}$$

where d is the thickness, W is the width and L is the length of the film, R is the resistance of the films. For Resistance-Temperature measurement, the samples were placed inside a close-cycled helium cryostat. The cooling and heating rates, adjusted by a temperature controller (Lake Shore 321), were set at 10 K/min over a temperature range from 60 to 380 K. The resistivity measurement is monitored by the Labview software program.

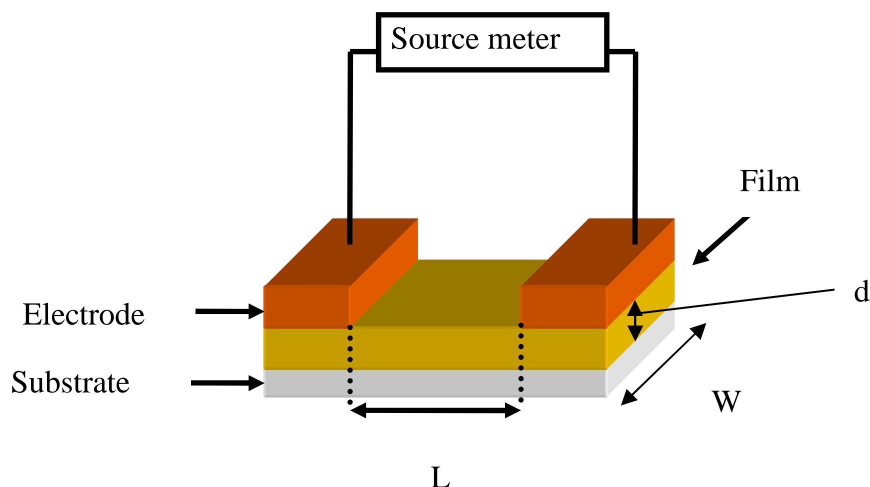

Fig. 2.4 Schematic diagram of resistivity measurement.

2.4.2. Current-Voltage measurement

Current-Voltage (*I-V*) measurement is a useful technique to study the transport properties of a electronic device. In this study, *I-V* measurements of all oxide based *p-n* junctions are evaluated by the Keithley 2400 and 6517A electrometer. The results allow us to deduce the ideality factor, series resistance and leakage current of the devices.

2.4.3. Hall Effect Measurement

The electrical properties of PLD grown In doped MZO thin films on MgO(001) substrate were examined using Hall Measurement. Resistivity, sheet carrier concentration and Hall mobility of thin films are measured by a Bio-rad HL5500PC Hall effect measurement system with four probe stations. The permanent magnet is installed in the system and is calibrated by the manufacturer with nominal field $0.32T \pm 0.1\%$.

Hall Effect measurement commonly uses two sample geometries: (1) long, narrow bar geometries and (2) nearly circle and square Van Der Pauw configuration. For simplicity and accuracy of these measurements, Van Der Pauw arrangement is probably the most convenient hall measurement geometry that allows us to obtain information of sheet resistivity, sheet Hall coefficient, sheet carrier concentration and Hall mobility of the semiconducting sample. In our experimental arrangement for the Van Der Pauw technique we used is square geometry. A small size of metal electrode is deposited at the corner of the films. The resistivity of a Van Der Pauw sample is given by the expression:

$$\rho = \frac{\pi \cdot t}{2 \cdot \ln(2)} \cdot \left[\frac{V_{43}}{I_{12}} + \frac{V_{23}}{I_{14}} \right] \tag{2-6}$$

where V_{23} is defined as V_2 - V_3 and I_{12} indicates the current enters the sample through contact 1 and leaves through contact 2, t is the thickness of the active layer

The sheet Hall coefficient is defined as:

$$R_{Hs} = \frac{V_h}{I \cdot B} \quad (m^2/C) \tag{2-7}$$

where V_h is the averaged value for all possible permutations of the contacts applied current and directions of magnetic field.

The sheet carrier concentration is defined as:

$$N_s = 1/q \cdot R_{Hs} \quad (cm^{-2}) \tag{2-8}$$

If the thickness of the film (t) is known, the carrier concentration and sheet resistivity can be calculated from $N = N_s/t$ and $\rho_s = \rho/t$ respectively. Finally, once the sheet resistivity is known, the Hall mobility is given by:

$$\mu_H = R_{Hs}/\rho_s \left(cm^{-3}/V \cdot s\right) \tag{2-9}$$

2.5. Optical measurement

2.5.1. Transmittance

The transmission spectra of the films can be obtained by UV-2550 UV-VIS Spectrophotometer, which is equipped with two continuous light sources: halogen lamp and deuterium lamp. These two light sources can provide a continuous spectrum from 190 to 900 nm. The working principle of this spectrometer is that when an incident light beam approaches a medium, a part of the light beam will be reflected by the medium, part of the light beam will be transmitted through the medium, and the rest of the beam will be absorbed. Absorption of photons arises due to the transition of the electrons from valence band to conduction band. Absorption coefficient α for a uniform medium can be defined as the intensity change of a monochromatic light beam in unit distance:

$$\frac{dI(\lambda)}{dx} = -\alpha(\lambda)I(\lambda) \qquad \text{(2-10)}$$

So the beam intensity as a function of distance x can be defined as:

$$I(\lambda) = I_0(\lambda)e^{-\alpha(\lambda)x} \qquad \text{(2-11)}$$

Assume there is no reflection from the medium, the transmittance $T(\lambda)$ is defined as the ratio of the intensity of the transmitted beam to that of the incident beam:

$$T(\lambda) = \frac{I(\lambda)}{I_0(\lambda)} \qquad \text{(2-12)}$$

where I and I_o are the intensities of the transmitted beam and incident beam respectively

So, the absorption coefficient can be deduced as:

$$\alpha(\lambda) = \ln(1/T)/d \tag{2-13}$$

where d is the thickness of the sample. Once the thickness of sample is known, the absorption coefficient can be obtained. The optical absorption coefficient is one of the simple and useful tools for understanding the radiatively allowed transition mechanism of the material. By plotting $(\alpha h\upsilon)^n$ against hυ, where υ is the frequency of the light source and n is the dependence on this transition mechanism of material. One can yield whether the transitions are direct or indirect bandgap. For n= 0.5, the transition nature of the semiconductor is an indirect bandgap. And for n= 2, it is a direct bandgap.

2.5.2. Spectral response

The performance of a photodetector system can be obtained from the responsivity, which is defined as the ratio of the electrical output of detector over the incident power P_{in}. The electrical output of detector can be usually expressed in amperes per watt, or volts per watt, of incident power. So the responsivity R can be expressed as

$$R = \frac{I_p}{P_{in}} or \frac{V_p}{P_{in}} \tag{2-14}$$

where I_p is the photocurrent, V_p is the photovoltage and P_{in} is the illumination power at a wavelength λ. The experimental setup of spectral response measurement is shown as Fig 2.4. The light source with 148W was configured to pass through a Oriel 77250 monochromator to select a particular wavelength for measurement. Inside the monochromator, the s wavelength election ranging from 200 to 1000nm was obtained

by a ruled grating with 1200 line/mm and blaze wavelength at 350 nm. The output slit size from the monochromator was then regulated by a pin hole with 3 mm diameter. Before performing the optical measurement, the spectral power of the light source at a particular wavelength was measured by a Newport Model 840 handheld optical power meter with a calibrated Model 818 UV enhanced silicon detector. The precise optical alignment of the device under test can be controlled by triple axis manipulator. The photo-generated current from the devices can be measured by a Keithley 617 electrometer, which has the lowest current limit down to 10^{-16} A. The spectral response of devices with zero bias voltage was measured from 250nm to 500nm.

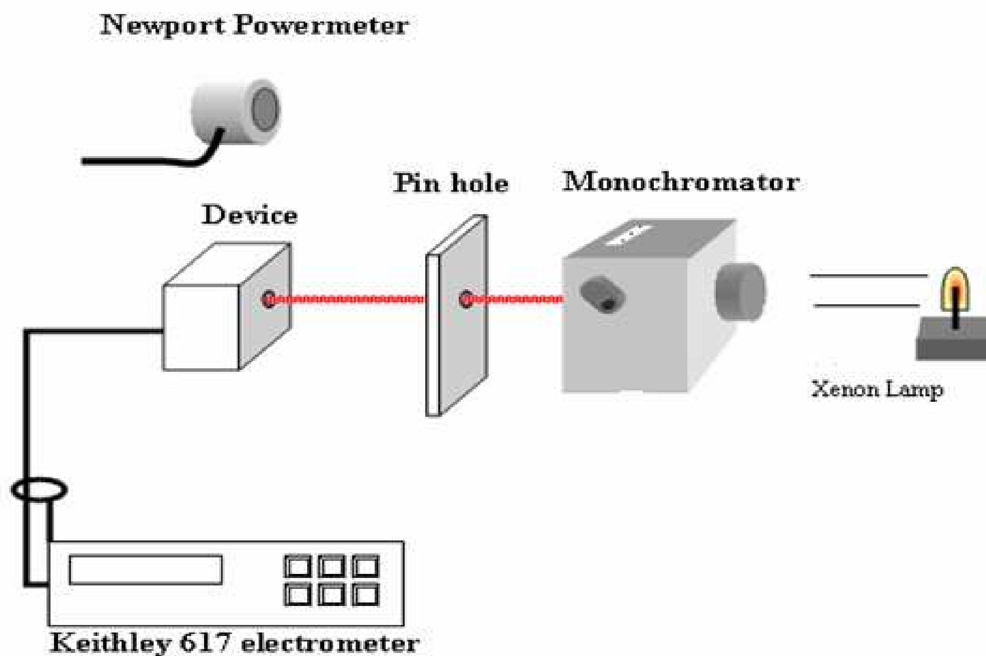

Fig. 2.5 Schematic diagram of the spectral response measurement.

2.5.3. Raman spectroscopy

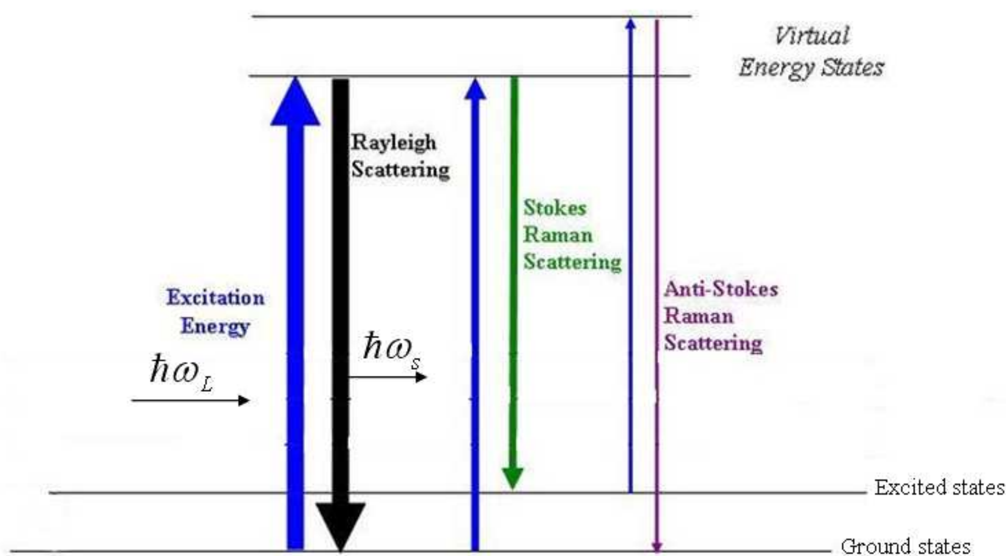

Fig. 2.6 Energy level diagrams of Rayleigh scattering, Stokes Raman scattering, and anti-Stokes Raman scattering.

Raman scattering is a convenient and non-destructive characterization technique for chemical identification, analysis of molecular structures, effects of bonding and stress analysis. This spectroscopic technique is based on the inelastic scattering of visible, near infrared or near ultraviolet range. The working principle of this Raman spectroscopy is that when a monochromatic light is incident on a molecule, it interacts with the electron cloud and the bonding of the molecule. The incident photon excites the molecule into a virtual state. For the spontaneous Raman Effect, the molecule than relaxes to a lower stationary state with the emission of a photon. The energy of the final state may be less or greater than the energy of the initial state. The process is called Stokes or ant-Stokes scattering respectively. The frequency shift $|\hbar\omega_l - \hbar\omega_S|$ also called the Raman shift, is characteristic of the excitations from the sample.

In this project, Raman spectra were recorded at room temperature using a John-Yvon

Horiba HR800 Raman spectrometer (spectral resolution < 0.2 cm^{-1}). A blue laser beam with wavelength 488 nm was employed as incident photons for photon excitation.

Chapter 3. Bandgap engineering of IMZO films with different In content

3.1. Introduction

Zinc oxide is a promising semiconducting material with various applications in electronics due to its large direct bandgap of 3.37 eV and exciton energy of 60 meV, which is more than double of that of GaN. Recently, bandgap engineering of $Zn_{1-x}Mg_xO$ (MZO) and $Zn_{1-x}Cd_xO$ has been demonstrated [3.1, 3.2]. Generally, MZO alloys have wurtzite and cubic structure. By increasing the Mg content($x \geq 45$), the hexagonal structure of MZO changes to a cubic structure [3.3], which can be excellent materials for photonic applications such as UV detector, UV light emitting diode and UV laser [3.4, 3.5]. The cubic MZO has a crystalline structure with a lattice constant of 0.42 nm, which is a very convenient size for lattice matched heteroepitaxial growth of many other oxides, such as perovskites and transition metal monoxides. Moreover, by introducing different amount of indium (In) into MZO films, we can tune their structural, electrical and optical properties easily over a wide range of values.

In this chapter, we report the fabrication of epitaxial (In doped $Mg_{0.5}Zn_{0.5}O$) IMZO films deposited on MgO and LAO substrates by PLD. The change of structural, electrical and optical properties of IMZO films as a function of In content have been studied. The microstructure and the surface morphology of MZO were characterized by atomic force microscopy (AFM) and scanning electron microscopy (SEM). The electrometer and low temperature cryostat helped to measure the resistivity against temperature over the range of 60 – 380 K. Transmittance spectra provided strong

evidences for IMZO films to be a good transparent conducting oxide (TCO) and to possess tunable bandgap.

3.2. Experimental details

Commercial single crystal MgO(001) and $LaAlO_3$ (001) (LAO) substrates were employed to grow the IMZO thin films. Both LAO and MgO substrates are of cubic structure. Their lattice mismatch with IMZO when x=0 are 11.6% and 1.6% respectively. About 500nm thick IMZO films with different In content were fabricated at substrate temperature of 600 ^oC and ambient pressure of 3 x 10^{-5} Torr. The laser fluence was kept to 4 Jcm^{-2} with repetition rate of 10 Hz.

3.3. Structural properties

The conventional solid state reaction was employed to produce the IMZO target. According to the desired stoichiometric ratio of IMZO, high purity powder of In_2O_3 (99.999%), ZnO (99+%) and MgO (99.99%) were mixed in ethanol and ball milled for 6 hours. Then the mixture was calcinated twice in air at 1100 ^oC for 10 hours. The calcined mixture was grounded into fine powder, then compressed in to pellets and followed by sintering at 1350 ^oC for 10 hours. Based on these procedures, IMZO target with different In content (x) of 0, 0.04, 0.08, 0.16 and 0.18 were fabricated.

Figure 3.1 illustrates the XRD diffraction peaks of IMZO targets with different x content. When x equals to 0, 0.04 and 0.08, all the diffraction peaks are attributed to the hexagonal and cubic structure of MZO. At higher In content (x=0.16, 0.18), diffraction peaks of In_2O_3 become more apparent. Moreover, the diffraction peaks of IMZO shifts to lower angles side, meaning the out-of-plane lattice increases It is concluded that some In^{3+} have been doped into the MZO lattice.

3.3.1. Structural properties of IMZO target

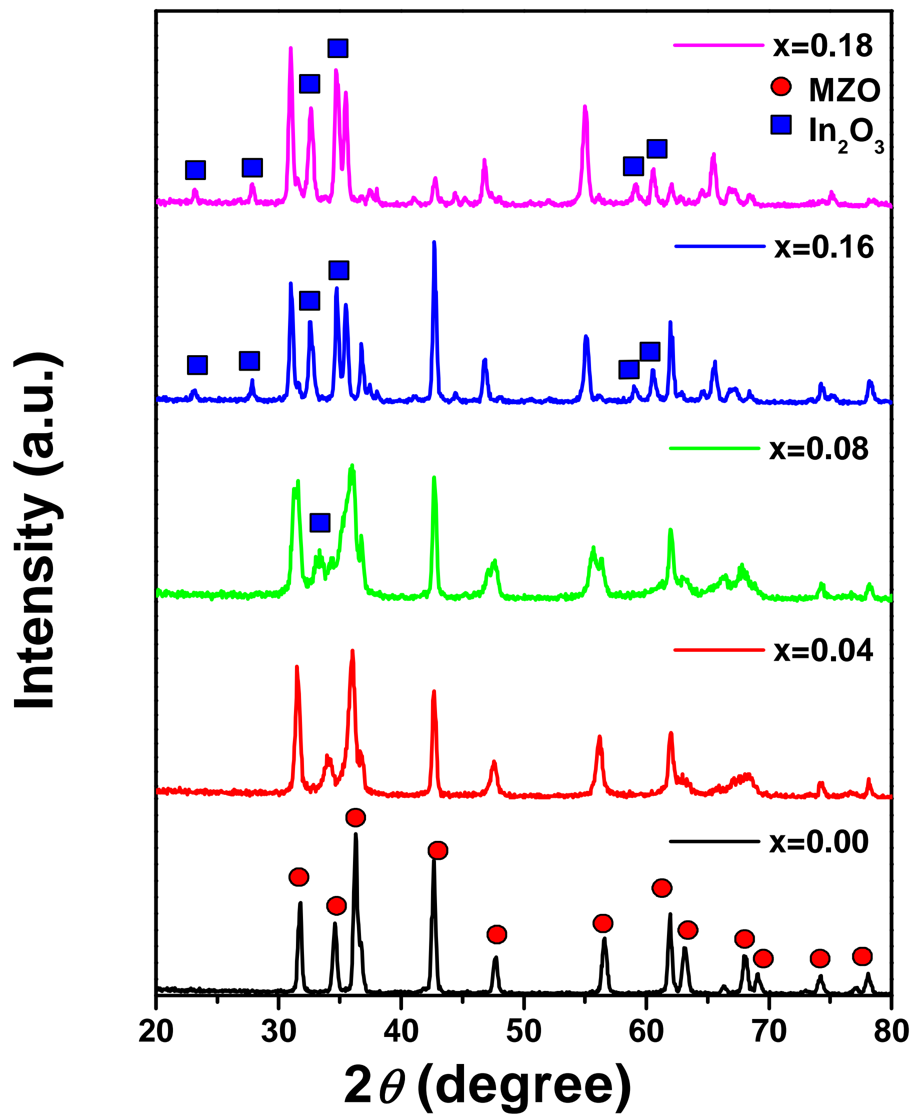

Fig. 3.1 XRD powder diffractions of IMZO targets with different In content (x) of 0, 0.04, 0.08, 0.16 and 0.18 respectively.

3.3.2. Structural properties and surface morphology of IMZO films

Figure 3.2a illustrates the θ-2θ scan x-ray diffraction pattern of $Zn_{0.5}Mg_{0.5}O$ (MZO) films grown on LAO(001) and MgO(001) substrates. Besides the diffraction peaks from LAO substrate, only one diffraction peak located at 42.58^{o} can be attributed to (002) plane of cubic MZO (c-MZO) with lattice constant of 4.24 Å. The absent diffraction peaks of wurtzite structure of MZO indicates that the MZO films are of purely cubic structure. XRD in-plane Phi scan for plane (202) of the MZO and LAO reflections are shown in Fig.3.3. It is cleared that four-fold symmetry diffraction profiles that a heteroepitaxial c-MZO film can be obtained on the LAO(001) substrate. Due to large lattice mismatch between LAO (3.78 Å) and MZO (4.24 Å), the in-plane orientation of the c-MZO film appears to rotate 45° relative to the substrate. Domain matching epitaxy with the sequence 5/4, 4/3 is observed by TEM, indicating a complex strain relaxation mechanism. Thus, heteroepitaxial relationship of MZO(001)||LAO(001) (out of plane) and MZO(011)||LAO(010) (in-plane) has been obtained in MZO films on LAO substrate [3.6, 3.7]. For those grown on MgO substrate as shown in Fig.3.2b, the diffraction peak of MZO(002) can not be resolved by XRD methods due to their almost identical lattice constants. Previous HR-TEM results from our research group have demonstrated that the lattice matching is prefect and no clear interface between c-MZO and MgO is decernable [3.7]. It can be concluded that excellent cube-on-cube homoepitaxial relationship between MZO and MgO substrate is obtained.

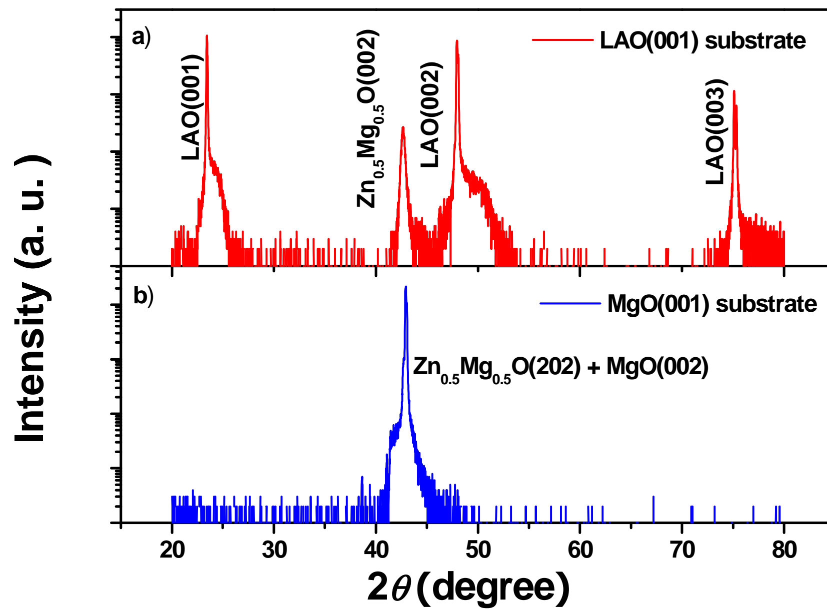

Fig. 3.2 XRD pattern *θ*-2*θ* scans of $Mg_{0.5}Zn_{0.5}O$ films deposited on: a) LAO(001), and b) MgO(001) substrates at 600°C with 3 x 10^{-5} Torr ambient pressure.

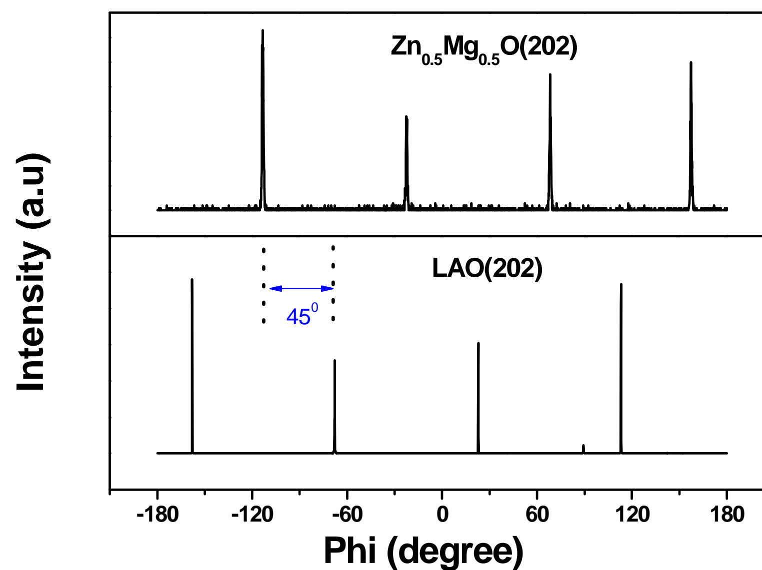

Fig. 3.3 Phi scans of the $Zn_{0.5}Mg_{0.5}O$ (202) and the LAO (202) reflections of the $Zn_{0.5}Mg_{0.5}O$ film on LAO substrate.

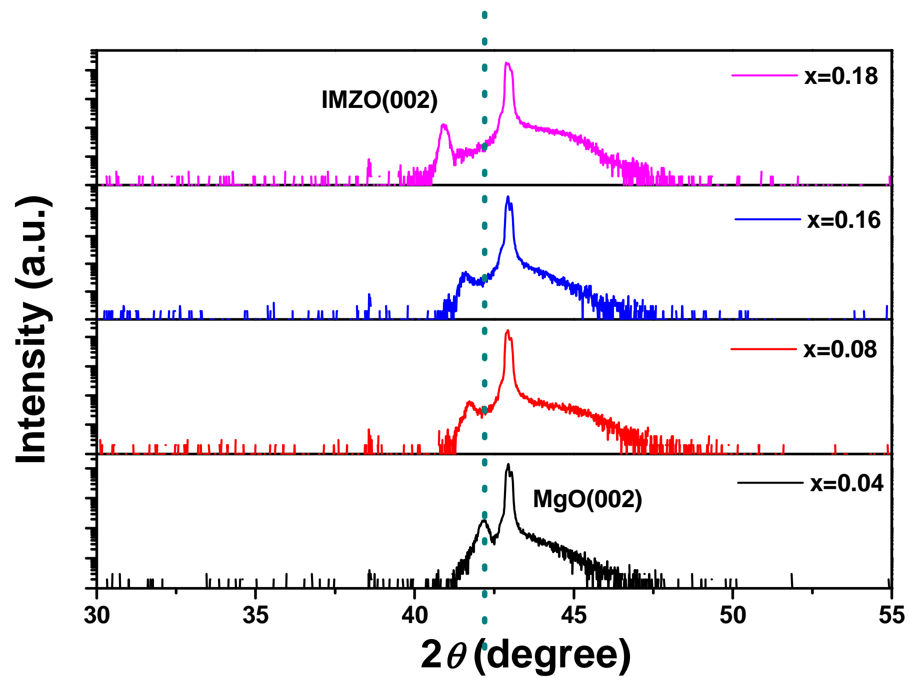

Fig. 3.4 XRD pattern θ-2θ scans of IMZO films deposited on MgO(001) substrates with different In content (x) of 0.04, 0.08, 0.16 and 0.18 in the target.

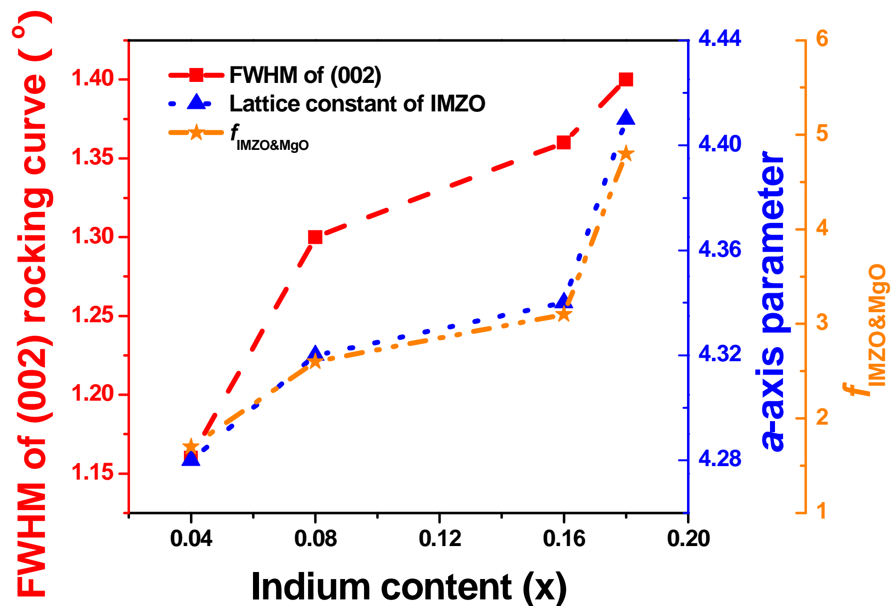

Fig. 3.5 Lattice mismatch between IMZO and MgO, *a*-axis parameter and FWHM values of IMZO(002) with different In content (x) of 0.04, 0.08, 0.16 and 0.18 in the target.

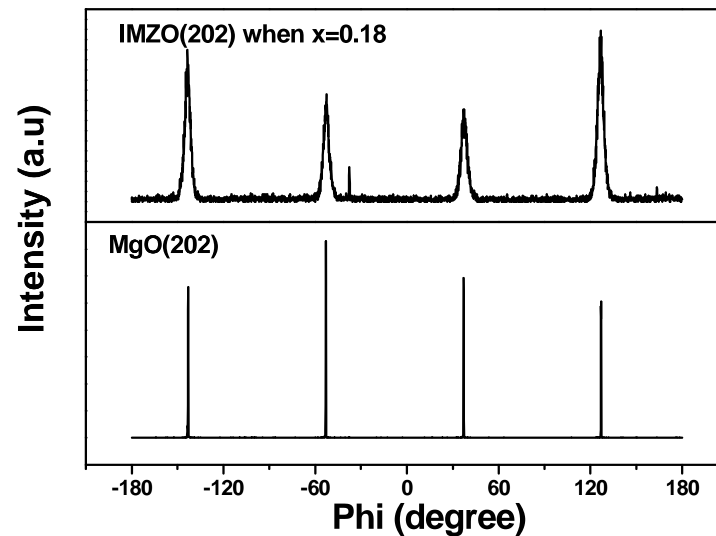

Fig. 3.6 Phi scan of the IMZO(202) and the MgO(202) reflections of the IMZO film on MgO (001) substrate with x =0.18 in the target.

The structural properties of the IMZO films with different In content of 0, 0.04, 0.08, 0.16 and 0.18 were characterized by XRD. The θ-2θ scans XRD of these films are shown in Fig.3.4. Apart from the diffraction peak from MgO(002) of the substrate, sharp diffraction peaks located at around 42° corresponding to diffraction from (002) planes of cubic IMZO appear in all samples. With increasing In content, the IMZO(002) diffraction peak gradually shifts to lower angles. This suggests that substitution of In^{3+} atoms into the lattice of MZO has been achieved. These shifts in IMZO(002) is under our expectation due to larger ion radius of In^{3+}(0.62 Å) than those in Zn^{2+}(0.60 Å) or Mg^{2+}(0.57 Å) [3.8]. The absence of diffraction peak of wurtzite structure of ZMO and phase of pure In_2O_3 indicates that single phase cubic IMZO with preferably (002) orientation is obtained with no phase segregations.

The *a*-axis parameter value of IMZO and lattice mismatch between IMZO and MgO

substrate with different In content are shown in Fig. 3.5.The *a*-axis parameter value increases from 4.28 to 4.41 Å, which implies that an increased out-of-plane residual relaxed stress induced lattice distortion. This is no surprise that substitution of In^{3+} in Mg^{2+} or Zn^{2+} will enlarge the lattice constant of IMZO. Upon increase the In content, the lattice mismatch between IMZO and MgO substrate increases from 1.7 to 4.8 %. Besides the change in lattice constant of IMZO, the crystallinity of IMZO depends on the In content too. Fig.3.5 illustrates the FWHM values of rocking curve of IMZO(002) with different In content. The FWHM values of IMZO(002) increases from 1.16^{o} to 1.40^{o}. These results indicated that the crystal quality of IMZO declines as the In content increases. Figure 3.6 shows the XRD in-plane Phi scan for (202) plane of the IMZO films grown at 600°C in 3 x 10^{-5} Torr ambient pressure. In plane of XRD analysis shows that the films are epitaxial with IMZO(202) plane aligned with MgO(202) plane, suggesting no rotations between the unit cell of IMZO and MgO.

Figure 3.7(a)-3.7(d) show the AFM images of IMZO films with different In content (x) of 0, 0.08, 0.16 and 0.18 respectively. Without any In content, the surface morphology of the film is quite flat and smooth. By increasing the In content, the surface morphology has greatly changed. It can be observed that the surface roughness decreases from 6.87 to 1.28 nm with increasing In content from 0.04 to 0.18. Gradually increasing the In content, the grain size became smaller.

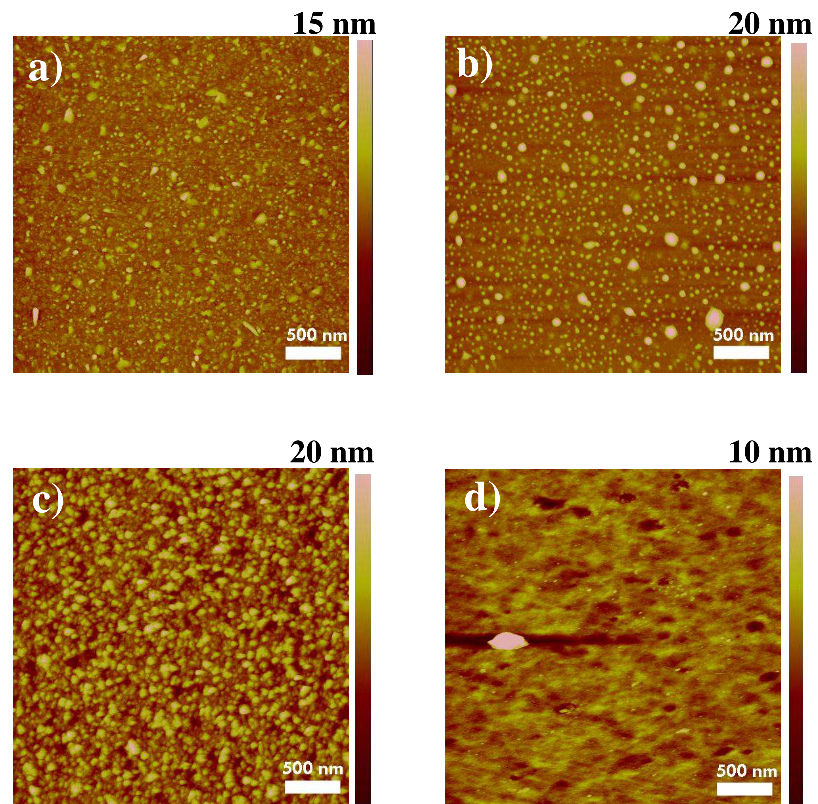

Fig. 3.7 AFM images of IMZO films with different In content (x): a) 0, b) 0.08, c) 0.16 and d) 0.18 in the target, measured over 3 x 3 μm^2 scanning size.

3.4. Electrical properties

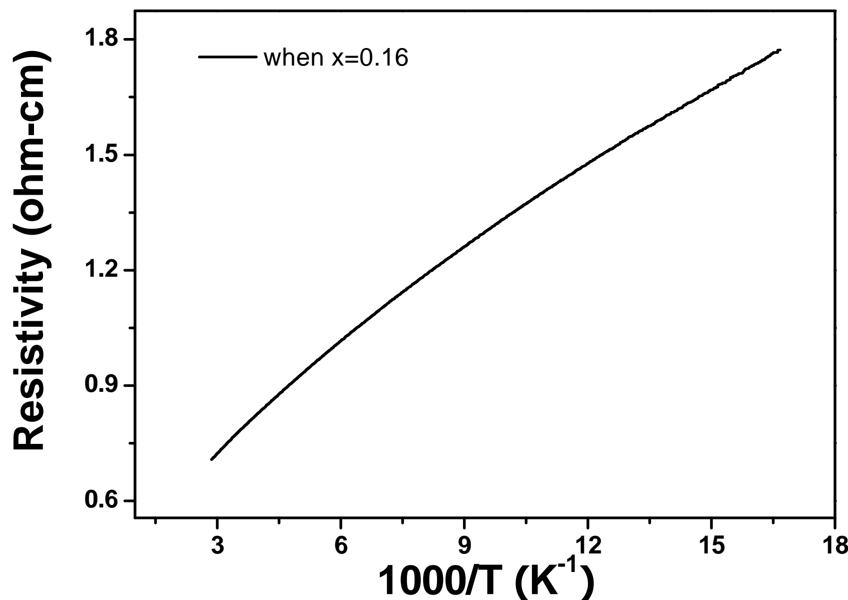

Fig. 3.8 Resistivity of IMZO films as a function of temperature for the In content (x) of 0.16 in the target.

Figure 3.8 illustrates the resistivity ρ as a function of 1000/T for the IMZO film when In content is x=0.16. These temperature dependence measurements can yield the electrical conduction mechanism in the IMZO films, which exhibit a decrease trend in resistance when the temperature is increased. This suggests that a semiconducting-like conduction mechanism is dominant in the IMZO films.

Several donor impurities are known to improve the electrical conductivity in ZnO. The Group Ⅲ elements Al [3.9-3.11], Sn [3.12], Ga [3.13], and In, in particularly, substitute easily for Zn ions($Zn_{Al/Ga/In}$), can be incorporated to become degenerated semiconductor means that the carrier concentration is higher than 10^{20} cm^{-3}. Moreover, oxygen vacancies (V_O) are also an important parameter that contributes to the

conductivity of ZnO. Under a high deposition temperature and high vacuum, ZnO film can easily become oxygen deficient. The concentration of oxygen vacancies in the ZnO can greatly affect the electrical and optical properties of ZnO thin films. In our case, the cubic phase MZO possesses a higher bandgap (6.2 eV) than that wurtzite phase of ZnO. These larger bandgap energy results a high resistivity(10^7 Ω-cm). Introducing a large amount of indium oxide, the electrical conductivities can be greatly improved. Thus, the electrical properties of IMZO films with different In content were characterized by Hall Effect measurement and two-point probe technique.

Resistivity, carrier concentration and mobility of IMZO films with different In content are shown in Fig. 3.9. It is difficult to use the Hall Effect measurement for investigating the mobility and carrier concentration of these films due to the high resistivity of undoped and slightly In doped MZO films. Under this limitation, the two-point probe is employed to evaluate the resistivity of these films only. By Introducing In content of 0.04 into intrinsic cubic phase MZO films, resistivity is substantially decreased from 2.06×10^7 to 5.2×10^3 Ω-cm. Moreover, the Hall measurements suggest that the IMZO films with In content of 0.08, 0.16 and 0.18 exhibit *n*-type conduction. As the In content increases from 0.08 to 0.18, the resistivity of these films is gradually decreased from 3.6 to 0.01 ohm-cm, and accompanies with the increases in the carrier concentration and a slight change in Hall mobility. The maximum electron concentration was found to be 3.06×10^{20} cm^{-3} in the IMZO film with In content of 0.18, the Hall mobility of 1.6 cm^2/V s and resistivity of 0.0128 Ωcm, which is two orders of magnitude higher than the value of ITO epitaxial films(1.1×10^{-4} Ωcm)[3.14]. This improved resistivity in the IMZO films is due to the fact that the substitution of In^{3+} into Zn^{2+} or Mg^{2+} sites donates more free electrons to the IMZO system.

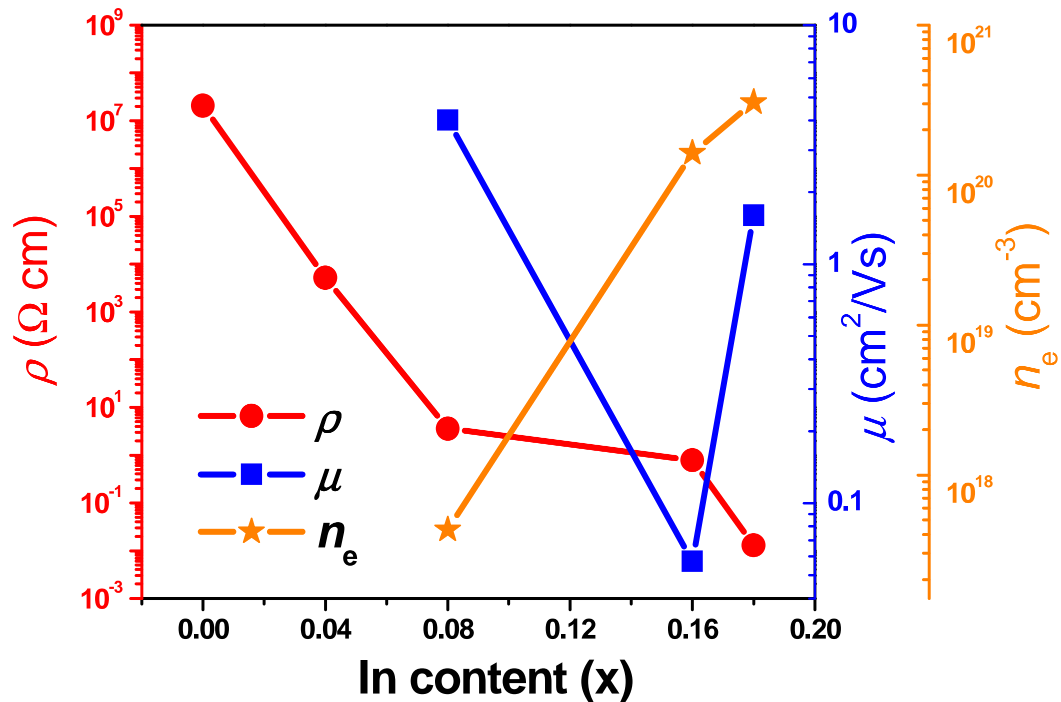

Fig. 3.9 Electrical resistivity (*ρ*), Hall mobility (*μ*) and carrier concentration (n_e) of IMZO films as a function of In content (x) of 0, 0.04, 0.08, 0.16 and 0.18 in the target.

3.5. Optical properties

The optical properties of IMZO films were analyzed by UV-VIS spectrometer at room temperature. Figure 3.10 shows the transmittance spectra of IMZO films with different In content. All samples shows reasonable absorption edge and excellent transmittance of about 90% in the visible ranges. Introducing more In content, the cut-off edge shifts from 210 to 300 nm. No multi-absorption edges occur in these samples. This indicates that no typical phase segregation of MZO occurs in the IMZO sample. For direct bandgap semiconductor, the relationship of absorption coefficient (α) and the optical bandgap (E_g) can be expressed as

$$\alpha \propto (h\nu - E_g)^{1/2} \qquad (3\text{-}1)$$

h and ν are the Planck constant and the frequency of the incident photon, respectively.

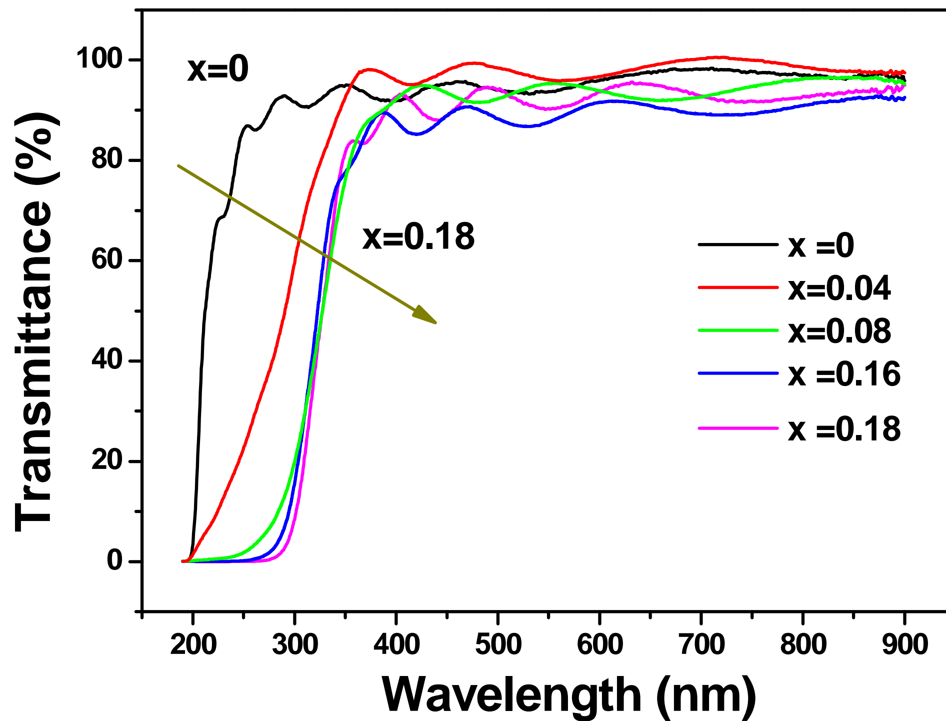

Fig. 3.10 Transmittance spectrum of IMZO films as a function of In content (x) in the target.

Figure 3.11 shows the bandgap of IMZO obtained from the extrapolation approach based on Eq. (1).The bandgap energy deceases from 6.17 to 4.29 eV monotonously as the In content increases. This feature is attributed to the fact that the bandgap of In_2O_3 (3.7eV) is much smaller than that of MgO (7.8 eV).The bandgap could be easily modified by controlling the In content in the films. This is very useful for the application for solar-blind UV detectors and tunable UV filter.

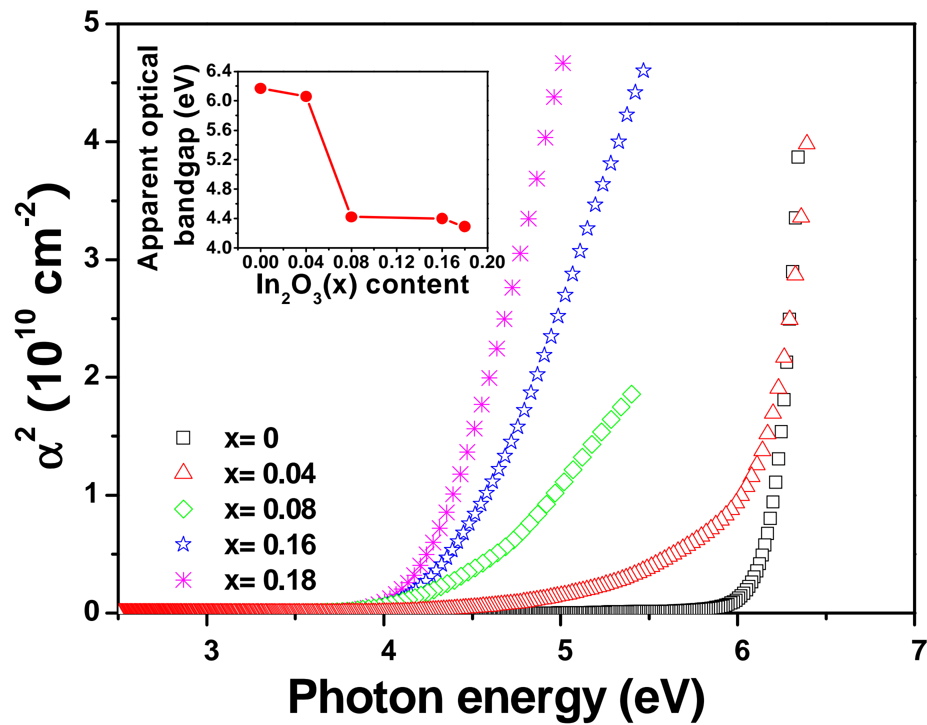

Fig. 3.11 The square of absorption coefficient versus photon energy for IMZO films with different In content (x) of 0, 0.04, 0.08, 0.16, and 0.18 in the target.

3.6. Summary

Epitaxial magnesium zinc oxide (MZO) films with cubic structure were successfully fabricated on single crystal MgO (001) and LAO (001) substrates by pulsed laser deposition method. Upon increasing the In content, the IMZO(002) diffraction peak moves towards to smaller angles. Based on Bragg's law, the decrease in the diffraction angle corresponds to the increase in the interplanar spacing (d_{002}). Since In^{3+} has larger ionic radius than Zn^{2+} or Mg^{2+}, this substitution of In atoms for Zn or Mg increases the lattice constant of IMZO. Besides the shift in IMZO(002) diffraction peak, it is found that the crystal quality of IMZO film is degraded upon increment of the In content.

In the electrical measurement, the temperature dependence of resistivity of IMZO films suggested that a semiconducting-like conduction mechanism is dominant in the IMZO films. Introducing an appropriate content of In, the resistivity can be greatly reduced. The maximum electron concentration was found to be 3.06×10^{20} cm^{-3} in IMZO film with In content of 0.18, the Hall mobility of 1.6 cm^2/V s and resistivity of 1.2×10^{-2} Ω cm.

It has been demonstrated that by alloying with different amount of indium oxide, the transition energy of IMZO films can be widely tuned from 6.7 to 4.29eV. All IMZO films have excellent optical transmittance of over 90 % for the whole visible spectrum. Therefore, these IMZO films can be used as transparent conducting oxide (TCO) for various optoelectronics applications

Chapter 4. Structural, electrical and optical properties of IMZO films with different thickness

4.1. Introduction

Transparent conducting oxides (TCOs) such as SnO_2:F, ZnO:Al and In_2O_3:Sn have been extensively used in the optoelectronic industries as indispensable component in flat panel display, windows for solar cell and UV detector [4.1-4.7]. However, crystalline TCO that can be template for epitaxial growth of perovskites and transition metal monoxides remains elusive due to the large lattice mismatch between TCO and the perovskites. In the previous chapter, we have demonstrated that IMZO films have stable cubic crystalline structure with a lattice constant of 0.42 nm. This is a very convenient size for lattice matched heteroepitaxial growth of many oxides, such as perovskites and transition metal monoxides. IMZO films exhibited resistivity of about 1.28 x 10^{-2} Ω-cm and more than 90% optical transmittance over the whole visible spectrum. As a result, IMZO can be utilized as TCO with cubic structure. In our knowledge, up to now, no reports on epitaxial cubic phase TCO (IMZO) films with lattice constant of about 4.2 Å were published. In this chapter, the preparation of IMZO TCO films deposited on MgO(001) substrate using PLD method is reported. The structural, electrical and optical properties of the IMZO films with different thickness are also presented.

4.2. Experimental details

IMZO films with different thickness were deposited on MgO(001) substrate. A 18% In_2O_3 doped $Mg_{0.5}Zn_{0.5}O$ (IMZO, when x=0.18) was employed as the PLD target. All the films were deposited at 600°C substrate temperature and oxygen pressure of 3 x 10^{-5} Torr on MgO substrates.

4.3. Structural properties of IMZO films of different thickness

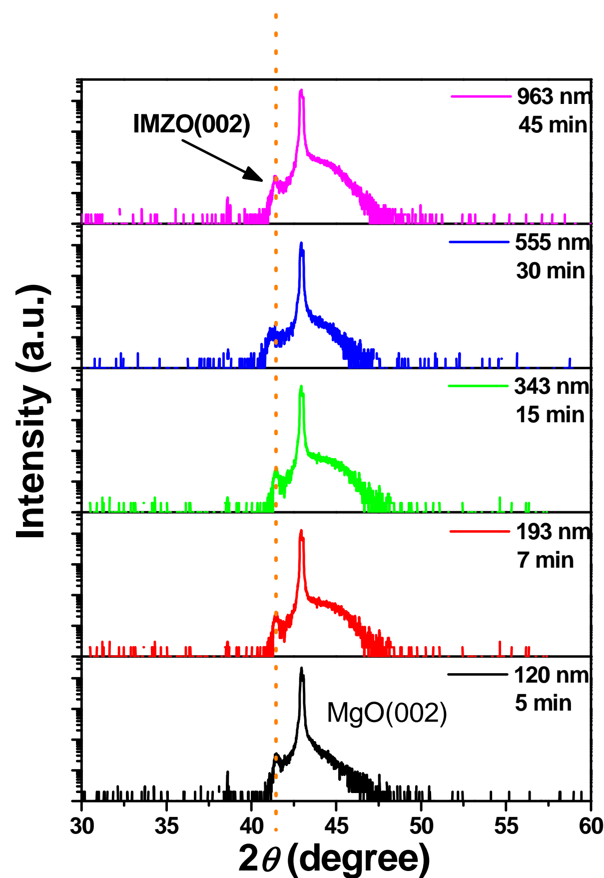

Fig. 4.1 XRD pattern *θ-2θ* scans of IMZO films (when x= 0.18 in the target) with various deposition times of 5, 7, 15, 30, and 45 min, which corresponded to the film thickness of 120, 193, 343, 555, and 943 nm respectively.

Figure 4.1 shows the XRD pattern of θ-2θ scan for IMZO films grown with various deposition times, indicative film thickness are also given. Apart from the diffraction peak from the MgO substrate, only IMZO(002) is observed in all samples. This indicates that the IMZO films have a cubic structure. It is noted that the wurtzite phase of MZO and crystalline phase of In_2O_3 are not observed in the XRD pattern, implying that no phase segregations occurs. Moreover, it can be proved that In^{3+} atoms substitute Mg^{2+} or Zn^{2+} in the MZO lattice. With increasing the film thickness, the diffraction peak of IMZO(002) does not show any significant changes. This corresponds to the fact that there are no induced stresses at increased film thickness.

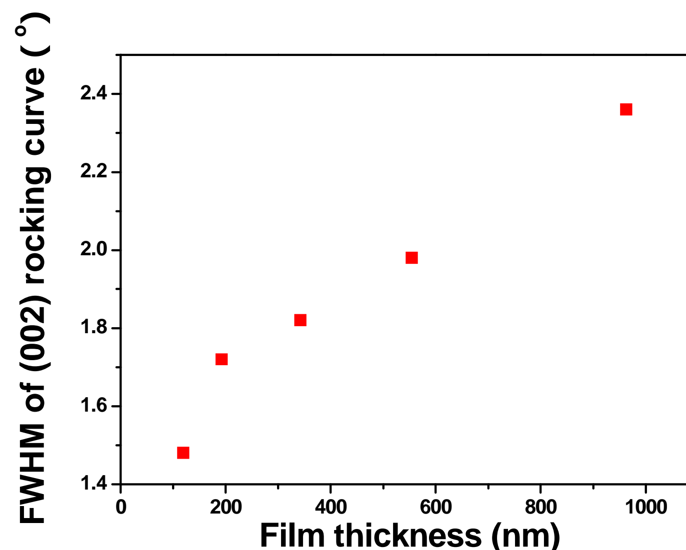

Fig. 4.2 FWHM of (002) rocking curves for IMZO films (when x= 0.18 in the target) with different thickness.

The values of FWHM in the omega scan of IMZO(002) diffraction peak with different thickness are shown in Fig.4.2. The film thickness increases from 120 to 953 nm in accordance to the duration of the deposition time. It is found that variations in the crystal quality of the films are primarily attributed to the change in the film thickness.

The FWHM value of IMZO(002) increases from 1.48° to 2.36° with film thickness. In plane analysis shows the films are epitaxial with IMZO(202) plane aligned with MgO(202) plane, suggesting no any rotations between the unit cell of IMZO and MgO.

4.4. Electrical properties of IMZO films with different thickness

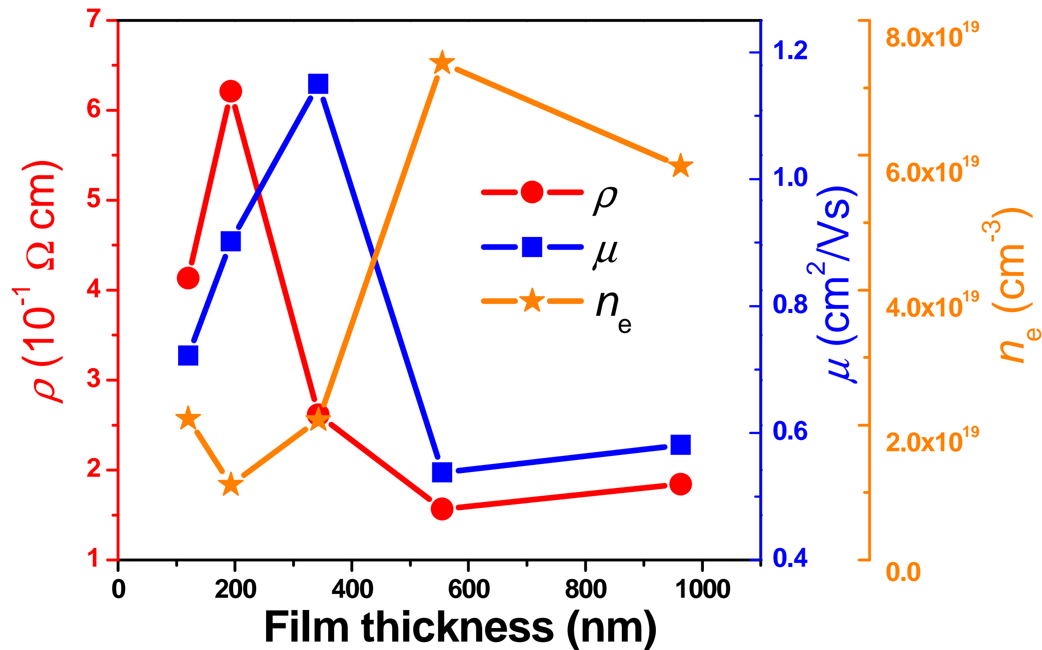

Fig. 4.3 Electrical resistivity (*ρ*), hall mobility (*μ*) and carrier concentration (n_e) with different thickness of IMZO films, when x=0.18 in the target.

Figure 4.3 shows the thickness dependence of the electrical resistivity, Hall mobility and carrier concentration on IMZO films that were epitaxially grown on MgO (001) substrates. As the thickness increases from 120 to 193 nm, resistivity increases from 0.41 to 0.62 Ω-cm. However, resistivity decreases sharply from 0.62 to 0.18 Ω-cm for thicker films. Similar dependence in resistivity and carrier concentration with the various film thickness was reported in the Zr-doped ZnO [4.8]. As shown in Fig. 4.3, our results indicate the dramatic reduction of resistivity with thickness originates from

changes in carrier concentration than Hall mobility. It is known that the mobility is associated with grain-boundary scattering and ionized-impurity scattering [4.9, 4.10]. The mobility will decrease with increase of carrier concentration in ionized-impurity scattering [4.11, 4.12]. However, if the grain-boundary scattering dominates, the mobility will increase with the carrier concentration. In our cases, Hall mobility increases from 0.722 to 0.902 cm^2/Vs when film thickness increases from 120 to 193 nm, which corresponds to the decrease in carrier concentration from $2.09 x 10^{19}$ to $1.11 x 10^{19}$ cm^{-3}. Moreover, when film thickness increases from 343 to 943 nm, the Hall mobility decreases while the carrier concentration increases. It appears that the trends of change in carrier concentration and Hall mobility are always opposite. Hence, we suggested that the ionized-impurity scattering governs in the IMZO films rather than grain boundary scattering. The lowest resistivity of 0.157 Ω-cm is obtained when the film thickness is 555 nm. The corresponding Hall mobility is 0.538 cm^2/Vs and the carrier concentration is 7.37 x 10^{19} cm^{-3}.

4.5. Optical properties of IMZO films with different thickness

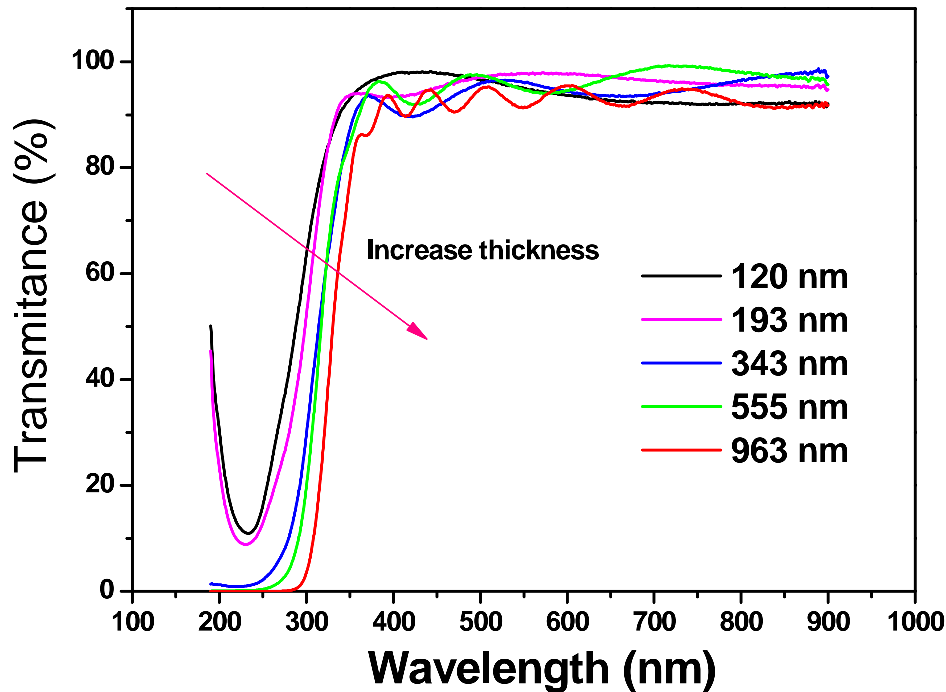

Fig. 4.4 Optical transmittance spectra with IMZO films (x=0.18 in the target) as a function of film thickness.

Figure 4.4 shows the optical transmittance of the IMZO film with different thickness in the wavelength range of 250 to 900 nm. The oscillation of the spectra is due to the interference originated from the reflection at interfaces of the films. And it can be observed that all IMZO films exhibit excellent optical transmittance of over 90 % in the visible range, regardless of the changes in thickness. Figure 4.5 shows the square of the product of absorption coefficient and photon energy as a function of film thickness. The inset shows the change in apparent optical bandgap with the variation in thickness. The bandgap decreases from 4.51 to 4.21 eV when the thickness increases from 120 to 963 nm. Generally, it is known that the bandgap increases with the carrier concentration, due to the Burstein-Moss (B-M) shift [4.13, 4.14]. However, as shown in Fig. 4.5, these

relationships between bandgap and carrier concentration cannot be explained by the B-M shift. Note that the decrease in bandgap may be attributed to the degradation of the crystallinity as the increase in thickness, which is revealed by the XRD measurement as shown in Fig. 4.2.

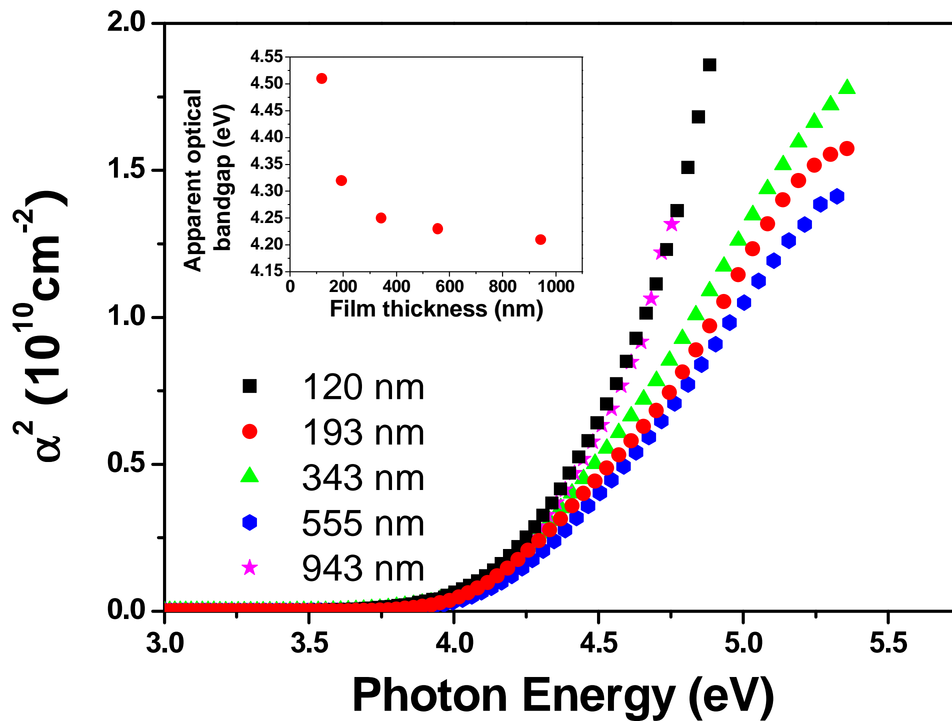

Fig. 4.5 Relationship between the square of absorption coefficient (α^2) and photon energy (eV) of IMZO films with thickness. The inset is the optical bandgap as a function of film thickness.

4.6. Summary

Different thickness of cubic phase epitaxial IMZO films with high transparency and low resistivity were prepared on MgO(001) substrate by PLD. It is found that the structural, electrical and optical properties show strong dependence on the film thickness. Generally thicker IMZO films exhibit poorer crystallinity, and lead to changes in the electrical and optical properties.

From the electrical characterization, the mobility is found to be reduced with increased carrier concentration. The relationship between the structural and electrical properties suggests that the ionized-scattering mechanism dominates in the IMZO films rather than the grain-boundary scattering. The lowest resistivity achieved is 0.157 Ω-cm with Hall mobility of 0.538 cm^2/Vs and a carrier concentration of 7.37 x 10^{19} cm^{-3}, where the film thickness is 555 nm.

All IMZO films demonstrate a transmittance of about 90% in the visible wavelength. The apparent optical bandgap was found to be reduced from 4.51 to 4.32 eV upon increment of the film thickness. We suggested that the degradation of crystallinity plays a more crucial role in shortening the bandgap of IMZO films.

Chapter 5. Structural, electrical and optical properties of LNO/IMZO heteroepitaxial junctions grown on MgO(100) substrates

5.1. Introduction

Transparent conducting oxides (TCOs) have been widely used in optoelectronic industries. However, most TCOs exhibit an *n*-type electrical conduction. In order to fully utilize the TCOs in the optoelectronic industries, TCOs with *p*-type electrical conduction should be explored. Recently, *p*-type ZnO and ZnMgO have been reported [5.1-5.6]. It still remains difficult to fabricate a reproducible and high quality *p*-type ZnO due to reasons such as deep acceptor levels, low solubility of the dopants and the self compensation. Instead of fabricating *p-n* homojunctions, many researchers have turned to make heterojunction with different *p*-type semiconducting oxides such as $CuAlO_2$ [5.7, 5.8], $CuGaO_2$ [5.9, 5.10], and $SrCu_2O_2$ [5.11], mainly grown on amorphous substrates. This polycrystalline structure of *p*-type layers has introduced more lattice defects in the interface comparing with the epitaxial growth, which will degrade the optical and electrical performance of the heterojunction [5.10]. Another approach is to fabricate high quality heteroepitaxial *p-n* junction that can effectively reduce the defect density at the interfaces.

Among the *p*-type semiconducting oxide, simple cubic structure and semi-transparency are found in NiO. This *p*-type semiconductor has a direct bandgap of 3.7eV with weak absorption bands due to *d-d* transition of a $3d^8$ electron configuration in the visible

region [5.12]. When Li^+ partially substitute the sites of Ni^{2+}, the electrical resistivity can be reduced to $10^{-1}\,\Omega$-cm.

In this chapter, we report the fabrication of *p*-LNO/*n*-IMZO heterojunctions with different In doping concentration of 0.08, 0.16 and 0.18 in the target. The *p*-LNO/*n*-IMZO heterojunction has several advantages: the first is that both IMZO and LNO are simple cubic structures; compatible structure can reduce the dislocation at the interface of the two layers. The epitaxial relation helps minimizing the electron scattering and increasing the efficiency of electron transportation across the interface. The second advantage is that lattice mismatch between LNO and IMZO is only 2.8 to 4.8%, depending on the indium oxide content in the *n*-IMZO layer. This small lattice mismatch allows epitaxial growth of *p*-LNO/*n*-IMZO heterojunctions. Finally, IMZO can doubly act as the TCO owing to its high optical transmittance (>95%) within the visible spectrum.

5.2. Structural, electrical and optical characterization of $Li_{0.15}Ni_{0.85}O$

5.2.1. Structural characterization of LNO ceramics target

The $Li_{0.15}Ni_{0.85}O$ (LNO) ceramics target was fabricated by the conventional solid state reaction methods. High purity of 0.831g Li_2CO_3 and 9.524g NiO powder were used as the starting materials. They were mixed with ethanol and then ball milled for 6 hours. Then the mixture was calcinated twice in air for 10 hours at 1100 °C and 1200 °C respectively. The calcined mixture was grounded into fined powder again. Finally they were compressed into pellets and followed by sintering at 1350 °C for 10 hours.

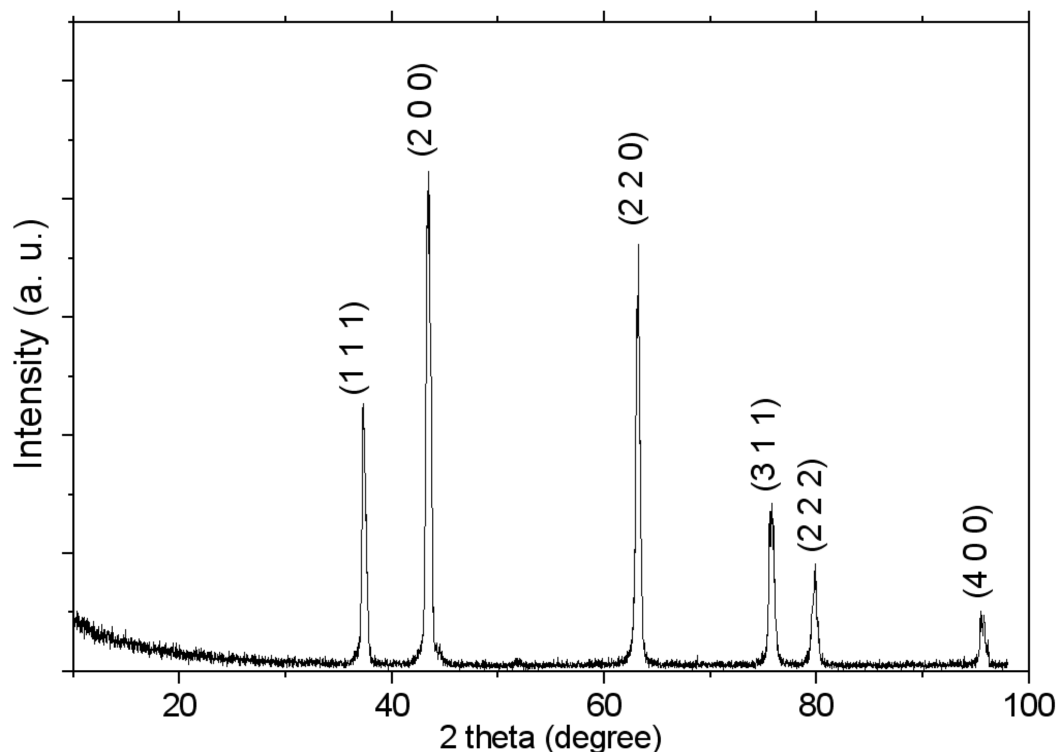

Fig. 5.1 The X-ray diffraction pattern of densely sintered $Li_{0.15}Ni_{0.85}O$ ceramics target.

Figure 4.1 shows the X-ray diffraction pattern of densely sintered LNO ceramics target. All the strong diffraction peaks indicate the target, which is well crystallized with a simple cubic structure that matches with the LNO data from the XRD database of IDD

international Centre for Diffraction Data.

5.2.2. Deposition of LNO Layer

Initially single layer LNO thin film was grown on MgO(001) substrate by PLD. Prior to being loading into the vacuum chamber, MgO(001) substrates were cleaned ultrasonically for 5 min in acetone and then 5 min in ethanol. The deposition chamber was evacuated to base pressure of about a few mTorr by a roughing pump. Substrate temperature was kept at 500°C with oxygen pressure at 100 mTorr during the deposition of the LNO layer. As-deposited LNO film of about 100 nm thick was annealed *in situ* at the same growth temperature for 20 min to improve the crystalline structure. Pure stoichiometric nickel oxide is an insulator with simple cubic structure. When Li^{+} partially substitute the sites of Ni^{2+}, a hole is introduced in the form of Ni^{3+} or O^{-} to keep charge neutrality [5.13]. And this oxide becomes a black semiconductor. Varying the deposition temperature and oxygen pressure can easily control the electrical and optical properties of LNO thin films. The deposition temperature for LNO can not be higher than 600 °C, because Li atoms tend to evaporate from the film. Even if the LNO layer was deposited at room temperature, approximately 75% of Li evaporates [5.14]. In our works, we optimized the substrate temperature (T_s) to about 500-600°C with oxygen pressure (Po_2) of about 100-150 mTorr.

5.2.3. Structural characterization of LNO layer

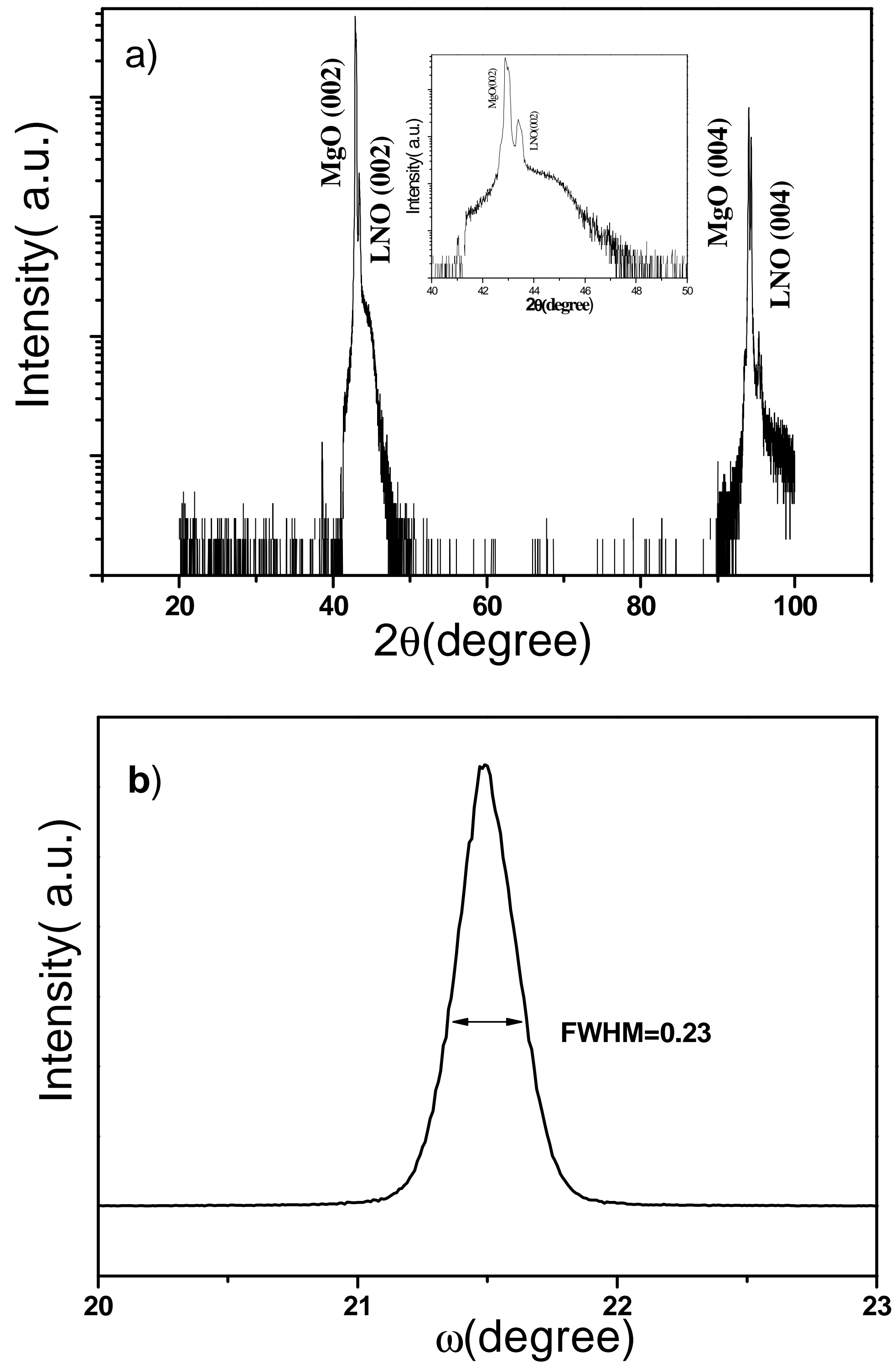

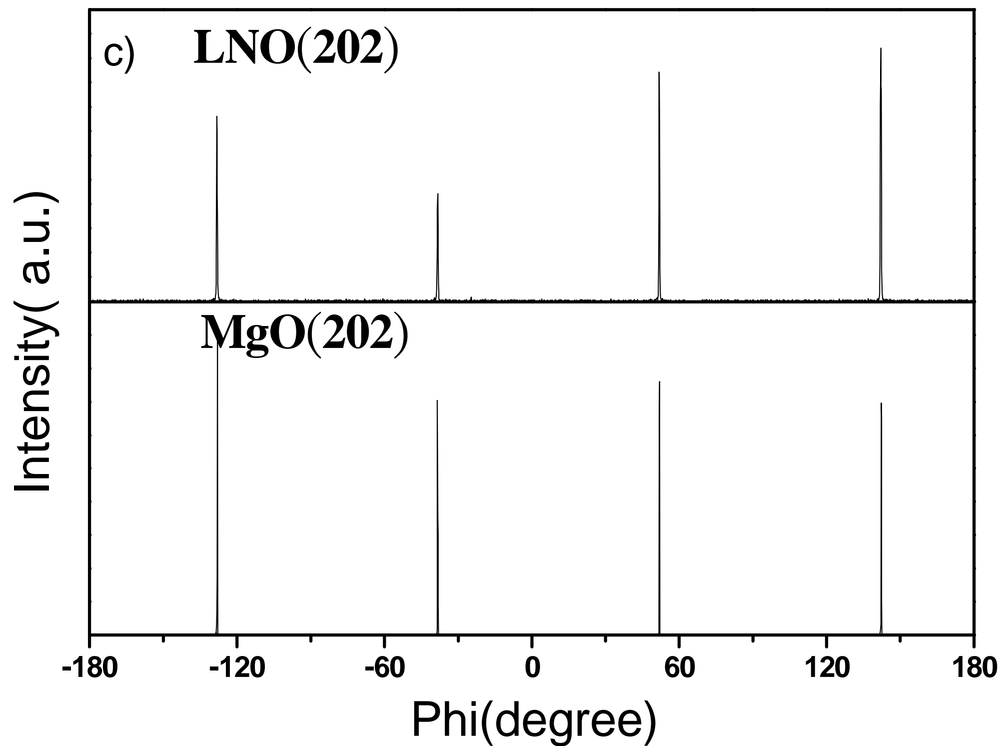

Fig. 5.2 X- Ray diffraction patterns for LNO films deposited on MgO(100) at 500°C with 100 mTorr oxygen pressure: (a) θ-2θ scan, (b) the rocking curve of (002) peak of LNO, (c) Phi scan measured from (202) LNO and (202) MgO.

Figure 5.2a shows the x-ray diffraction pattern of LNO film grown on MgO(001) substrate. Apart from the diffraction peaks of MgO(002), only strong diffraction from LNO (00ℓ) is observed. This indicates that the LNO layer is of cubic structure only. No diffraction peaks from Li_2O_3 and Ni are observed. Note that the diffraction peak of LNO(002) is located at 43.37°. This corresponds to a lattice constant of 4.17 Å, which is almost the same value as bulk LNO materials, suggesting no significant stress induced lattice distortion in the film. This is attributed to the very small lattice mismatch (~1%) with MgO substrate. The crystal quality of LNO on MgO(001) is confirmed by

out-of-plane rocking curve, which was indicated by the diffraction peak of LNO(002). As shown in Fig. 5.2b, the FWHM of 0.23^{o} is observed in the ω-scan of LNO(002) diffraction peak. Figure 4.2c shows the XRD in-plane Phi scan for (202) plane of the LNO films grown at 500 ^{o}C in 100 mTorr oxygen pressure. In plane analysis shows the films are epitaxial with LNO(202) plane aligned with MgO(202) plane, suggesting cube-on-cube heteroepitaxy.

5.2.4. Electrical and optical properties of LNO layer

Table 5.1 shows the resistivity, Hall mobility and carrier concentration of the LNO films grown on MgO substrate under the deposition conditions (T_s=500 ^{o}C and Po_2=100 mTorr). The carrier concentration is positive value in the Hall Effect measurement, which confirms that LNO layer is a *p*-type semiconductor. The resistivity and mobility of LNO films are 1.19 Ω-cm and 0.093 $cm^2V^{-1}s^{-1}$ respectively at room temperature. This electrical results are comparable with that of the epitaxial growth of LNO films grown on YSZ(111) substrate reported by T. Kamyia *et.al*. [5.14].

Table 5.1Resistivity, Hall mobility and carrier density for LNO films deposited on single crystal MgO substrate under the deposition conditions (T_s=500°C and Po_2=100 m Torr).

Resistivity (Ω-cm)	Carrier concentration (cm^{-3})	Mobility ($cm^2V^{-1}s^{-1}$)
1.19	1.13 x 10^{20}	0.093

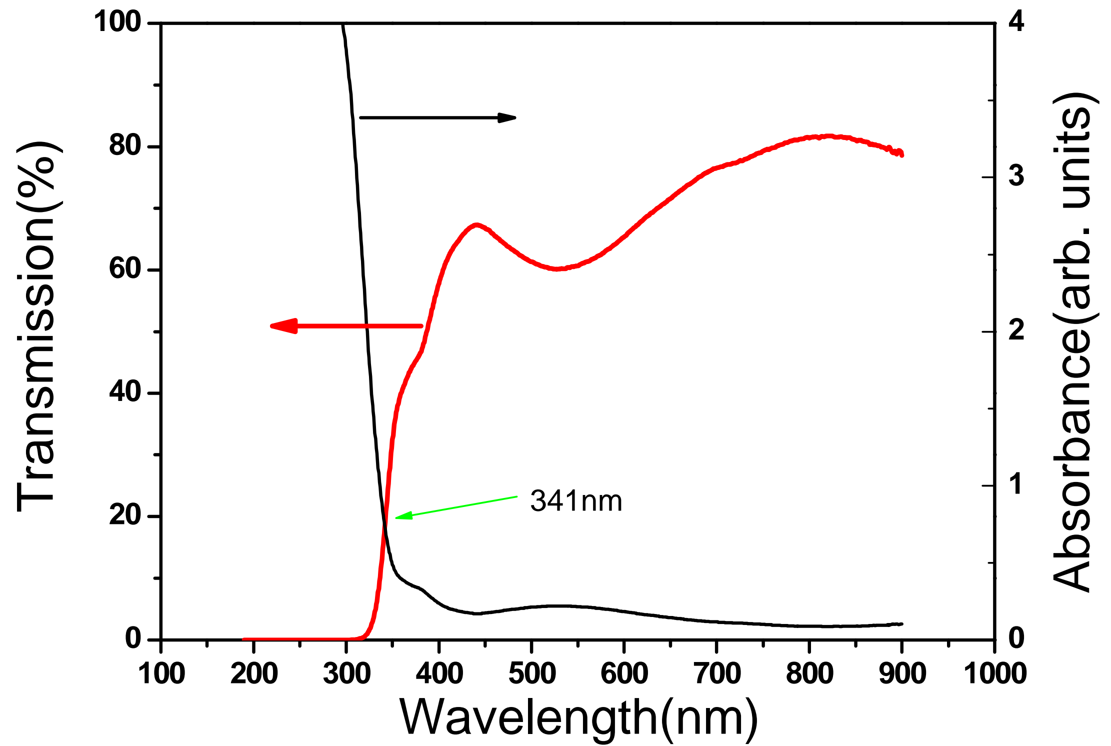

Fig. 5.3 UV-visible transmission and absorption spectra of LNO film on MgO(100) substrate showing a strong absorption at 341nm.

Figure 5.3 shows the transmittance and absorbance spectra for LNO films grown on two-side polished MgO(001)substrate. The transmittance spectrum reveals a strong absorption in the 330nm wavelength, which corresponds to a bandgap energy of 3.76eV. The transmittance over the whole visible range is over 60%.

5.3. Experimental details

Considering the excellent experimental results obtained for single layer of InMgZnO(IMZO) and LNO films deposited on the single crystal MgO(001) substrate, we attempted to fabricate a transparent *p-n* junction diode using *n*-IMZO and *p*-LNO layers. The *p*-LNO/n-IMZO heteroepitaxial diode with different In content in the *n*-IMZO layers were deposited by PLD on MgO(001). A schematic layout of the diode configuration is shown in Fig. 5.4. Densely sintered IMZO and LNO ceramic targets were made by conventional solid-state reaction with constitute oxides. The detailed procedure has presented in Chapter 3.3 and 5.2.

A KrF Excimer laser was used to ablated IMZO ceramic targets. Substrate temperature was kept at 600 ^{o}C with ambient oxygen pressure of 3 x 10^{-5} Torr during the growth of a 500 nm thick IMZO *n*-type layer. The sample was then annealed *in situ* at the same growth temperature for 20 min to improve the crystalline structure. LNO was subsequently grown at 500 ^{o}C with oxygen pressure of 100 mTorr. Using stainless steel mask with regular arrays of 500 x 500 μm^2 openings, a 100 nm of LNO film was deposited through the holes of the mask, resulting isolated flat LNO square islands on top of the IMZO layer. Circular spot platinum electrodes of 200 μm diameter were finally deposited at room temperature on the LNO islands via another properly shaped and aligned mask by PLD.

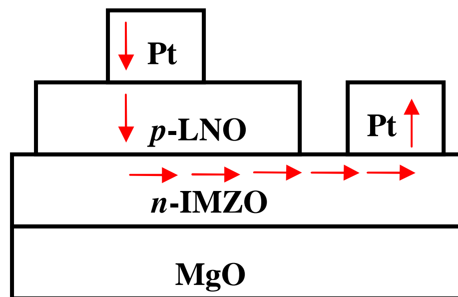

Fig. 5.4 Schematic structure of LNO/ IMZO *p-n* heteroepitaxial diode. The red arrow is the current flow direction under forward bias voltage.

The crystalline structure of the heteroepitaxial junctions was characterized by an X-ray diffractometer operated in four-circle-mode. A Keithley 2400 was used to evaluate the electrical properties. The temperature dependent *I-V* characteristic of the junction was examined over a temperature range of 160 to 300K. Spectral responses of different heterojunctions were examined by Xenon lamp as a light source.

5.4. Structural properties of heterojunctions grown on MgO substrates

Figure 5.5a illustrates the θ-2θ scan x-ray diffraction pattern of the *p-n* heterojunction with different indium oxide doping in the *n*-IMZO layers grown on MgO(001) substrates. Apart from the diffraction reflections of IMZO(002)CuK$_\beta$, MgO(002)CuK$_\beta$, LNO(002)CuK$_\beta$ and MgO(002), sharp diffraction peaks of IMZO(002) and LNO(002) can be found. They are assigned to the cubic structure of LNO and IMZO. No impurity phase of IMZO or LNO can be seen from the XRD results.

Table 5.2 lists the lattice mismatch, 2 theta angle value of LNO and IMZO for the *p-n* heterojunction. With increasing indium content, the diffraction peak of IMZO(002) shifts toward smaller diffraction angle, implying that the lattice constant of IMZO can be altered by changing indium doping concentration in the *n*-type layer. This increase in the lattice constant of IMZO suggests that the large size of indium ions have been substituted into the MgZnO lattice. As shown in Fig 5.5b, the FWHM of the rocking curve of IMZO(002) and LNO(002) when x=0.18 are 1.38^o and 0.25^o respectively. This implies that both the IMZO and LNO layers have good crystallinities. Figure 5.5c shows XRD in-plane Phi scan for plane (202) of the LNO, IMZO and MgO reflections. Four Phi-scan peaks at 90° intervals confirm the cube-on-cube epitaxy relationship of LNO(001)|| IMZO(001)|| MgO(001).

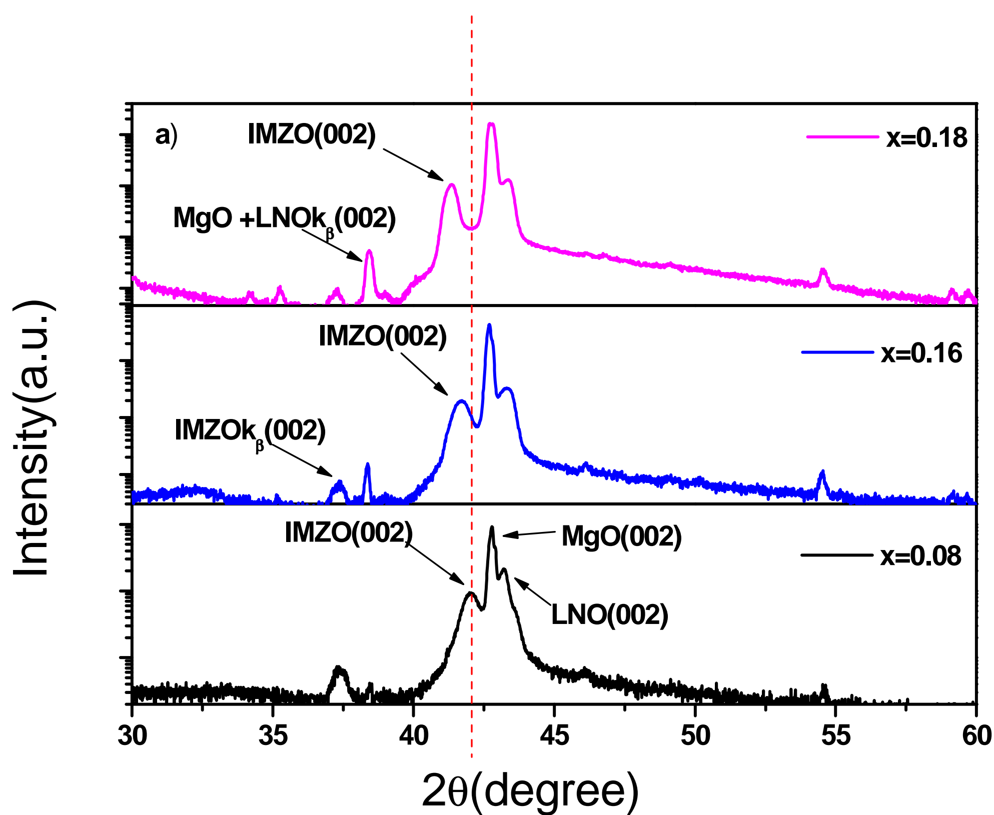
a)
IMZO(002)
MgO +LNOk$_\beta$(002)
x=0.18
IMZO(002)
IMZOk$_\beta$(002)
x=0.16
IMZO(002)
MgO(002)
LNO(002)
x=0.08
Intensity(a.u.)
2θ(degree)
30
35
40
45
50
55
60

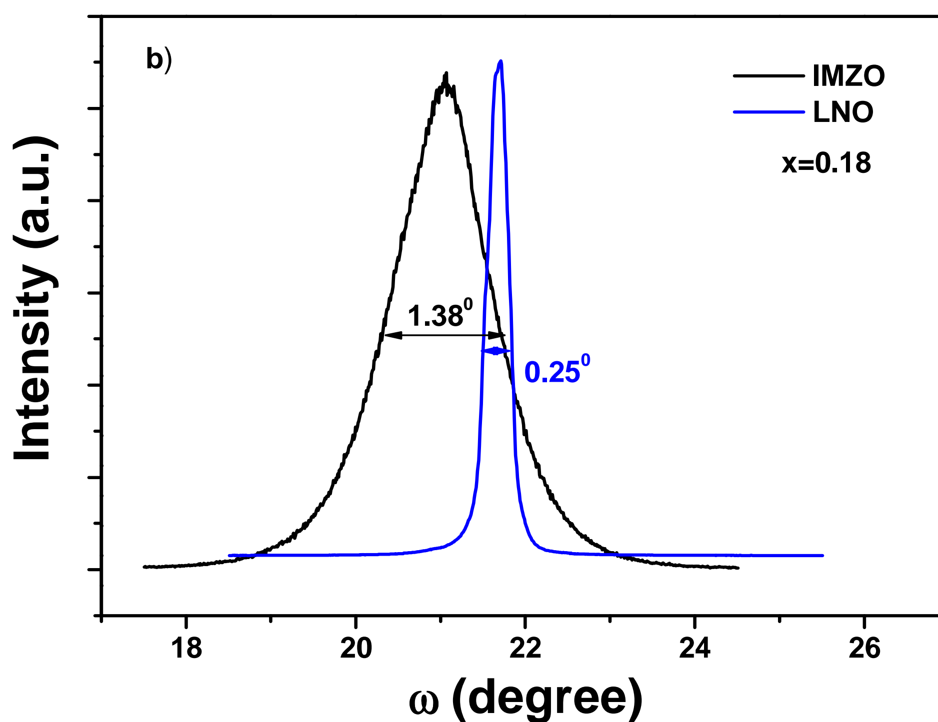
b)
IMZO
LNO
x=0.18
1.38^0
0.25^0
Intensity (a.u.)
ω (degree)
18
20
22
24
26

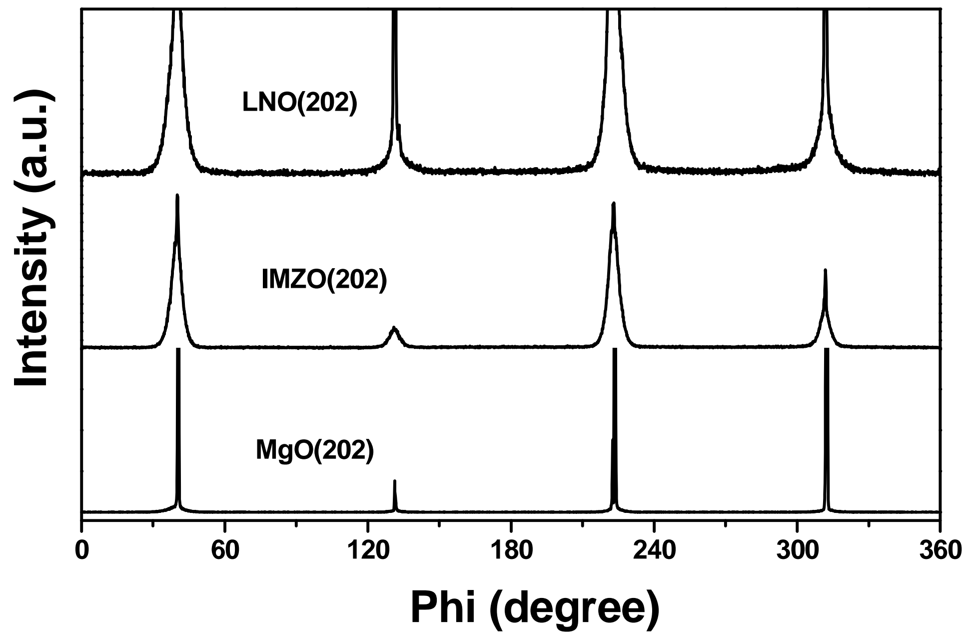

Fig. 5.5 X-Ray diffraction patterns for *p*-LNO/*n*-IMZO heterojunctions deposited on MgO(001) with different In content (x) in the target: (a) θ-2θ scan, (b) the rocking curve of (002) peak of LNO and IMZO when x=0.18, (c) Phi scan measured from LNO(202), IMZO(202) and MgO(202) when x=0.18.

Table 5.2 Lattice mismatch between IMZO and LNO, 2 theta angle of LNO and IMZO for *p-n* heterojunctions with different In content (x) in the target.

In content (x)	Lattice $_{IMZO/LNO}$	$2\theta_{IMZO}$	$2\theta_{LNO}$
0.08	2.8%	42.03°	43.24°
0.16	3.8%	41.66°	43.35°
0.18	4.8%	41.30°	43.39°

5.5. Electrical properties of heterojunctions grown on MgO substrates

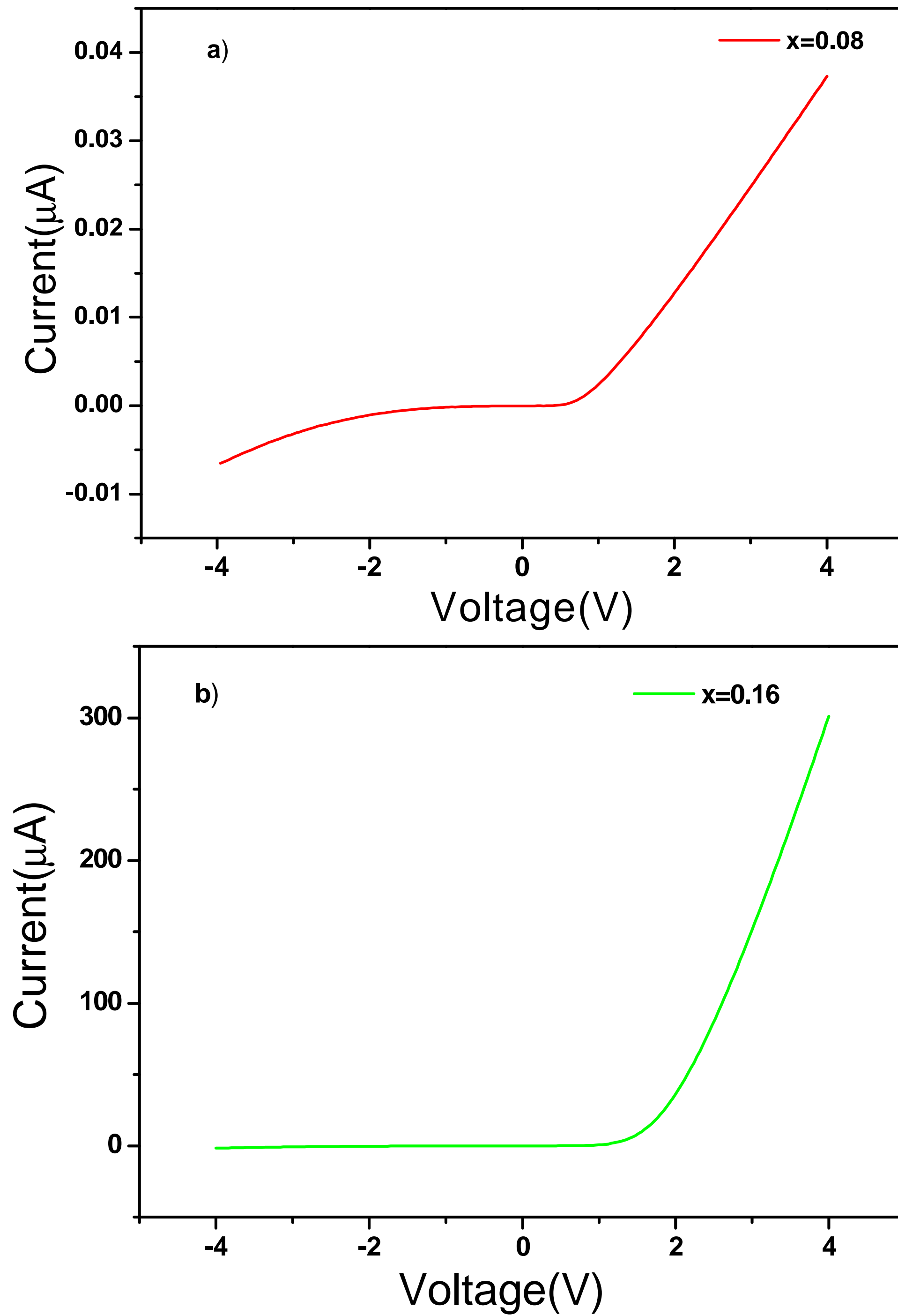

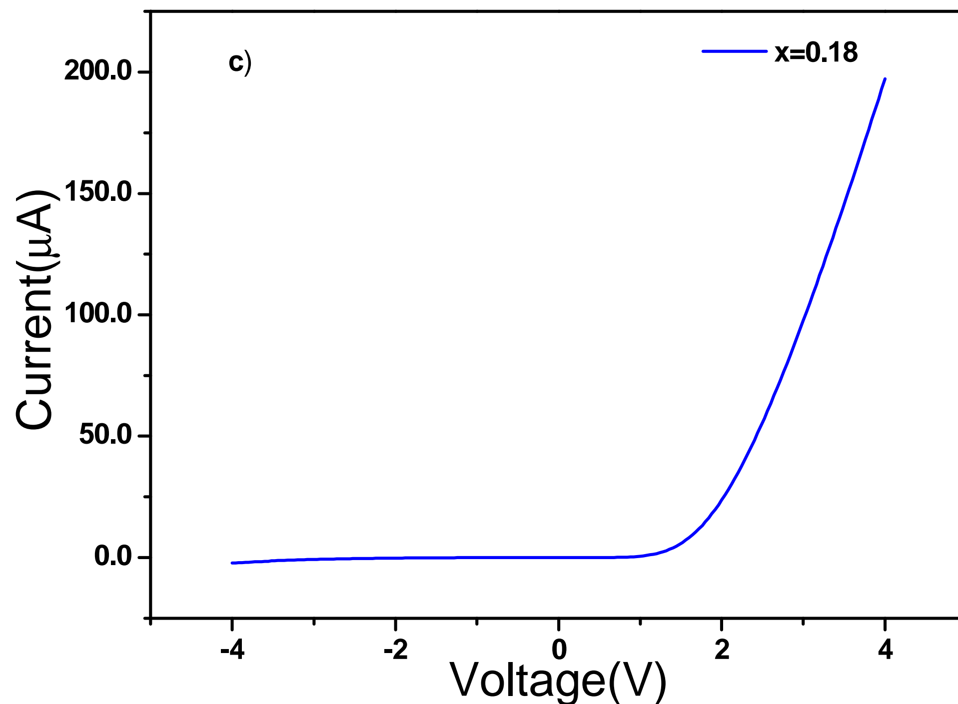

Fig. 5.6 *I-V* curve of *p*-LNO/*n*-IMZO heterojunctions on MgO(001) substrate with different In content (x) a) 0.08, b) 0.16 and c) 0.18 in the target.

The current-voltage (*I-V*) characteristics of *p*-LNO/*n*-IMZO heterojunctions with different indium doping concentration of 0.08, 0.16 and 0.18 are shown in Fig. 5.6. Good ohmic contact of Pt/IMZO/Pt (x=0.08, 0.16 and 0.18) and Pt/LNO/Pt are confirmed by 2-probe electrical measurement and are shown in Fig. 5.7. The results suggest that the non-linear rectifying *I-V* behavior is primarily due to the *p-n* junction.

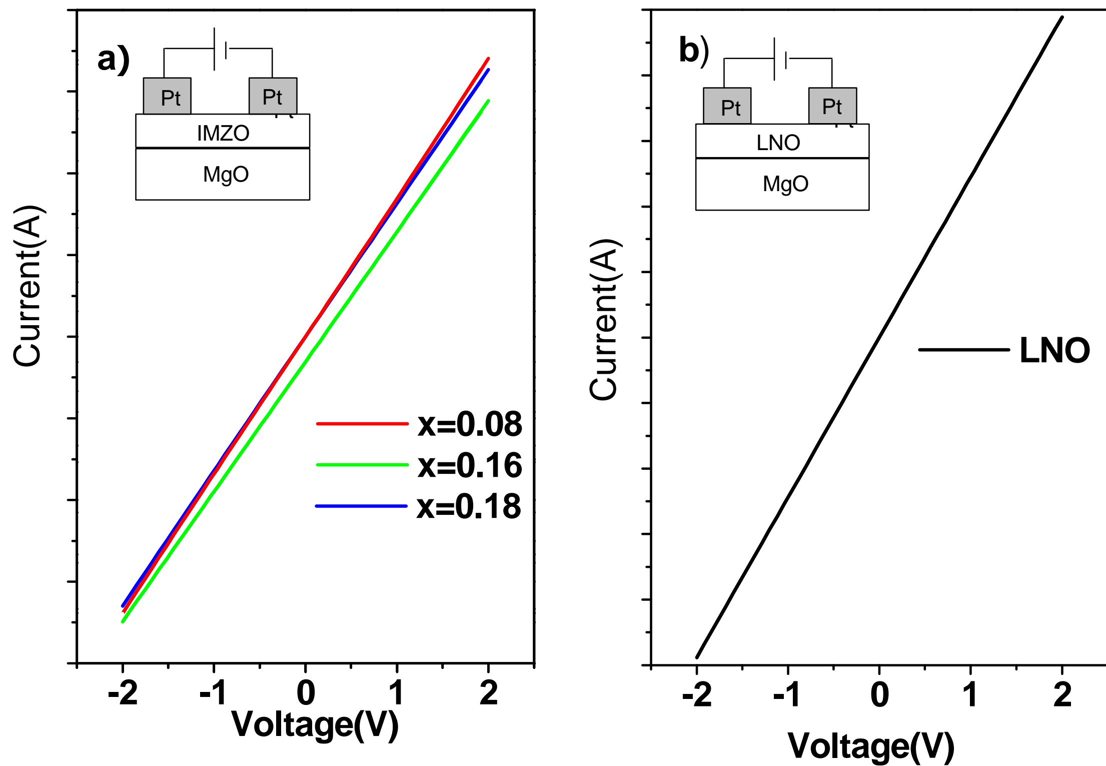

Fig. 5.7 ***I-V*** **characteristics between the two platinum electrodes on the a) IMZO film with different In content (x) of 0.08, 0.16 and 0.18 in the target, b) LNO film.**

Table 5.3 Threshold voltage, current rectifying ratio of +4 /-4 and the leakage current at -4V values for the heterojunction with different In content in the target.

In content	V_{on}(V)	$I_{+4/-4V}$	$I_{leak\ at\ -4V}$ (A)
0.08	0.97	5.7	6.25×10^{-9}
0.16	2	169	1.78×10^{-6}
0.18	2.14	83	2.29×10^{-6}

Table 5.3 lists the turn-on voltage and current rectifying ratio of +4 and -4 for this junction with different In content. The turn-on voltage and breakdown voltage of these

p-LNO/*n*-IMZO heteroepitaxial junctions are around 0.97 V and -3 V respectively when x= 0.08. With higher indium doping content in the *n*-type IMZO layer, both of turn-on voltage and breakdown voltage of the junctions increase. The increase in threshold voltage is due to the higher built-in potential generated by the Fermi-level of *p*-type LNO and *n*-type IMZO, which is assigned to be the tunable bandgap of *n*-type IMZO layer. In Chapter 3, it has been demonstrated that by doping with different amount of indium oxide, the transition energy of IMZO films can be widely tuned from 6.17eV to 4.29eV. Moreover, the increase in turn-on voltage may be also due to the increase in lattice mismatch between LNO and IMZO upon increment of the indium content. This leads to more structural imperfections and electron scattering at the interfaces. But the breakdown voltage of this junction can be greatly improved upon increment the indium content. Moreover only a small leakage current of 1.78 *u*A at -4V was observed in the reverse bias region when x=0.16. The ratio of forward current to reverse current is larger than 169 in the applied voltage of +4 to -4V. These electrical results are comparable with other transparent *p-n* junction [5.15-5.19].

Under the forward bias voltage of greater than a few millivolts, the standard diode equation [5.20] can be modified as

$$I = I_0 \exp\left(\frac{qV}{\eta kT}\right) \qquad (4\text{-}1)$$

where q is the electronic charge, V is the applied voltage, k is the Boltzmann constant, n is the ideality factor and I_0 is the reverse saturation current.

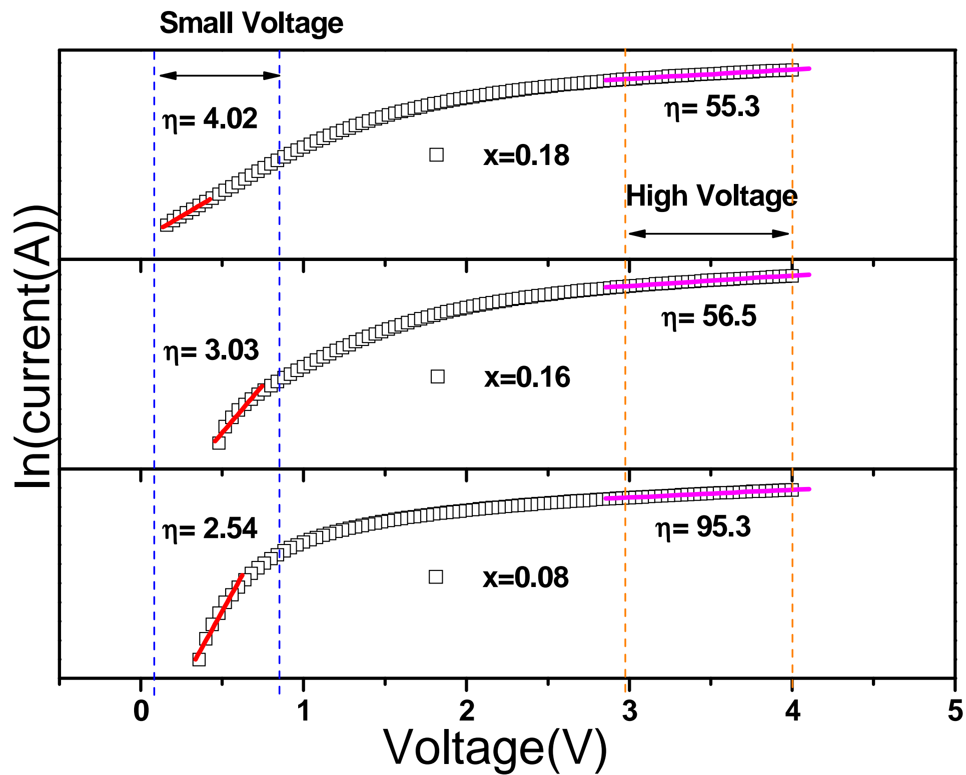

Fig. 5.8 Forward bias Ln(*I*)-*V* curve of *p*-LNO/*n*-IMZO heterojunctions on MgO substrate. Exponential fit lines corresponding to ideality factor: in low voltage region: 2.54, 3.03 and 4.02; in large voltage: 95.3, 56.5 and 55.3 with different In content (x) of 0.08, 0.16 and 0.18 in the *n*-type layer (target).

Figure 5.8 shows the typical In(*I*)-*V* of this *p*-*n* heteroepitaxial junction with different indium doing content in the *n*-type IMZO layers, which is measured at room temperature. In a small forward bias voltage region, ideality factors were found to be 2.54, 3.03 and 4.02, with different In content of 0.08, 0.16 and 0.18 respectively. Theses large values in the ideality factor indicate that these heterojunctions cannot exhibit ideal current transportation (n=1 for diffusion limited, n=2 for recombination limited). Such increase trend in the ideality factors are attributed to the larger lattice mismatch between LNO and IMZO layers, which increases probabilities of defect-assisted tunneling and

carrier recombination in the space charge region via interfaces states [5.21, 5.22].

For a large forward bias voltage (3<V<4), the ideality factors were found to be 95.3, 56.3 and 55.3, with In content of 0.08, 0.16 and 0.18 respectively. These large values suggest that *p*-LNO/*n*-IMZO heterojunctions are affected by a non-negligible circuit resistance in series. The decrease trend in the ideality factor is attributed to the decrease in the resistance of IMZO upon increase the content of indium oxide content.

5.5.1. Temperature dependence of *I-V* characteristics

To understand the current transport mechanism of the *p*-LNO/*n*-IMZO junction when x=0.16, *I-V* characteristics of a heterojunction with size of 500 x 500 μm^2 in a range of temperatures T=160-300K, are shown in Fig. 5.9. The values of leakage current and ideality factor are also plotted in Fig. 5.10 as a function of temperature.

By gradually increasing the junction temperature, the turn-on voltage of heteroepitaxial junction decreases and leakage current increases. These behaviors indicate that more carriers can have enough energy to tunnel or drift across the depletion layer, which is the so-called "thermal assisted tunneling" easily happened in the heavy doped semiconductors [5.24].

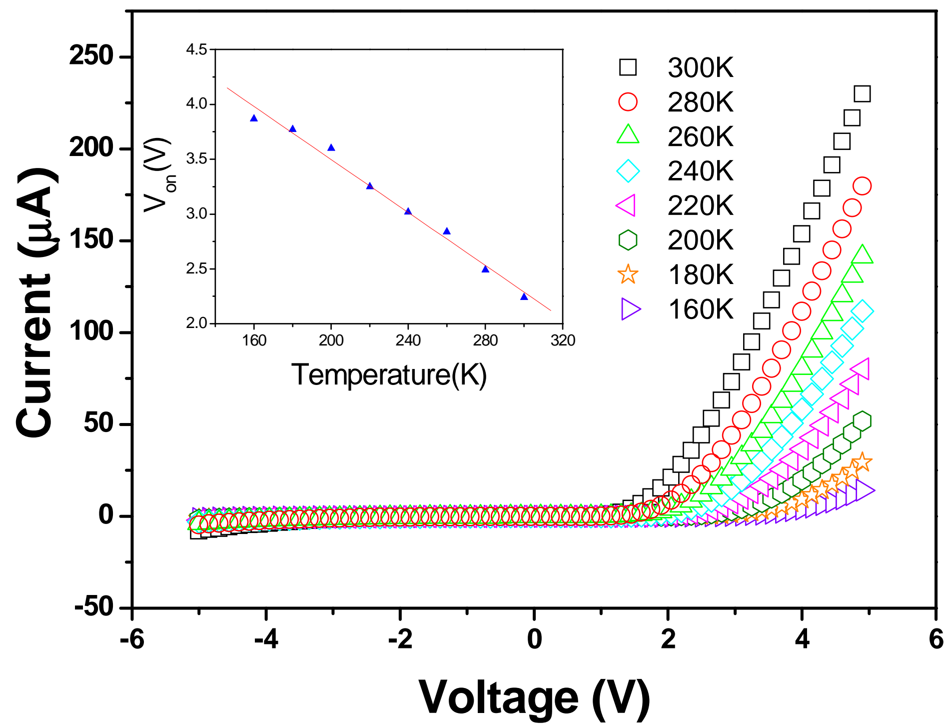

Fig. 5.9 Current-Voltage characteristics of *p*-LNO/*n*-IMZO heterojunction as a function of temperature, when the In content (x) in the target is equal to 0.16. The inset is the plot of threshold voltage against temperatures.

Also, the ideality factors are found to rise from of 3.79 to 13.0, as the junction temperature increases. Such large values in ideality factors indicate that the heterojunction cannot explain an ideal *p-n* junction. Generally, the ideality factor increases with junction temperature, which indicates that the current transport of this heterojunction is dominated by thermionic emission. But the ideality factor of this *p*-LNO/*n*-IMZO junction increases with the decrease in junction temperature. These changes in ideality factors may come from extra currents due to the tunneling through the barrier or the generation-recombination process occurring in the depletion region

[5.21]. This can also be explained by Eq. (4-2) where the ideality factor is inversely proportional to the junction temperature [5.21, 5.23].

$$\eta = \frac{q}{kT}\frac{\partial V}{In\left(\frac{I}{I_0}\right)} \tag{4-2}$$

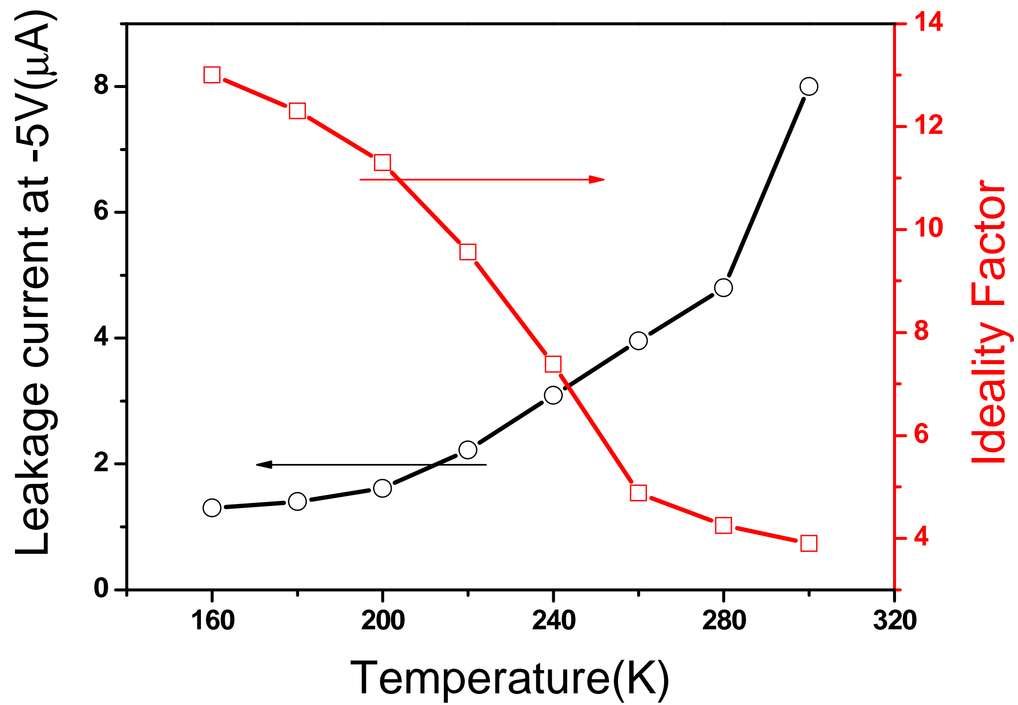

Fig. 5.10 Leakage current at -5V and the ideality factor as a function of temperature.

5.6. Optical properties of heterojunctions grown on MgO substrates

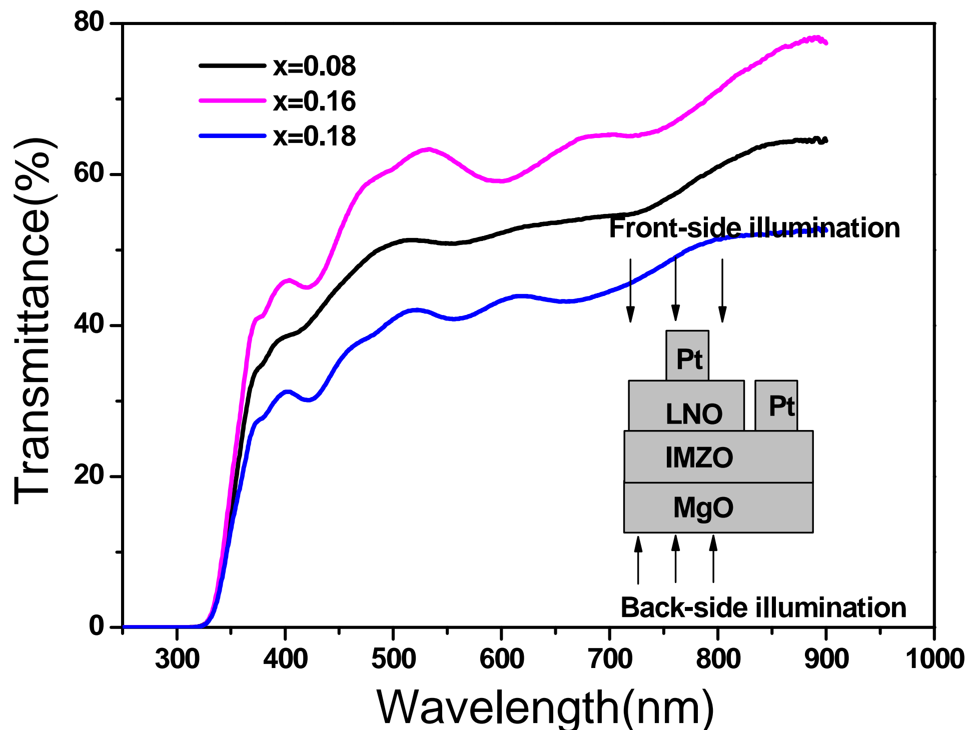

Fig. 5.11 Optical transmittance spectra of *p*-LNO/*n*-IMZO heterojunctions with different In content (x) of 0.08, 0.16 and 0.18 in the target respectively. The inset is the configuration of front-side and back-side illumination.

Figure 5.11 illustrates the transmission profiles of *p*-LNO/*n*-IMZO heterojunctions with indium content of 0.08, 0.16 and 0.18. All heterojunctions show sharp absorption edges and average transmittance of over 40% in the whole visible spectrum. In changing the indium content in the *n*-type layer, the absorption edge remains at 332 nm. This clearly suggests that the transmittance of these heterojunctions is dominated by the LNO layers. Three samples exhibited with difference percentage of transmittance in the visible spectrum. Their variation is primarily due to the variation in the thickness of LNO layers. When the indium content(x) is equal to 0.16, the sample has an average

transmittance of over 60%. Therefore, these *p*-LNO/*n*-IMZO heterojunctions show optical absorptions in the UV range. Further studies of photoresponse of these heterojunction should be explored.

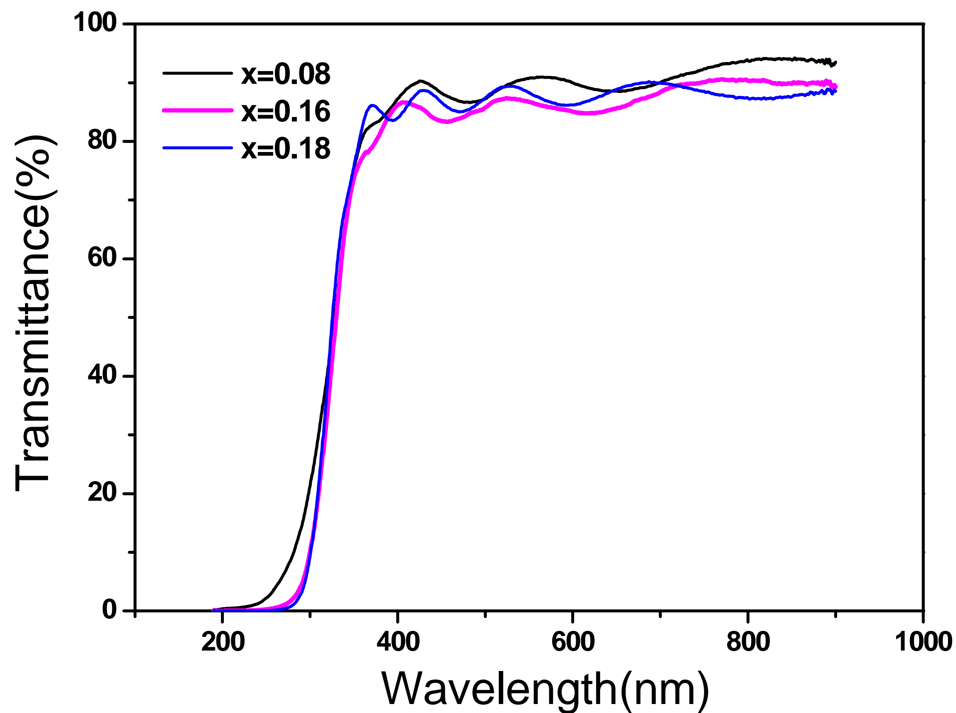

Fig. 5.12Optical transmittance spectra of *n*-IMZO film with different In content (x) in the target.

Figure 5.12 shows the transmission spectra of IMZO films with different indium content. All samples exhibit sharp absorption edge and high transmittance of about 90% in the visible range. With increasing indium content, the absorption edge can be tuned from 250 to 310nm. This tunable cutoff wavelength of *p*-LNO/*n*-IMZO photodiode can cover the whole UV solar-blind spectral range. In subsequent optical characterizations *p*-LNO/*n*-IMZO photodiode with x=0.16 and 0.18 were used.

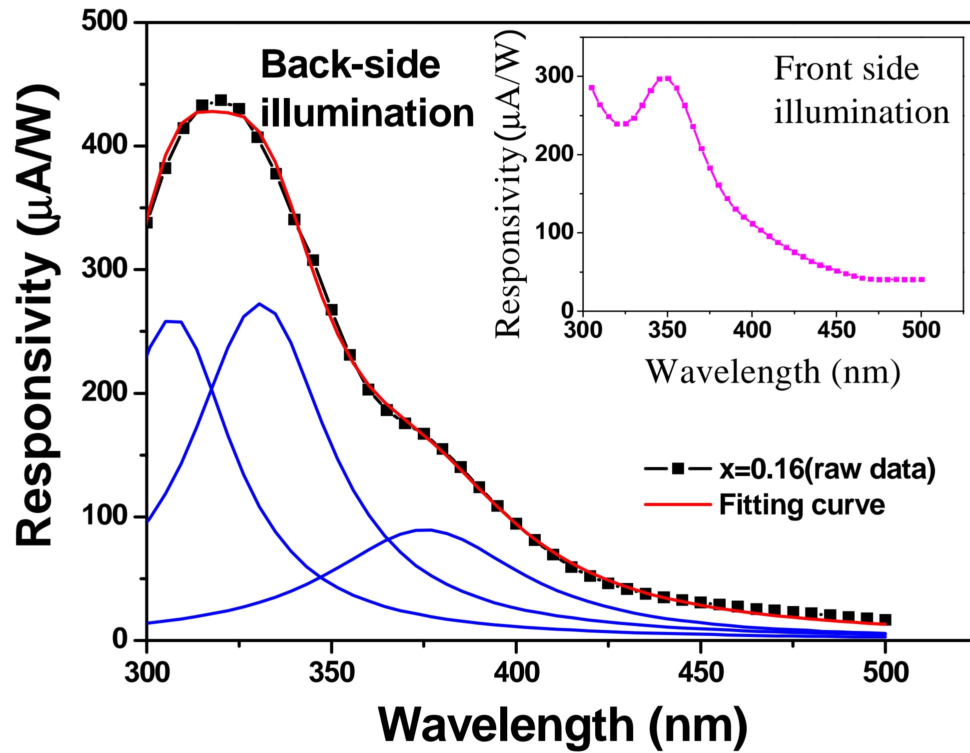

Fig. 5.13 Spectral responsivity of the *p*-LNO/*n*-IMZO heterojunctions on MgO substrate under back-side illumination when x=0.16 in the target. The corresponding Lorentzian fit peaks are 307, 330 and 375 nm respectively. The inset shows the spectral response of these heterojunction under front-side illumination.

The *p*-LNO/*n*-IMZO heteroepitaxial structure, as shown in the inset of Fig. 5.11, allows for both front-side and back-side illumination. MgO substrate is a good transmission window for UV to VIS transmission over the wavelength range of 200-900 nm. Figure 5.13 and 5.14 shows the responsivity spectra and quantum efficiency of the *p*-LNO/*n*-IMZO heterojunction irradiated on front-side and back-side (inset) illumination at zero bias voltage in a range of wavelength 300-500 nm respectively.

Interestingly, the peak responsivity at wavelength 350 nm on the front-side and 320nm on back-side illumination were detected. The photoresponse mechanism of this heteroepitaxial junction could be understood by the transmittance profile of LNO and IMZO films.

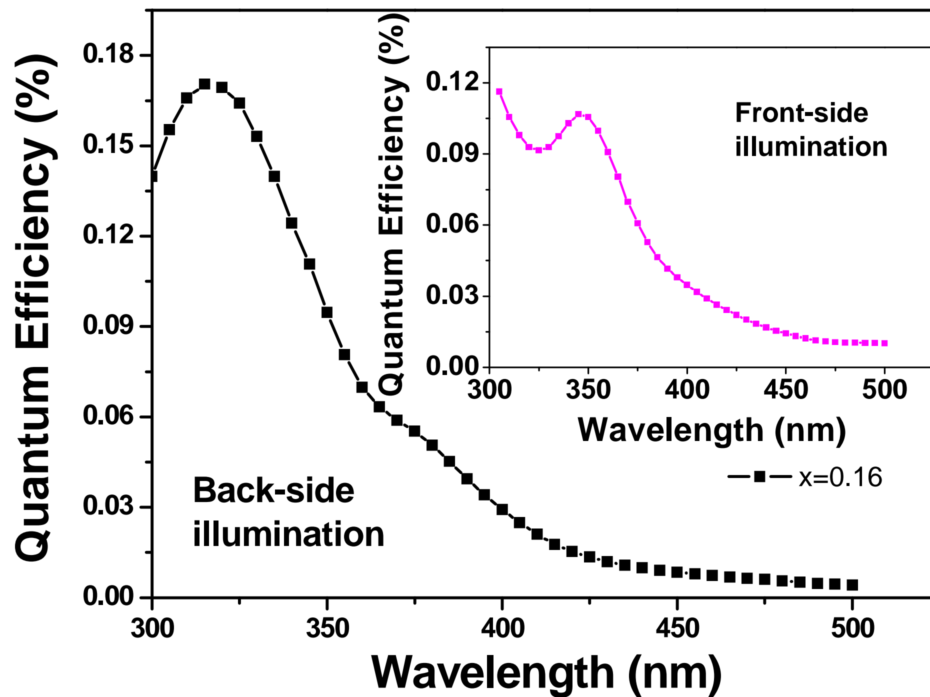

Fig. 5.14 Quantum Efficiency of the *p*-LNO/*n*-IMZO heterojunctions on MgO substrate under back-side illumination when x=0.16 in the target.

Under the front-side illumination, a high responsivity was observed at wavelength from 334 to 365 nm, which corresponds to the near band edge absorption of LNO, whereas no photoresponse was observed due to the band-to-band absorption of IMZO at 300 nm. Indeed, the UV light with a wavelength shorter than 365 nm is absorbed the LNO layer, which results a photogenerated electron-hole pairs. Given that the film is of 100 nm thick and the optical absorption of LNO in these UV regions is strong, it was believed

that these UV light was completely absorbed in this layer. The photogenerated electrons diffuse to the depletion layer. Then these carriers were swept by build-in electric field, which contributes to the photocurrent in the UV region. Therefore, the *p*-LNO/*n*-IMZO heteroepitaxial junction showed a high responsivity with wavelength of 350 nm under front-side illumination.

To understand the spectral responsivity of these heterojunction under the back-side illumination, it was necessary to consider the optical property of IMZO films first. The UV light with a wavelength shorter than 320 nm is completely absorbed by IMZO layer. These results are photogenerated electron-hole pairs. And it was observed that the IMZO film is highly transparent (>90%) in the range of 320-500 nm. Therefore, light with a wavelength from 320 to 500 nm passes through the IMZO layer and is absorbed by the impurity or defects states at the interface and by the underlying *p*-LNO. The highest responsivity was obtained in the wavelength range from 300 to 340 nm, which is in a good agreement with the bandgap of IMZO when x=0.16. The maximum responsivity is $4.37x10^{-4}$ A/W at wavelength of 320nm. The present results give an UV/visible rejection ratio of more than 40. The photoresponse with the wavelength at 330nm is likely due to the band-to-band transition of the LNO layer. The relatively weak response at the blue spectral region can be attributed to absorption caused by impurity or defects states at the interface. Clean and defects free interface in the heterojunction can certainly improve the performance of this *p-n* junction based photodetectors.

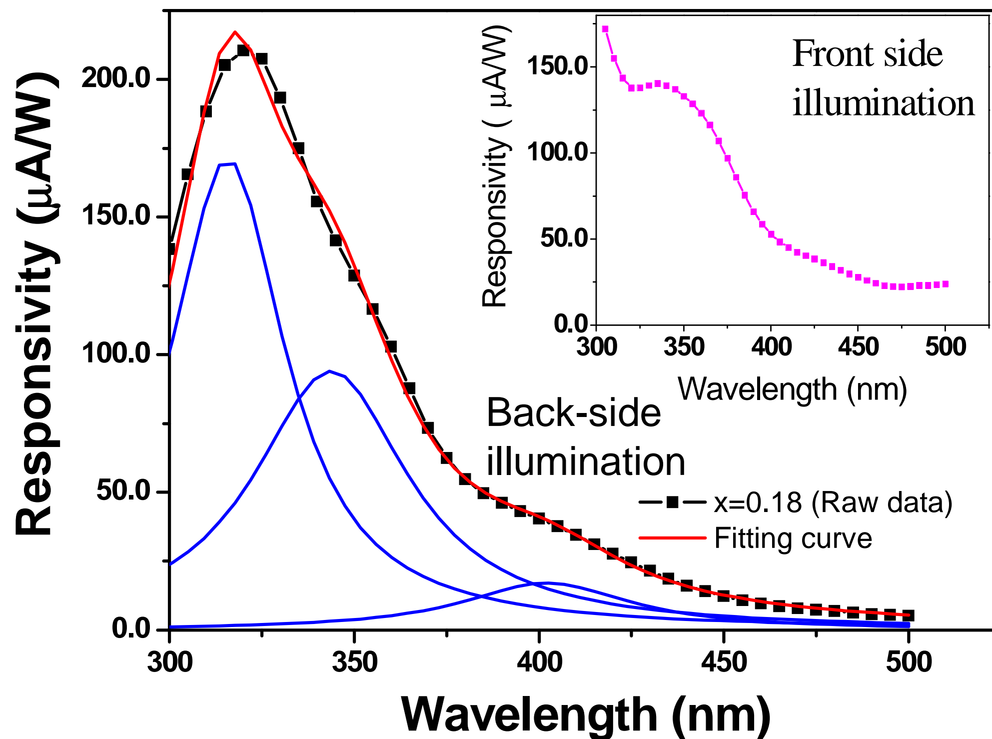

Fig. 5.15 Spectral responsivity of the *p*-LNO/*n*-IMZO heterojunctions on MgO substrate under back-side illumination when x=0.18 in the target. The corresponding Lorentzian fit peaks are 315, 343 and 402 nm respectively. The inset shows the spectral response of these heterojunction under front-side illumination.

It is expected that the cutoff wavelength in the spectral response can be varied by changing the indium content in the *n*-IMZO layer. The spectral response and quantum efficiency of the heterojunction(x=0.18) under back-side illumination at zero bias voltage in a range of wavelength 300-500 nm are shown in Fig. 5.15 and Fig. 5.16. The corresponding front-side illumination profile is depicted in the inset. For the back-side illumination, the spectral response spectrum of the *p*-LNO/*n*-IMZO heterojunction

shows a fitting peak of shifts from 307 to 315 nm, when the indium content changes from 0.16 to 0.18. This shift in the fitting peak is due to the tunable bandgap of IMZO upon increment the indium content in the *n*-type layer. This is consistent with the decrease trend in the cut-off wavelength, which is mentioned in Fig. 3.11.

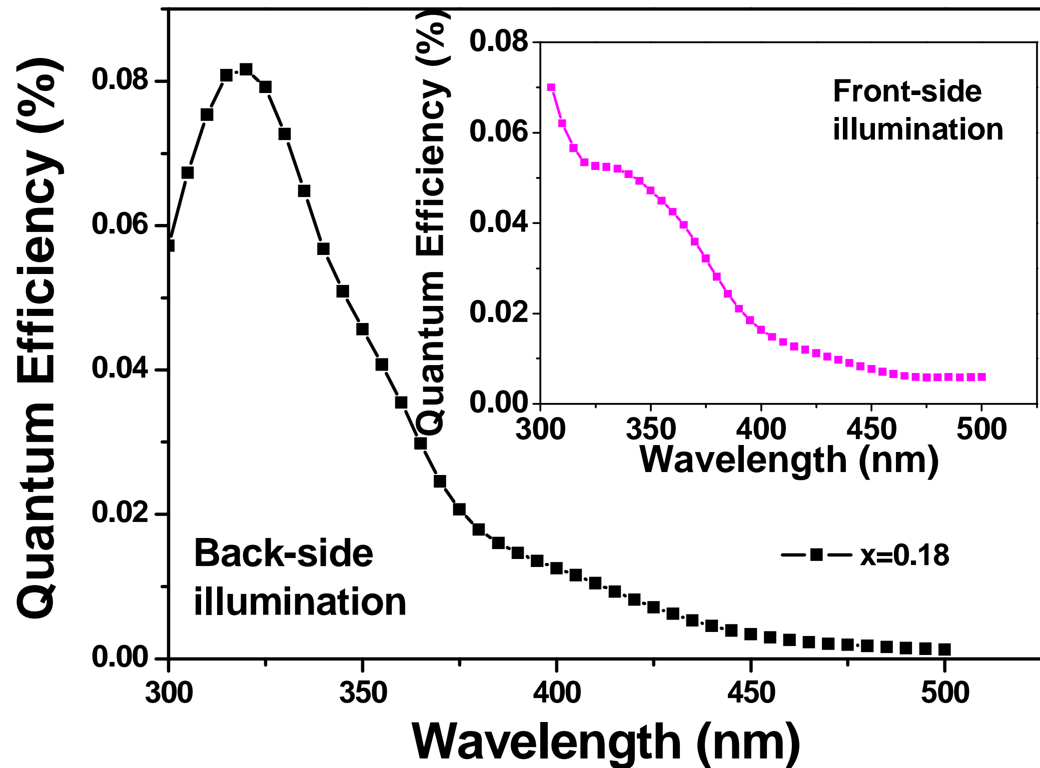

Fig. 5.16 Quantum Efficiency of the *p*-LNO/*n*-IMZO heterojunctions on MgO substrate under back-side illumination when x=0.18 in the target.

5.7. Summary

Cubic phase *p*-LNO/*n*-IMZO heterojunctions with different indium doping concentration of 0.08, 0.16 and 0.18 were successfully grown on MgO(001) substrate by PLD. Cube-on-cube epitaxial relationship of LNO(001)|| IMZO(001)||MgO(001) was obtained. With increasing indium content, the diffraction peak of IMZO(002) shifts toward smaller diffraction angle, implying that the lattice constant of IMZO can be adjusted by changing indium doping concentration of *n*-IMZO layer. And the lattice mismatch between LNO and IMZO increases from 2.8% to 4.8% upon increasing the indium content in the *n*-type layer.

All heterojunctions show good rectifying current-voltage characteristics. A maximum current rectifying ratio of 169 is obtained for an applied voltage of +4 to -4V when x=0.16. Increase trend in the ideality factors of this heterojunction is attributed to the increase in the lattice mismatch between LNO and IMZO layers, which increases the probability of defect-assisted tunneling and carrier recombination in the space charge region via interface states. In the temperature dependent current-voltage characteristics, the current transportation mechanism is dominated by the tunneling through the barrier or the generation-recombination process occurring in the depletion region.

Solar blind UV photodetector with peak spectral response at wavelength 320nm has been realized based on *p*-LNO/*n*-IMZO heterojunction. This photodetector shows a UV/visible rejection ratio of more than 40 under back-side illumination configuration. Upon increasing the In content in *n*-type layer, the fitting peak of responsivity shifts from 307 to 315 nm.

Chapter 6. Structural, electrical and optical properties of LNO/IMZO heteroepitaxial junctions grown on TiN buffered Si(001) substrates

6.1. Introduction

ZnO has a direct band gap of 3.27 eV and high exciton binding energy of 60 meV. When it is alloyed with MgO, the transition band gap energy can be tuned from 3.37 to 3.87 eV [6.1]. Indeed band-gap engineering of epitaxially grown $Zn_xCd_{1-x}O$ and $Zn_xMg_{1-x}O$ films have been demonstrated [6.2, 6.3]. Recently, Lin *et al.* [6.4] have also reported that the band-edge luminescence intensity of $Zn_{0.973}Mg_{0.027}O$ film at room temperature is nearly six times higher than that in pure ZnO film. It is believed that $Mg_xZn_{1-x}O$ (MZO) can be an excellent material for photonic applications such as UV detector, blue and UV light-emitting diode, and laser diode [6.5–6.8]. For these purposes, we need to fabricate MZO based high quality *p–n* junction diodes on Si wafer substrates. Up-to-date *p*-type doping of ZnO or MZO remains difficult and homoepitaxial MZO *p–n* junction has not been realized. An alternative approach is to grow *n*-type MZO on other lattice matched *p*-type semiconducting oxides to form heteroepitaxial junctions. The integration with Si, on the other hand, can be accomplished via refractory buffer layers such as TiN [6.9]. There are a number of *p*-type conducting oxides available. Noted ones include manganates and nickelates. TiN has a simple cubic structure with a lattice constant of 4.2 Å. In these respects, the cubic phase of MZO is highly desirable.

Choopun et al. [6.10] reported that phase transition from hexagonal to a rocksalt simple cubic structure occurred in the MZO films grown by pulsed laser deposition (PLD)

technique with MgO content higher than 45%. This structural change came about originally from the two phase structures of ZnO: wurtzite and cubic structure. Wurtzite ZnO is very stable in ambient pressure. In contrast, the cubic form of ZnO only exists under high pressure at 100 kbar or above [6.11]. Apparently the high concentration of cubic rocksalt MgO induces formation of the cubic ZnO phase. We also believe that epitaxial growth on appropriate lattice matched cubic phase single crystal substrate can also help to stabilize the cubic MZO under the normal ambient. Our group has successfully demonstrated single-phase domain matching growth of epitaxial cubic MZO films on $LaAlO_3$ substrates [6.12].

In our recent study, epitaxial In-doped cubic MZO films have also been fabricated. Using a 18% In-doped $Mg_{0.5}Zn_{0.5}O$ (IMZO, when x=0.18) PLD target, films with low resistivity of about 1×10^{-2} Ω-cm have been obtained. The optical transmittance over the whole visible spectrum is more than 90% [6.13]. As a result, IMZO can be utilized as a cubic structured transparent conducting oxide (TCO). Nickel oxide (NiO), having a cubic structure, is a *p*-type semiconductor with a bandgap of 3.7 eV. In order to increase the conductivity in NiO, Li^+ ion doping is introduced to raise the hole concentration [6.14, 6.15]. 15% Li doped NiO (LNO) is used as the *p*-type layer for our heteroepitaxial *p*–*n* junction.

In this chapter, the fabrication of *p*-LNO/*n*-IMZO heteroepitaxial junction grown on TiN buffered Si using PLD is reported. A detail study of film growth condition and the structural, optical and electrical properties of this heteroepitaxial junction are presented.

6.2. Experimental details

Heteroepitaxial *p–n* junctions were grown on TiN buffer Si rather than directly on Si(100) substrate. Due to the large lattice mismatch between IMZO (4.43 Å) layer and Si (5.43 Å) substrate, TiN buffer layer was employed between IMZO film and Si substrate. There are several advantages of introducing TiN layer: (i) preventing chemical diffusion between IMZO and Si; (ii) low resistivity of the TiN layer (15 uΩ-cm) can be regarded as the conducting bottom electrode for the *p–n* junction [6.16]; (iii) to achieve cube-on-cube epitaxial growth due to less than 4 % lattice mismatch between IMZO and TiN.

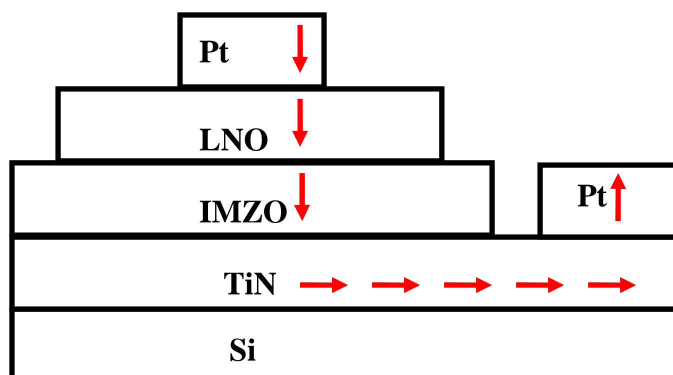

Fig. 6.1 The schematic diagram of *p*-LNO/*n*-IMZO heterojunctions on TiN buffered Si. The arrow is the flow of the electron.

The heteroepitaxial diodes of *p*-LNO/*n*-IMZO on TiN buffered *n*-Si (100) with different In content (target) of 0.08, 0.16 and 0.18 in the *n*-type layer were deposited by PLD. A schematic layout of the diode configuration is shown in Fig. 6.1. The advantage of this design is that TiN, having low resistivity (15 uΩ-cm), provides electrical path for the *p-n* junction. So now the current-voltage characteristics can more truly reflect the performance of the junction.

Prior to loading into the chamber, Si(001) substrate wafers were cleaned by ultrasonically for 5 min in acetone and then 5 min in ethanol, followed by etching in 10% HF solution in order to remove the native oxide. The deposition chamber was evacuated to base pressure of about 3 x 10^{-5} Torr by a turbo-molecular pump. A KrF Excimer laser was used to ablate the hot-pressed stoichiometric TiN target. Substrate temperature was kept at 600 °C during the growth of the TiN layer. The sample was then annealed *in situ* at the same growth temperature for 20 min to improve the crystalline structure. After the deposition of 100 nm thick TiN buffer layer, an IMZO layer was grown on TiN under an oxygen ambient pressure of 4 x 10^{-5} Torr. The substrate temperature was kept at 600 °C. The final IMZO film was about 500 nm thick. LNO was subsequently grown at 600 °C with oxygen pressure of 150 mTorr. Using stainless steel mask with regular arrays of 500 ×500 μm^2 openings, 100 nm of LNO film was deposited through the holes of the mask, resulting isolated flat LNO square islands on top of the IMZO layer. Circular spot platinum electrodes of 200 μm in diameter were finally deposited at room temperature on the LNO islands via another properly shaped and aligned mask by PLD.

The crystalline structure of the heteroepitaxial junctions were characterized by an x-ray diffractometer (Phillips model X'pert system) operated in four-circle-mode. Keithley 2400 and 6517A were used to evaluate the electrical properties. Spectral response of this junction was examined over a wavelength range of 300–500 nm by Xenon lamp.

6.3. Characterization of TiN deposited on Si(001) substrates

6.3.1. TiN bulk Target

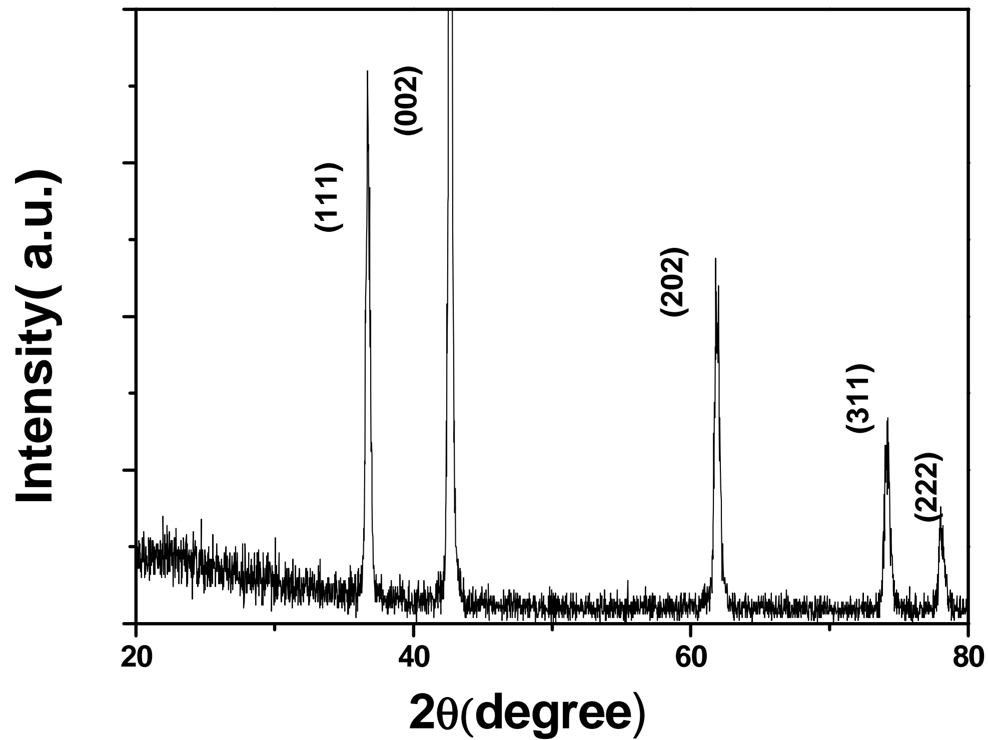

Fig. 6.2 The X-ray diffraction pattern of hot-press sintered TiN ceramics target.

Hot-press stoichiometric TiN target with 99.5% purity, bought from Electronic Space Products International Company (ESPI), was employed as the PLD target. Figure 6.2 shows the 2theta-theta scan of these TiN targets. All diffraction peaks are assigned to the crystal plane of TiN.

6.3.2. Structural properties and surface morphology of TiN film

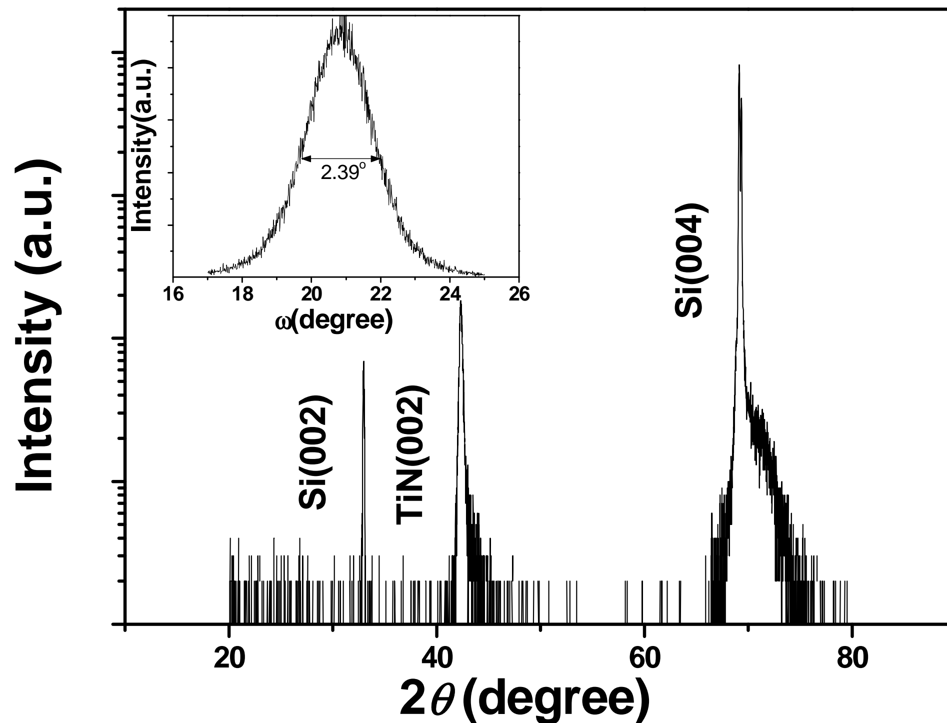

Fig. 6.3 X- Ray diffraction patterns of *θ*-2*θ* scan of TiN deposited on Si(100) substrate. The inset is the rocking curve of (002) peak of TiN film.

The x-ray diffraction spectra of TiN films deposited on *n*-type Si(001) substrate are shown in Fig. 6.3. Besides the diffraction peaks from Si(004) and Si(002), only one peak located at 42.32^o is observed. This is attributed to the diffraction from TiN(002). The lattice constant of TiN is 4.26 Å, which is slightly smaller than the bulk materials (4.27 Å), suggesting compressed strain induced lattice distortion. This induced strain is due to nitrogen deficient in the crystal structure of TiN. As shown in the inset of Fig. 6.3, the FWHM of TiN(002) is about 2.39^o , which suggests the TiN layer is well oriented on the Si substrate.

Figure 6.4a shows the SEM image of the as-grown film. The film is almost uniform, clean and crack-free. Figure 6.4b shows the AFM images of TiN film grown on the Si substrate measured over a 1 x 1 μm^2 scanning range. The surface roughness is about 1.10nm and this result is comparable with other previous report [6.17]. In summary, high quality crystalline of TiN film with flat and crack-free surface has been successfully grown on Si substrate.

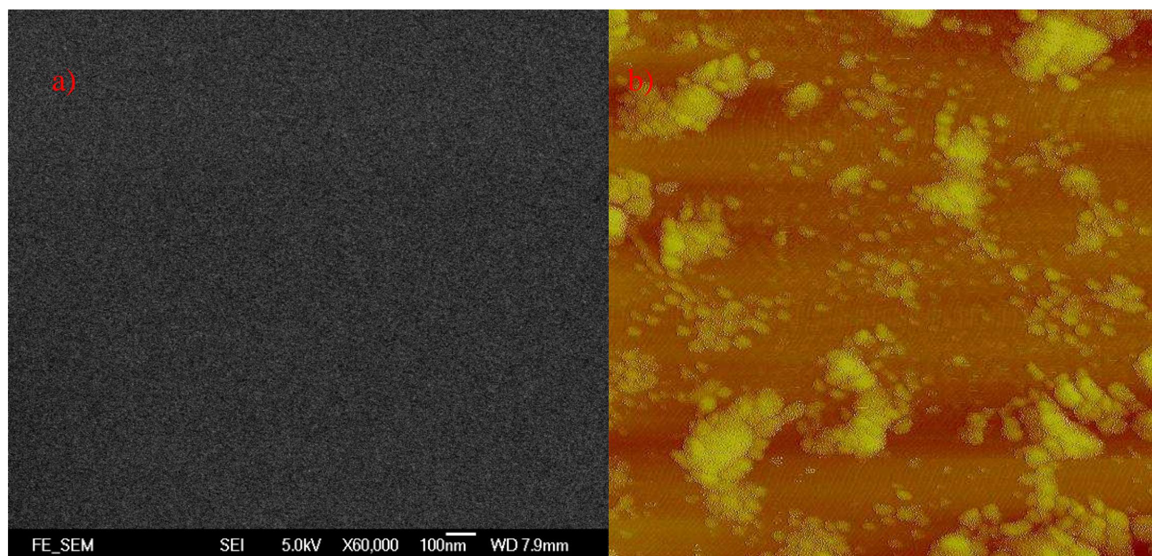

Fig. 6.4 The SEM and AFM images of the surface morphology of TiN deposited on Si substrate.

6.4. Structural properties of heterojunctions on TiN buffered Si

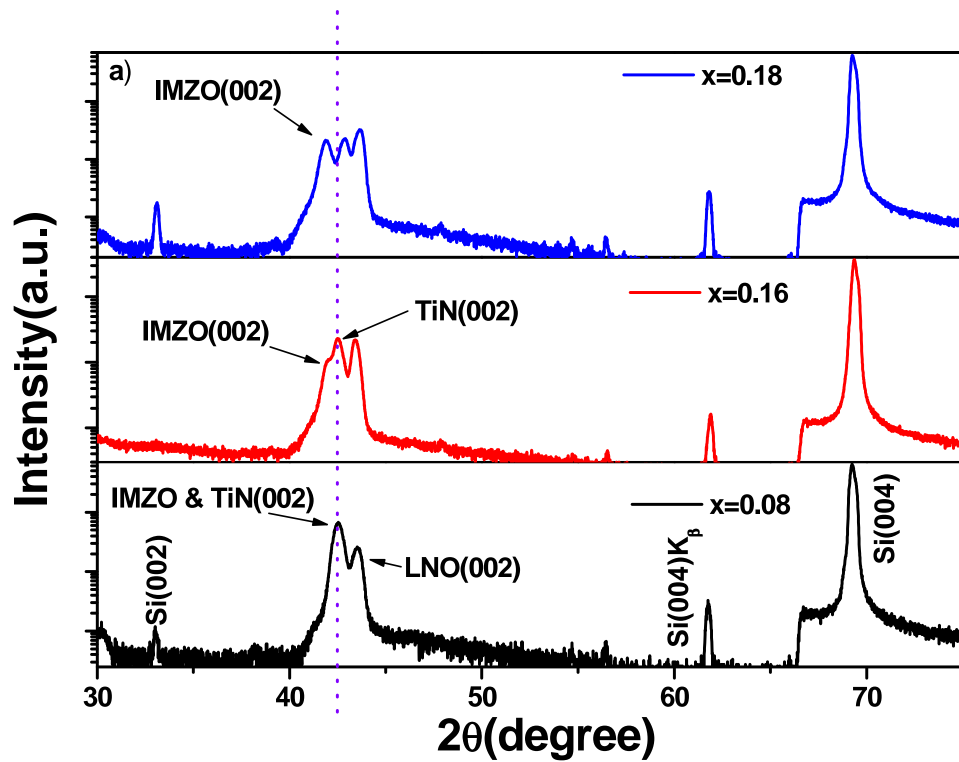

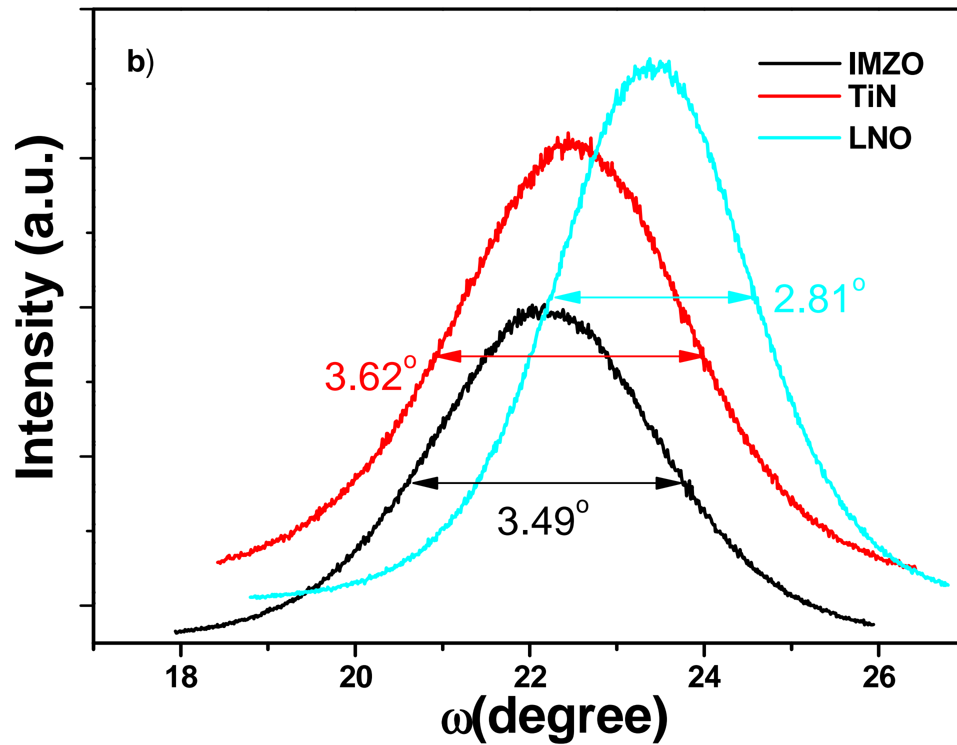

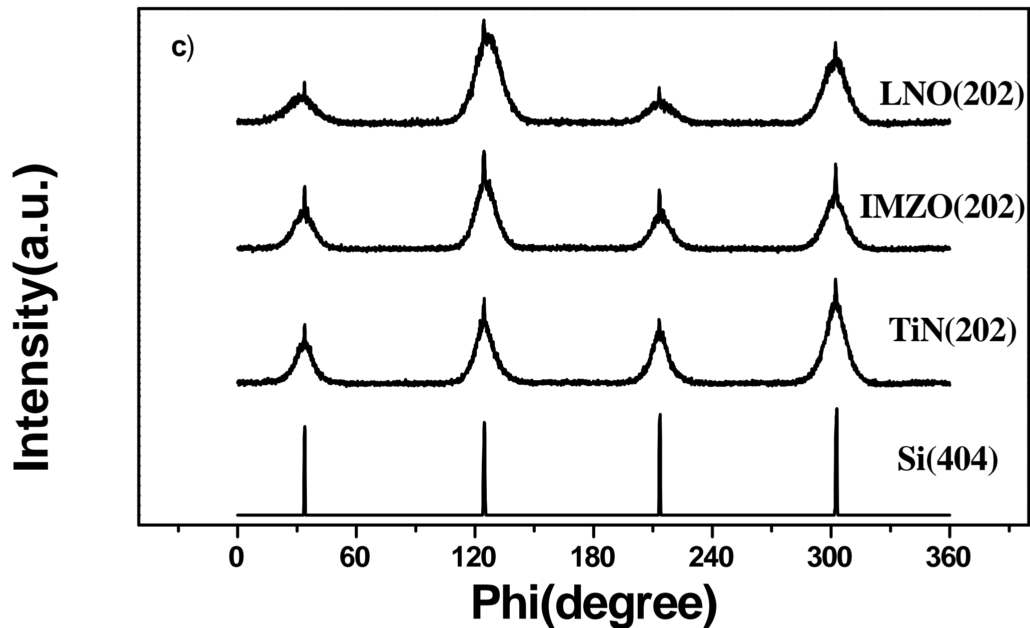

Fig. 6.5 XRD for *p*-LNO/*n*-IMZO heterojunctions deposited on TiN buffered Si(001) with different In content of 0.08, 0.16 and 0.18 in the target: (a) θ-2θ scans, (b) the rocking curves of (002) peak of IMZO, TiN and LNO when x=0.18, (c) Phi scan measured from (202)LNO, (202)IMZO, (202)TiN and (404)Si when x=0.18.

The structural properties of *p*-LNO/*n*-IMZO heterojunctions with different indium content (x= 0.08, 0.16 and 0.18) fabricated on TiN buffered Si were characterized by XRD. Figure 6.5a shows the XRD θ-2θ scan of these *p*-*n* heterojunctions. Besides the diffraction peak from Si(002), Si(004) and Si(004)CuK$_b$, sharp diffraction peaks of IMZO(002), TiN(002) and LNO(002) can be seen. This indicates that all layers are grown with cubic structure with preferentially (002) orientation.

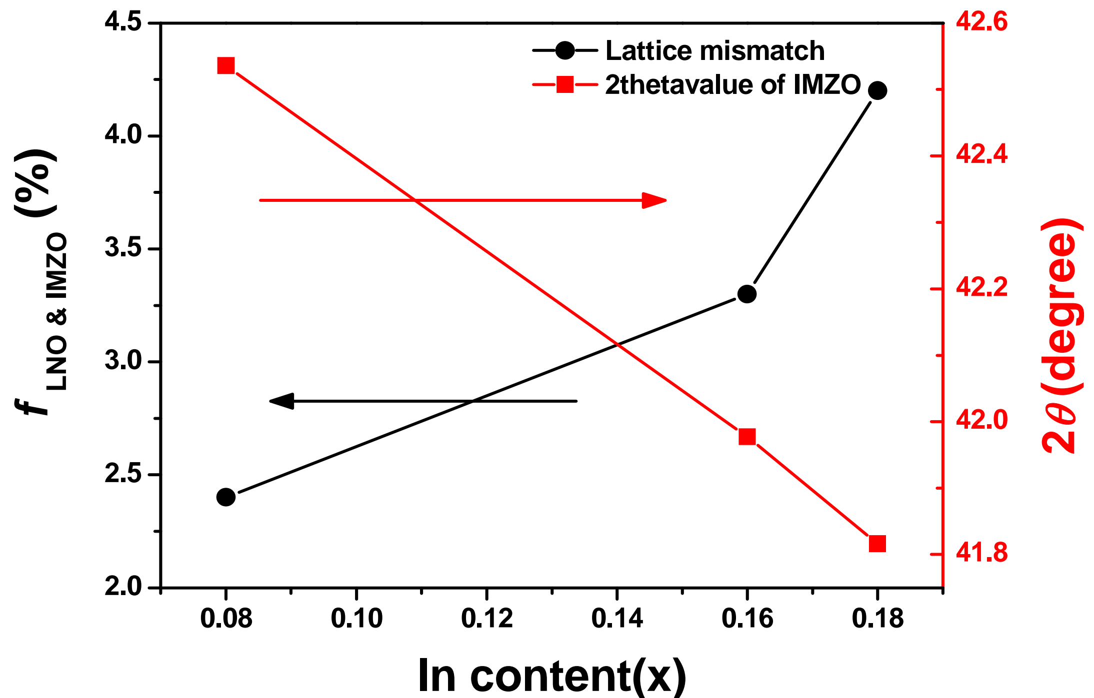

Fig. 6.6 The lattice mismatch between LNO and IMZO, $f_{LNO\vartheta IMZO}$, and the 2 theta values of IMZO with different In content (x) in the target.

Figure 6.6 shows the lattice mismatch between LNO and IMZO with different indium content. With increasing the indium content in the IMZO layer, the diffraction reflections of IMZO(002) shifts to lower angle side, indicating the incorporation of In^{3+} ions into the lattice of the MZO. Thus, the lattice mismatch between LNO and IMZO increases from 2.4 to 4.2 %. This is consistent with the structural properties of *p*-LNO/*n*-IMZO heterojunctions grown on MgO substrate as described in Chapter 5. Figure 6.5b shows the XRD ω scan of IMZO(002),TiN(002) and LNO(002) when x=0.18. The FWHM of (002) plane of IMZO, TiN and LNO are 3.49°, 3.62° and 2.81° respectively. The poor crystalline quality of these films is due to the poor crystal quality of TiN template layer. Figure 6.5c shows XRD in-plane Phi scan for plane (202) of the LNO, IMZO and TiN reflections. Four Phi-scan peaks at 90° intervals confirm the

cube-on-cube epitaxial relationship of LNO(001)|| IMZO(001)||TiN(001)||Si(001).

6.5. Electrical properties of heterojunctions on TiN buffered Si

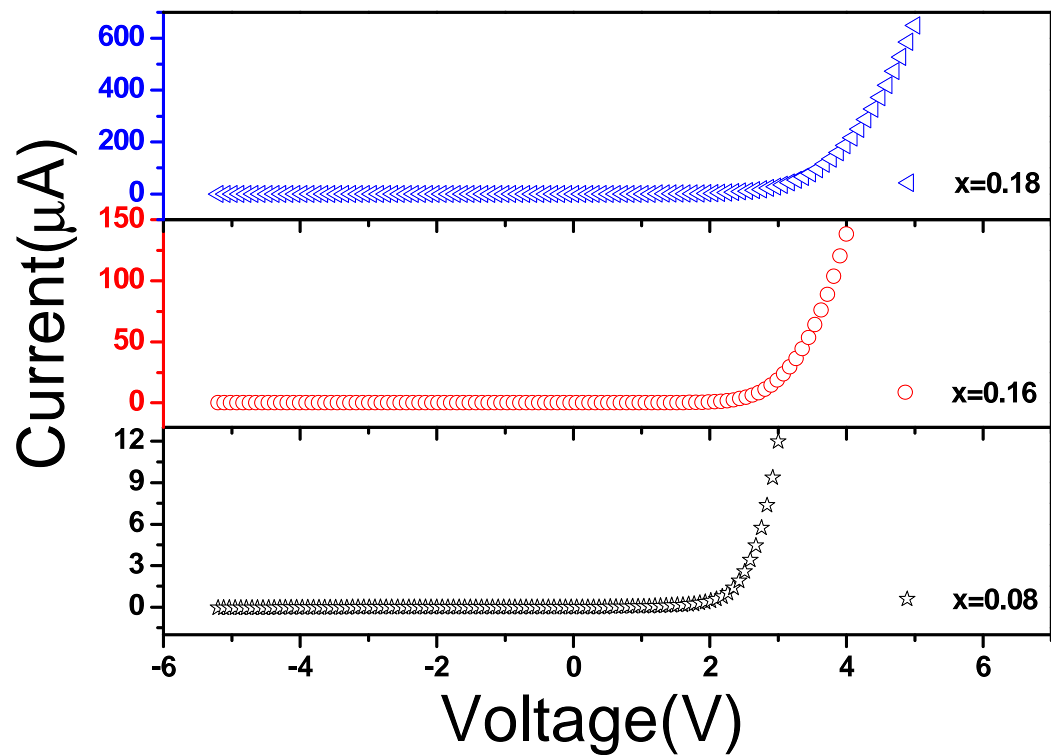

Fig. 6.7 ***I-V*** **curve of** ***p*****-LNO/*****n*****-IMZO heterojunctions on TiN buffered Si(001) substrate with different In content (x) 0.08, 0.16 and 0.18 in the target respectively.**

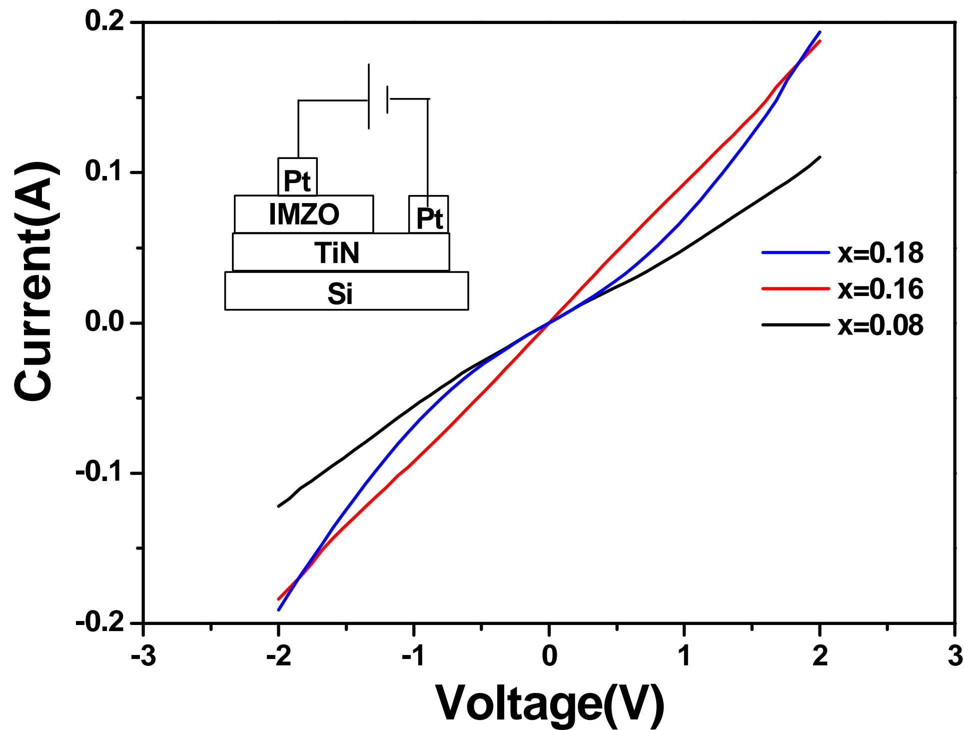

Fig. 6.8 ***I-V*** **characteristics between the two platinum electrodes on the IMZO film with different In content (x) in the target.**

The *p-n* junction is evaluated by the electrical measurements. Figure 6.7 shows the typical current- voltage characteristics of the *p*-LNO/*n*-IMZO heterojunctions fabricated on TiN buffered Si with different In content (x) of 0.08, 0.16 and 0.18 in the *n*-type layer. Symmetrical *I-V* characteristics of Pt/IMZO/TiN/Pt when x=0.08, 0.16 and 0.18 are shown in Fig. 6.8. The ohmic contacts of Pt/IMZO/Pt and Pt/LNO/Pt were mentioned in Chapter 4. Thus, good electrical rectifying characteristics of all the heterojunctions come from the *p-n* junctions rather than other semiconductor and metal contact. Moreover, the *I-V* properties of these heterojunctions were affected by electrical properties of the *n*-type layer. Upon increase the indium content from x= 0.08 to 0.16 in the *n*-type layer, the current of this heterojunction increases a factor of 2 at 3V

of forward bias voltage. Among these samples, the maximum current can be obtained from *p*-LNO/*n*-IMZO heterojunctions when x= 0.18. It can be concluded that increase of the indium content in the *n*-IMZO layer can effectively improve the electrical performance of *p*-LNO/*n*-IMZO heterojunctions. It is due to the improvement of conductivity as the indium content in the *n*-type layer increases.

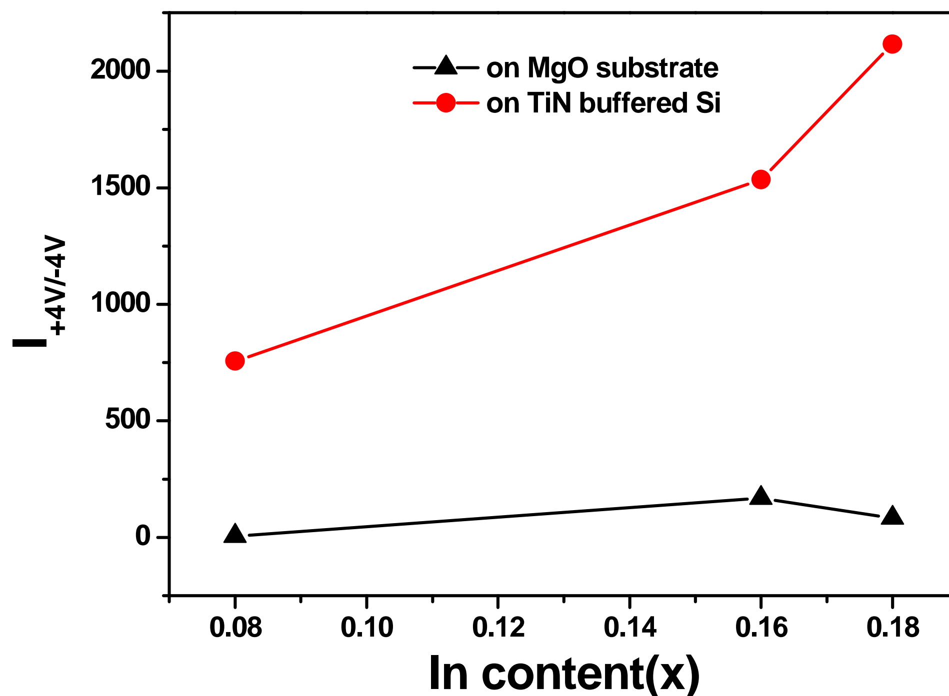

Fig. 6.9 The current rectifying ratio $\frac{I_{4v}}{I_{-4v}}$ of heterojunction fabricated on TiN buffered Si and MgO substrate with different In content (x) in the target.

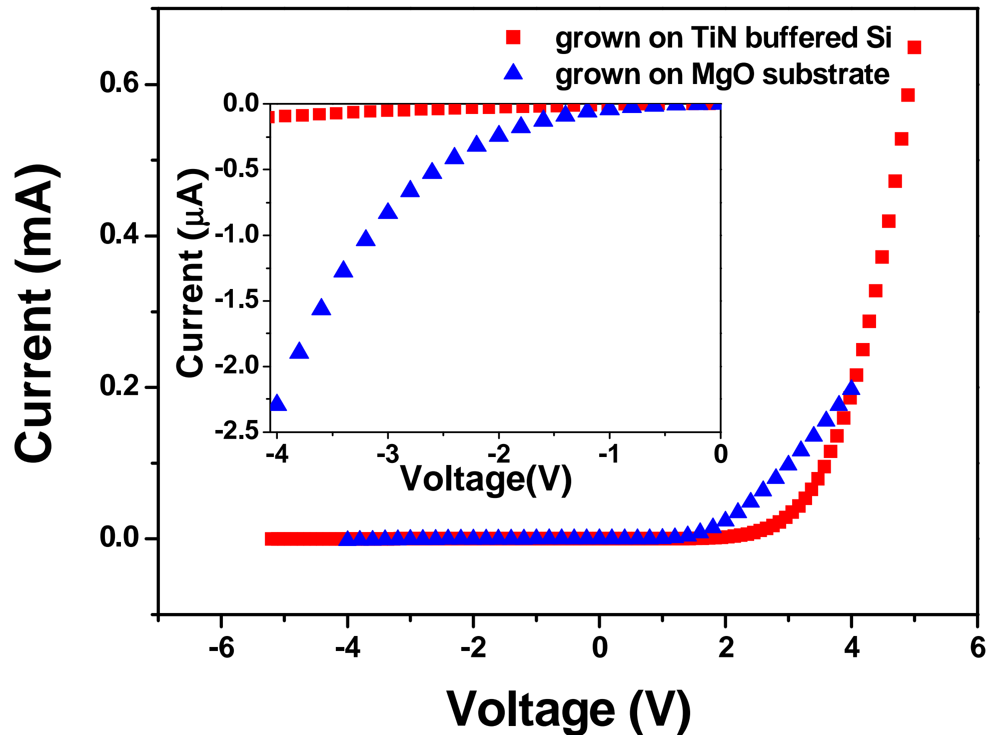

Fig. 6.10 *I-V* curves of *p*-LNO/*n*-IMZO heterojunctions grown on TiN buffered Si(001) and MgO(001) substrate when x= 0.18 in the target.

Figure 6.9 shows the current rectifying ratio of heterojunction fabricated on different substrates. Using TiN buffered Si instead of MgO as substrate, the current rectifying ratio increased by a factor of 10. Current-Voltage characteristics of *p*-LNO/*n*-IMZO heterojunction grown on MgO and TiN buffered Si when x=0.18 are shown in Fig. 6.10. The heterojunction deposited on TiN buffered Si exhibited a lower leakage current than those on MgO. And the ratio of the forward current to the reverse current reached 4037 in the voltage ranging from +5V to -5V. By contrast *p-n* junction grown on MgO substrate gives a ratio of only 89. It is shown that all heterojunctions grown on TiN buffered Si show better electrical performances than those fabricated on MgO substrate. This is attributed to the TiN layer (15 $\mu\Omega$-cm) that can be regarded as the conducting

bottom electrode for the *p*–*n* junction, and reduces the series resistance of these heterojunctions.

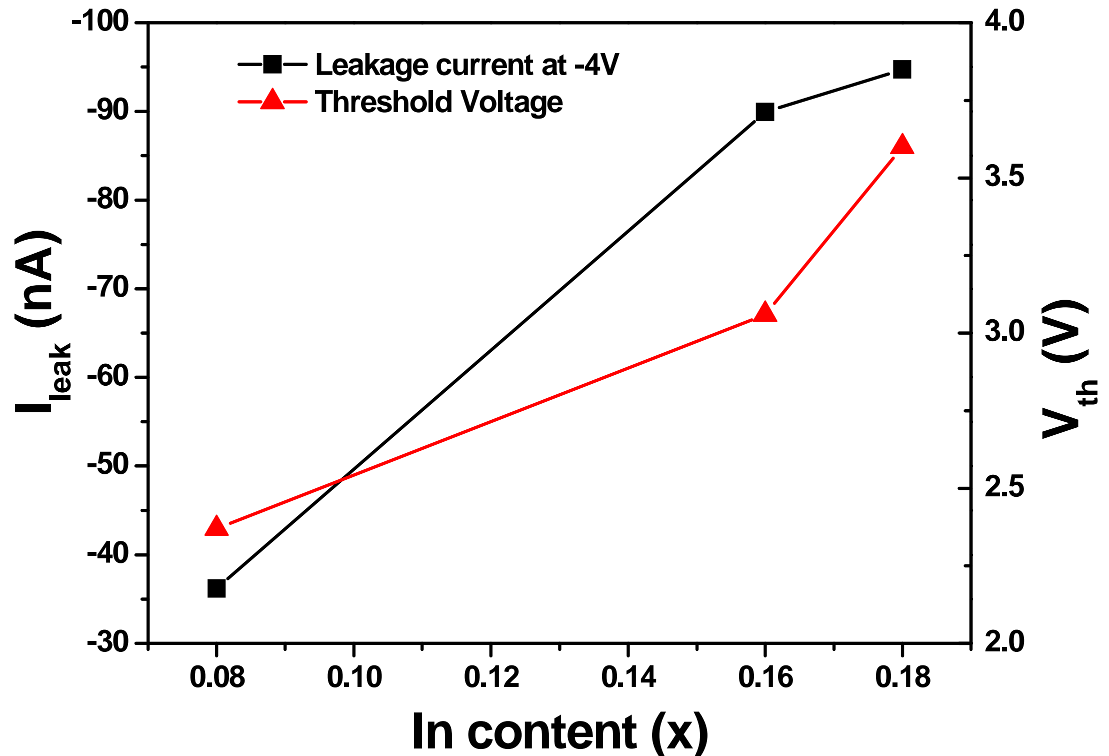

Fig. 6.11 Threshold voltage (V_{th}) and leakage current (I_{leak}) in *p*-LNO/*n*-IMZO heterojunctions with different In content (x) of 0.08, 0.16 and 0.18 in the *n*-IMZO layer (target).

Figure 6.11 shows the threshold voltage and leakage current with different x content in the *p*-LNO/*n*-IMZO heterojunctions. The increase threshold voltage is due to higher built-in potential generated by the difference in Fermi level between *p*-LNO and *n*-IMZO. As the leakage current of the heterojunction increases, the resistivity of *n*-type IMZO should take into consideration. This is attributed to the reverse leakage current consists of hole tunneling from the IMZO region to the LNO region and electron

tunneling vice-versa. Partial replacement of In^{3+} with Mg^{2+} or Zn^{2+} can create more oxygen vacancies, which contributes to the decrease in resistivity. Thus, the leakage current increases with indium oxide content in the *n*-type layer. Moreover, the magnitude of leakage current of the heterojunctions when x = 0.16 and 0.18 grown on TiN buffered Si ranges from 90 to 94 nA in -4V, which is two order of magnitudes lower than those deposited on MgO substrate. And the leakage current of these all oxide based *p-n* junction has been much lower than other previous studies [6.18-6.24]. These results suggest that electrical properties of *p*-LNO/*n*-IMZO heterojunctions on TiN buffered Si can be tuned by the bandgap engineering of IMZO layer.

Figure 6.12 shows the typical Ln(*I*) against V curve of *p*-LNO/*n*-IMZO heterojunction with different indium content in the *n*-type layer. All heterojunction did not exhibit the ideal current-voltage relationship. The ideality factor value increases with In content of a low bias voltage. Such increase suggests that the enlarged in lattice mismatch between LNO and IMZO generates more dislocations in the interfaces. Thus, the electron scattering effect increases.

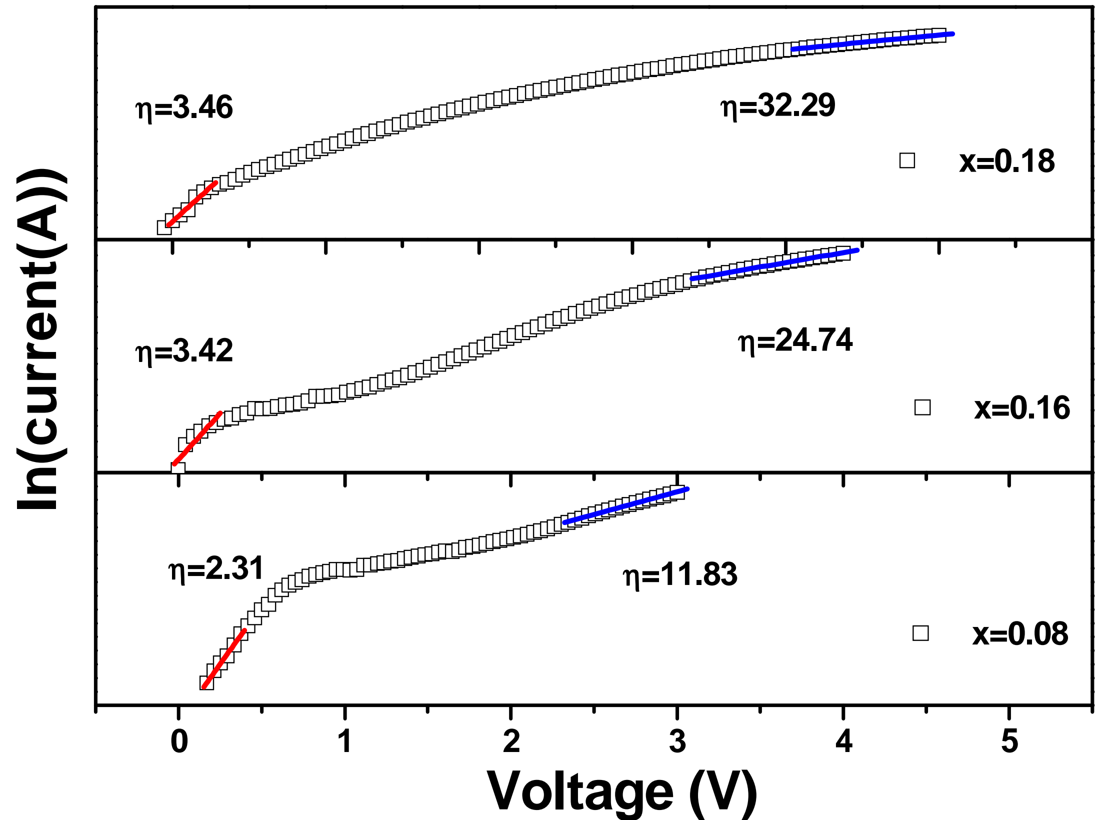

Fig. 6.12 Forward bias Ln(*I*)-*V* curves of *p*-LNO/*n*-IMZO heterojunctions on TiN buffered Si(001) substrates. Exponential fit lines corresponding to ideality factor: in low voltage region (red line): 2.31, 3.42 and 3.46; in large voltage (blue line): 11.83, 24.74 and 32.29 with different In content in the *n*-type layer (target).

From the theory of carrier transport in the diode, the series resistance in the diode will appear to be effective in the limitation of the increase current in the high bias voltage. Figure 6.13 shows the ideality factor at high bias voltage of the heterojunction with different indium oxide content and grown on different templates. The samples grown on TiN buffered Si exhibited lower ideality factor values than those grown on MgO substrate. It is cleared that the TiN buffer layers can serve as a metal-like conducting layer, which can effectively reduce the series resistance of the heterojunctions.

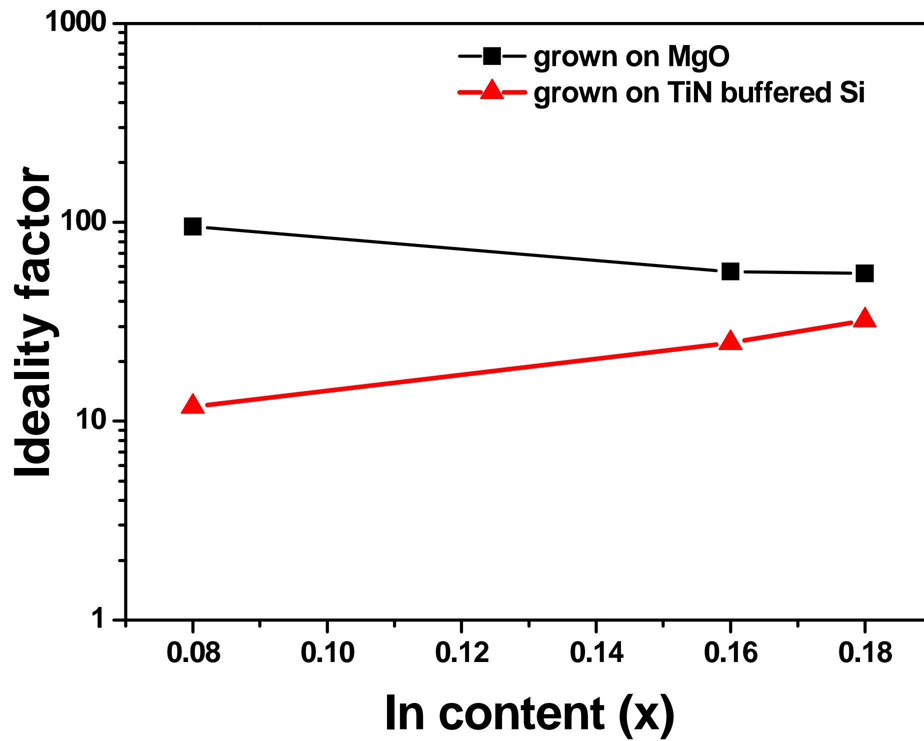

Fig. 6.13 The ideality factor of the heterojunctions with different In content (target) grown on TiN buffered Si and MgO substrate, which are measured at high forward bias voltage.

6.6. Optical properties of heterojunctions on TiN buffered Si

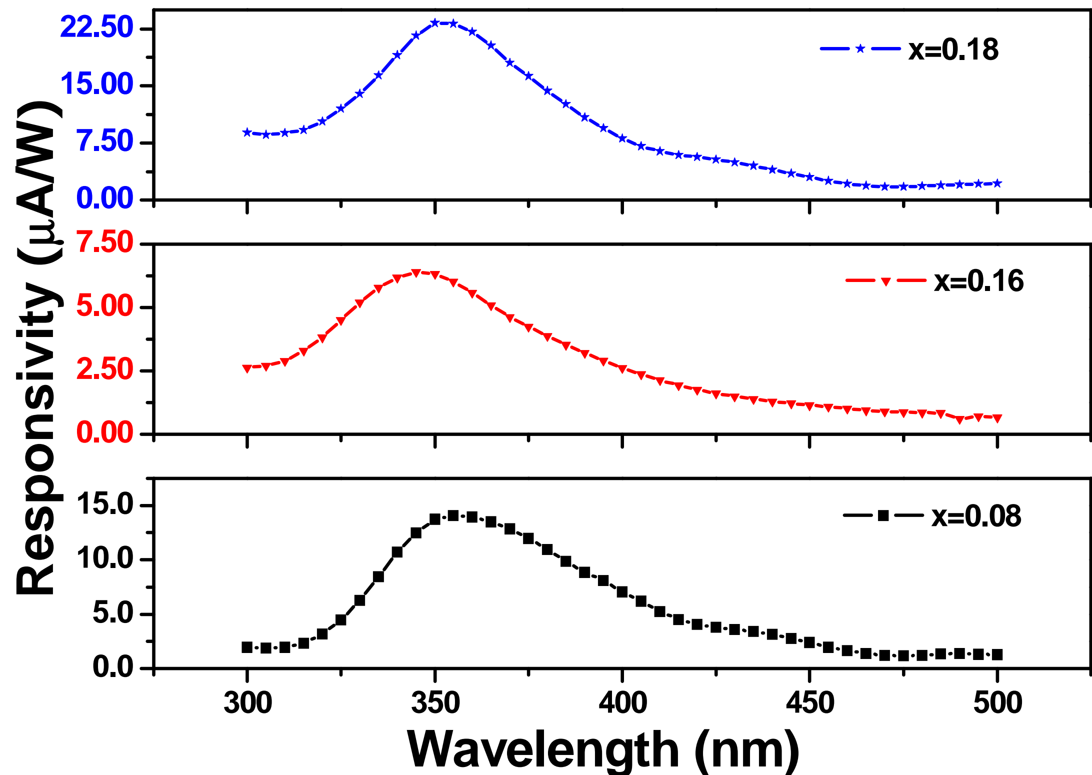

Fig. 6.14 Spectral responsivity of the *p*-LNO/*n*-IMZO heterojunctions on TiN buffered Si substrate with x=0.08, 0.16 and 0.18 in the target.

Spectral response curve of *p*-LNO/*n*-MZO heterojunction at zero bias voltage with different In content in the *n*-type layer are shown in Fig.6.14. These heterojunctions exhibit a strong UV response. The peak optical responses of these heterojunctions are at 350nm, which corresponds to 3.55 eV photon energy. In chapter 4, LNO was reported to exhibit bandgap energy of 3.65 eV for the direct band transition. Bandgap of IMZO with different indium oxide content of 0.08, 0.16 and 0.18 were reported to be 4.97, 4.29 and 4.14 eV respectively. Under illumination, light spectrum passes thought the

LNO first and then the IMZO layer. However, LNO has a smaller bandgap than IMZO. Therefore, LNO were likely to absorb the wavelength below 350nm. The absorption edges of IMZO films with different x content in these heterojunctions have been determined as 250, 290 and 300 nm, according to their transmittance profiles. It is concluded that the peak response of these heterojunctions around 350 nm are primarily due to the band-to-band transition of LNO. The relatively weaker response at the blue spectral region can be attributed to absorption due to defect/impurities states at the interfaces. The present give an UV/Visible rejection ratio of more than a factor of 10 at x=0.18. Better heteroepitaxial diode junction with clean and defects free interface can certainly improve the UV/Visible rejection ratio

6.7. Summary

In conclusion, we have integrated *p*-LNO/*n*-IMZO heterojunctions with Si substrate. Cube-on-cube epitaxy relationship of LNO(001)||IMZO(001)||TiN(001)||Si(001) has been obtained. The application of TiN to the heterojunctions as metal-like conducting electrode has reduced the series resistance of these oxide *p*-*n* junctions.

We have demonstrated that IMZO is an *n*-type semiconductor with controllable resistivity and bandgap by changing the In content. Upon increase the In content in *n*-IMZO layer, these heterojunction exhibits a higher leakage current, higher threshold voltage and higher current rectifying ratio. It has been shown that heterojunctions grown on TiN buffered Si lead to higher current rectifying ratio, lower series resistance and lower leakage current than those grown on MgO substrate. This is a favorable feature for developing future integrated UV devices.

Solar blind UV photodetector with peak spectral response at wavelength of 350 nm has been realized based on *p*-LNO/*n*-IMZO heterojunction on TiN buffered Si. This photodetector shows a UV/visible rejection ratio of more than 10 under front side illumination.

Chapter 7. Conclusion and Further Work

In this work, epitaxial MZO films and IMZO based *p-n* heterostructure diodes with high crystalline and single cubic phase were successfully fabricated on different substrate by PLD. Some of the systematic studies of structural, electrical and optical properties of these IMZO films and IMZO-based devices have been completed.

Epitaxial MZO films with single cubic phase and thickness of 500 nm were successfully grown on MgO(001) and LAO(001) substrates. Incorporation of In_2O_3 into MZO to form *n*-IMZO films causes the IMZO(002) x-ray diffraction peak shifting to lower angles side. Since In^{3+} has larger ionic radius than Zn^{2+} or Mg^{2+}, this is a clear indication that the In atoms have been successfully replacing either Zn or Mg atoms in the MZO lattice. The crystal quality of IMZO films deteriorates at higher In content. The Resistance-Temperature dependence measurements reveal that a semiconducting-like conduction mechanism is dominant in the IMZO films. Upon increasing the In content from 0 to 18%, the resistivity of these films can be changed from 10^7 to 0.01Ω-cm. This is attributed to the free electron generation from the In doping. In optical measurement, the optical bandgap can be tuned from 6.7 to 4.29 eV. All IMZO films exhibits excellent optical transmittance of over 90 % for the whole visible spectrum. Therefore, these IMZO films can be used as UV transparent conducting oxide (TCO) and tunable UV filter for various optoelectronics applications.

To our knowledge good TCO with cubic structure have not been reported. Cubic IMZO films with lattice constant about of 4.2 Å is a convenient size for lattice matched heteroepitaxial growth of many oxides, such as perovskites and transition metal

monoxides. With these advantages in the *n*-IMZO films, we have performed a series of experiments to investigate the processing condition, film thickness, In dopant concentration, and electrical transport properties of these films. The structural and electrical properties showed that the ionized-scattering mechanism rather than the grain-boundary scattering dominates in the IMZO films. The lowest resistivity can be achieved in a 550 nm thick IMZO film is 0.157 Ω-cm with a Hall mobility of 0.538 cm^2/Vs and a carrier concentration of $7.37x10^{19}$ cm^{-3}. Moreover, the apparent optical bandgap can be tuned from 4.51 to 4.32 eV upon increase the film thickness from 120 to 953 nm. We suggested that the degradation of crystallinity played a more crucial role in narrowing the bandgap of IMZO films.

Transparent *p-n* heterojunction composed of *p*-type LNO and *n*-type IMZO films with bandgap engineering of *n*-IMZO layer have been fabricated on MgO(001) substrate. The XRD measurements revealed that cube-on-cube epitaxial relationship of LNO(001)||IMZO(001)||MgO(001) was obtained. Upon increase of the In content in the *n*-IMZO layer, lattice mismatch between LNO and IMZO increases from 1.7 to 4.8 %. These enlargements in lattice mismatch greatly increase the density of dislocations and defects at the interfaces, which in turn increases the probabilities of electron scattering. The resultant *p-n* junction exhibit typical *I-V* behaviors with good rectifying characteristics. By increasing the In content of *n*-IMZO layer, the heterojunctions lead to higher threshold voltage due to the higher built-in potential generated by the change of the Fermi-level of *n*-type IMZO. Moreover, the ideality factor in the low voltage regions increases from 2.54 to 4.01. Such increase in the ideality factors are attributed to the larger lattice mismatch between LNO and IMZO layers, which increases the probability of defect-assisted tunneling and carrier recombination in the space charge

region via interfaces states. In the temperature dependent *I-V* characteristics, the current transportation mechanism is dominated by the tunneling through the barrier or the generation-recombination process occurring in the depletion region. Besides the electrical properties, we are also interested in the development of UV detector. Solar blind UV photodetector with peak spectral response at wavelength 320 nm has been realized based on the *p*-LNO/*n*-IMZO heterojunction. This photodetector shows a UV/visible rejection ratio of more than 40 under back-side illumination configuration. Upon increasing In content in *n*-type layer, the fitting peak of optical responsivity shifts from 307nm to 315nm.

The epitaxial growth of *p*-LNO/*n*-IMZO heterojunctions were prepared on TiN buffered Si by PLD. All *p*-LNO/*n*-IMZO junctions exhibited better rectifying characteristics than those grown on MgO substrate, such as higher current rectifying ratio, lower series resistance and lower leakage current. Moreover, their structural and electrical properties of the heterojunction grown on TiN buffered Si can be effectively tuned by bandgap engineering of *n*-IMZO layer. With higher In content in the *n*-IMZO layer, the electrical resistivity and the bandgap are reduced. These lead to higher current rectifying ratio, higher threshold voltage and higher leakage current in the bias voltage of -4V. Such IMZO based *p-n* heterojunctions are promising candidates for the development of low-cost and high electrical performance integrated optoelectronic devices.

The successful fabrication of MZO and IMZO films with high quality, single cubic phase, excellent epitaxy and high transparency are an important step towards implementation of ZnO-based heterojunctions in the electronic and optoelectronic applications. The potential for cubic phase TCO based on IMZO film is definitely an advantage for allowing heteroepitaxial growth of many oxides, such as perovskites and

transition metal monoxides. At the present stage, the electrical performance of these cubic phase TCOs have lots of room for improvement. Also, the fabrication of *p*-type MZO with cubic phase has not yet been attempted. The *p-n* homojunction based on c-MZO will be very useful for developing high quality of UV detector, blue and UV LED. The cubic phase of MZO homostructure gives out the parallel set of crystal planes allowing the formation of natural optical resonator for laser. Further investigation of c-MZO may ultimately lead to blue/UV laser that gives superior performance than the hexagonal-structure-based GaN laser.

References

[1.1] A. Nielsen, A. Brandlmaier, M. Althammer, W. Kaiser, M. Opel, J. Simon, W. Mader, S. T. B. Goennenwein, and R. Gross, Appl. Phys. Lett. **93**, 162510 (2008).

[1.2] J. H. Kim, H. J. Kim, D. J. Kim, Y. E. Ihm, W. K. Choo, J. Eur. Ceram. Soc., v **24**, n 6, p 1847-51, 2004.

[1.3] A. G. Zaitsev, R. Schneider, J. Geerk, G. Linker, F. Ratzel, and R. Smithey, Appl. Phys. Lett. **75**, 4165 (1999).

[1.4] X. D. Wu, S. R. Foltyn, P. N. Arendt, W. R. Blumenthal, I. H. Campbell, J. D. Cotton, J. Y. Coulter, W. L. Hults, M. P. Maley, H. F. Safar, and J. L. Smith, Appl. Phys. Lett. **67**, 2397 (1995).

[1.5] X. D. Wu, S. R. Foltyn, P. Arendt, J. Townsend, C. Adams, I. H. Campbell, P. Tiwari, Y. Coulter, and D. E. Peterson, Appl. Phys. Lett. **65**, 1961 (1994).

[1.6] L. Leontie, I. Evtodiev, V. Nedeff, M. Stamate, and M. Caraman, Appl. Phys. Lett. **94**, 071903 (2009).

[1.7] C. L. Yuan, P. Darmawan, Y. Setiawan, P. S. Lee, Nanotechnology, **17**, 3175 (2006).

[1.8] S. W. Jung, S. -J. An, G. Yi, C. U. Jung, S. Lee and S. Cho, Appl. Phys. Lett **80**, 4561 (2002).

[1.9] T. Andrearczyk, J. Jaroszynski, G. Grabecki, T. Dietl, T. Fukumura and M. Kawasaki, Phys. Rev. B, **72**, 121309 (2005).

[1.10] S. Sadofev, S. Kalusniak, J. Puls, P. Schafer, S. Blumstengel, and F. Henneberger, Appl. Phys. Lett. **91**, 231103 (2007).

[1.11] T. V. Shubina, A. A. Toropov, O. G. Lublinskaya, P. S. Kop’ev, S.V. Ivanov, A. El-Shaer,M. Al-Suleiman, A. Bakin, A.Waag, A.Voinilovich, E.V. Lutsenko, G. P.Yablonskii, J. P. Bergman, G. Pozina, and B. Monemar, Appl. Phys. Lett. **91**, 201104 (2007).

[1.12] S. Choopun, R. D. Vispute,W. Yang, R. P. Sharma, T. Venkatesan, and H. Shen, Appl. Phys. Lett. **80**, 1529 (2002).

[1.13] C. H. Bates,W. B. White, and R. Roy, Science **137**, 933 (1962).

[1.14] B. O'Neill, in Indium: Markets, Applications and Alternatives, Minor Metals 2005, Lisbon, Portugal, 2005.

[1.15] D.W. Palmer, http://www.semiconductors.co.uk/propiivi5410.htm, January, 2006.

[1.16] National Compound Semiconductor Roadmap/compound semiconductor materials,http://www.onr.navy.mil/sci_tech/information/312_electronics/ncsr/properties.asp, January, 2006.

[1.17] J. D. Albrecht, P. P. Ruden, S. Limpijumnong, W. R. L. Lambrecht, and K. F. Brennan, J. Appl. Phys. **86,** 6864 (1999).

[1.18] J.M. Adams, J. Fu, G. L. Catchen, and D. L. Miller, Appl. Phys. Lett. **61**, 2668 (1992).

[1.19] P. Yu, Z. K. Tang, G. K. L. Wong, M. Kawasaki, A. Ohtomo, H. Koinuma, Y. Segawa, J. Cryst. Growth **184/185**, 601 (1998).

[1.20] A. F. Kohan, G. Ceder, D. Morgan, and C. G. Van de Walle, Phys. Rev. B **61**, 15019 (2000).

[1.21] S. B. Zhang, S. H. Wei, and Alex Zunger, Phys. Rev. B **63**, 075205 (2001).

[1.22] D. C. Look, J. W. Hemsky, and J. R. Sizelove, Phys. Rev. Lett. **82**, 2552 (1999).

[1.23] K. Sakurai, T. Kubo, D. Kajita, T. Tanabe, H. Takasu, S. Fujita, and S. Fujita, Jpn. J. Appl. Phys. **39**, 1146 (2000).

[1.24] A. Ohtomo, M. Kawasaki, T. Koida, K. Masubuchi, H. Koinuma, Y. Sakurai, Y. Yoshida, T. Yasuda, and Y. Segawa, Appl. Phys. Lett. **72**, 2466 (1998).

[1.25] T. Minemoto, T. Negami, S. Nishiwaki, H. Takakura, and Y. Hamakawa, Thin Solid Films **372**, 173 (2000).

[1.26] A. K. Sharma, J. Narayan, J. F. Muth, C. W. Teng, C. Jin, A. Kvit, R. M. Kolbas, and O. W. Holland, Appl. Phys. Lett. **75**, 3327 (1999).

[1.27] W. I. Park, G. C. Yi, and H. M. Jang, Appl. Phys. Lett. **79**, 2022 (2001).

[1.28] T. Makino, Y. Segawa, A. Tsukazaki, A. Ohtomo, and M. Kawasaki, Appl. Phys. Lett. **93**. 121907 (2008).

[1.29] R. D. Shannon, Acta Crystallogr., Sect. A: Cryst. Phys., Diff., Theor. Gen. Crystallogr. **32**, 751 (1976).

[1.30] J .F. Sarver, Fred L. Katnack, and F. A. Hummel, J. Electrochem. Soc. **106**, 960 (1959).

[1.31] I. Takeuchi, W. Yang, K.-S. Chang, M.A. Aronova, T. Venkatesan, R.D. Vispute and L.A. Bendersky, J. Appl. Phys. **94** (2003) 7336.

[1.32] L. Zhuang, K. H.Wong, and G. K. H. Pang, Appl. Phys. A **89**, 543 (2007).

[1.33] W. Yang, S.S. Hullavarad, B. Nagaraj, I. Takeuchi, R.P. Sharma, T. Venkatesan, R.D. Vispute and H. Shen, Appl. Phys. Lett. **82** (2003) 3424.

[1.34] J. Narayan, A. K. Sharma, A. Kvit, C. Jin, J. F. Muth, O. W. Holland, Solid State Commun., **121**, 9, (2001).

[1.35] R. Schmidt, B. Rheinlander, M. Schubert, D. Spemann, T. Butz, J. Lenzner, E.M. Kaidashev, M. Lorenz, A. Rahm, H.C. Semmelhack, M. Grundmann, Appl. Phys. Lett. **82** (2003) 2260.

[1.36] H. Ohta, K. Kawamura, M. Orita, M. Hirano, N. Sarukura and H. Hosono, Appl. Phys. Lett. **77**, 475 (2000).

[1.37] P. Chen, X. Ma and D. Yang, J.Appl. Phys. **101** 053103 (2007).

[1.38] X. W. Sun, J. L. Zhao, S. T. Tan, L. H. Tan, C. H. Tung, G. Q. Lo, D. L. Kwong,

Y. W. Zhang, X. M. Li, and K. L. Teo, Appl. Phys. Lett. **92**, 111113 (2008).

[1.39] S. Mridha, and D. Basak, J.Appl. Phys. **101** 083102 (2007).

[1.40] M. Dutta, and D. Basak, Appl. Phys. Lett. **92**, 212112 (2008).

[1.41] Z. Guo, D. Zhao, Y. Liu, D. Shen, J. Zhang, and B. Li, Appl. Phys. Lett. **93**, 163501 (2008).

[1.42] W. Yang, R. D. Vispute, S. Choopun, R. P. Sharma, T. Venkatesan, and H. Shen, Appl. Phys. Lett. **78**, 2787 (2001).

[1.43] Z. G. Ju, C. X. Shan, D. Y. Jiang, J. Y. Zhang, B. Yao, D. X. Zhao, D. Z. Shen, and X. W. Fan, Appl. Phys. Lett. **93**, 173505 (2008).

[2.1] J. T. Cheung, I. Gergis, M. James, and R. E. DeWames, Appl. Phys. Lett. **60**, 3180 (1992).

[2.2] R. D. Vispute, R. Chowdhury, P. Tiwari, and J. Narayan, Appl. Phys. Lett. **65**, 2565 (1994).

[2.3] R. Ramesh, K. Luther, B. Wilkens, D. L. Hart, E. Wang, J. M. Tarascon, A. Inam, X. D. Wu, and T. Venkatesan, Appl. Phys. Lett. **57**, 1505 (1990).

[2.4] N. J.Seong, S. G.. Yoon, Y. H. Jo, M. H. Jung, C. R. Cho, Appl. Phys. Lett. **89**, 162109 (2006).

[3.1] S. Sadofev, S. Kalusniak, J. Puls, P. Schafer, S. Blumstengel, and F. Henneberger, Appl. Phys. Lett. **91**, 231103 (2007).

[3.2] T. V. Shubina, A. A. Toropov, O. G. Lublinskaya, P. S. Kop'ev, S.V. Ivanov, A. El-Shaer,M. Al-Suleiman, A. Bakin, A.Waag, A.Voinilovich, E.V. Lutsenko, G. P.Yablonskii, J. P. Bergman, G. Pozina, and B. Monemar, Appl. Phys. Lett. **91**, 201104 (2007).

[3.3] S. Choopun, R. D. Vispute,W. Yang, R. P. Sharma, T. Venkatesan, and H. Shen, Appl. Phys. Lett. **80**, 1529 (2002).

[3.4] Z. G. Ju, C. X. Shan, D. Y. Yiang, J. Y. Zhang, B. Yao, D.X. Zhao, D. Z. Shen and X. W. Fan, Appl. Phys. Lett. **93**, 173505 (2008).

[3.5] H. Long, G. Fang, H. Huang, X. Mo, W. Xia, B. Dong, X. Meng, and X. Zhao, Appl. Phys. Lett. **95**, 013509 (2009).

[3.6] L. Zhuang, K. H.Wong, and G. K. H. Pang, Appl. Phys. A **89**, 543 (2007).

[3.7] C. H. Lau, L. Zhuang, and K. H. Wong, Phys. Status Solidi B **244**, 1533 (2007).

[3.8] R. D. Shannon**,** Acta Crystallographica. **32**, 751 (1976).

[3.9] I. Volintiru, M. Creatore, B. J. Kniknie, C. I. M. A. Spee, and M. C. M. van de Sanden, J. Appl. Phys. **102**, 043709 (2007).

[3.10] M. Chen, X. Wang, Y. H. Yu, Z. L. Pei, X. D. Bai, C. Sun, R. F. Huang, and L. S. Wen, Appl. Surf. Sci. **158**, 134 (2000).

[3.11] C. Agashe, O. Kluth, J. Hüpkes, U. Zastrow, B. Rech, and M. Wuttig, J. Appl. Phys. **95**, 1911 (2004).

[3.12] J. H. Ko, I. H. Kim, D. Kim, K. S. Lee, T. S. Lee, B. Cheong, and W. M. Kim, Appl. Surf. Sci. **253**, 7398 (2007).

[3.13] S. Liang, X. F. Bi, J. Appl. Phys. 104, 113533 (2008).

[3.14] H. Ohta, M.Orita, M. Hirano, H. Tanji, H. Kawazoe, and H. Hosono, Appl. Phys. Lett. **76**, 2740 (2000).

[4.1] C. Heske, U. Groh, L. Weinhardt, O. Fuchs, B. Holder, E. Umbach, C. Bostedt, L. J. Terminello, S. Zweigart, T. P. Niesen, and F. Karg, Appl. Phys. Lett. **81**, 4550 (2002).

[4.2] S. Ishizuka, A. Yamada, K. Matsubara, P. Fons, K. Sakurai, and S. Niki, Appl. Phys. Lett. **93**, 124105 (2008).

[4.3] T. Nakada and A. Kunioka, Appl. Phys. Lett. **74**, 2444 (1999).

[4.4] Q. Wan, E. N. Dattoli, and W. Lu, Appl. Phys. Lett. **90**, 222107 (2007).

[4.5] T. W. Kim, D. U. Lee, D. C. Choo, and Y. S. Yoon, Appl. Phys. Lett. **79**, 2187 (2001).

[4.6] Y. J. Lin , J. H. Hong, Y. C. Lien, and B.Y. Liu, Appl. Phys. Lett. **89**, 262110 (2006).

[4.7] F. Ghebremichael, C. Poga, and M. G. Kuzyk, Appl. Phys. Lett. **66**, 139 (1995).

[4.8] H. F. Zhang, C. X. Lei, H. F. Liu, and C. K. Yuan, J. Semicond. **30**, 043004 (2009).

[4.9] B. D. Ahn, S. H. Oh, H. J. Kim, M. H. Jung, and Y. G. Ko, Appl. Phys. Lett. **91**, 252109 (2007).

[4.10] S. Liang, and X. Bi, J. Appl. Phys **104**, 113533 (2008).

[4.11] T. Minami, S. Suzuki, and T. Miyata, Mater. Res. Soc. Symp. Proc. **666**, F1.3.1 (2001).

[4.12] T. Pisarkiewics, K. Zakrzewska, and E. Leja, Thin Solid Films **174**, 271 (1989).

[4.13] E. Burstein, Phys. Rev. **93**, 632 (1954).

[4.14] T. S. Moss Proc. Phys. Soc. London, Sect. B **67**, 775 (1954).

[5.1] L. Chen, Z. Ye, S. Lin, H. He, Y. Zeng, B. Zhao and L. Zhu, Materials Letters, vol. In Press, Accepted Manuscript,

[5.2] W. Jun and Y. Yintang, Materials Letters. **62**, 1899 (2008).

[5.3] Y. F. Li, B. Yao, Y. M. Lu, Z. P. Wei, Y. Q. Gai, C. J. Zheng, Z. Z. Zhang, B. H. Li, D. Z. Shen, X. W. Fan and Z. K. Tang, Appl. Phys. Lett. **91**, 232115 (2007).

[5.4] M. Oh, D. Hwang, Y. Choi, J. Kang, S. Park, C. Hwang and K. I. Cho, Appl. Phys. Lett. **93**, 111905 (2008).

[5.5] M. X. Qiu, Z. Z. Ye, H. P. He, Y. Z. Zhang, X. Q. Gu, L. P. Zhu and B. H. Zhao,

Appl. Phys. Lett. **90**, 182116 (2007).

[5.6] K. Tang, S. Gu, S. Zhu, W. Liu, J. Ye, J. Zhu, R. Zhang, Y. Zheng and X. Sun, Appl. Phys. Lett. **93**, 132107, (2008).

[5.7] H. Kawazoe, M. Yasukawa, H. Hyodo, M. Kurita, H. Yanagi, and H. Hosono, Nature (London) **389**, 939 (1997).

[5.8] H. Yanagi, S. Inoue, K. Ueda, H. Kawazoe, and H. Hosono, J. Appl. Phys. **88**, 4159 (2000).

[5.9] K. Ueda, T. Hase, H. Yanagi, H. Kawazoe, H. Hosono, H. Ohta, M. Orita, and M. Hirano, J. Appl. Phys. **89**, 1790(2001).

[5.10] H. Yanagi, H. Kawazoe, A. Kudo, M. Yasukawa, and H. Hosono, J. Electroceram. **4**, 427 (2000).

[5.11] A. Kudo, H. Yanagi, H. Hosono, and H. Kawazoe, Appl. Phys. Lett. **73**, 220 (1998).

[5.12] H.ohta, M.Hirano, K. Nakaara, H. Maruta, T. Tanabe, M. Kamiya, T. Kamiya, and H. Hosono, Appl. Phys. Lett. **83**, 1029 (2003).

[5.13] E. Antolini, Mater. Chem. and Phys. **82**, 937(2003).

[5.14] T. Kamiya, H. Ohta, M. Kamiya, K. Nomura, K. Ueda, M. Hirano, and H. Hosono, J. Mater. Res. **19**, 913 (2004).

[5.15] H. Ohta, K. Kawamura, M. Orita, M. Hirano, N. Sarukura, and H. Hosono, Appl. Phys. Lett. **77**, 475 (2000).

[5.16] H. Ohta, H. Mizoguchi, M. Hirano, S. Narushima, T. Kamiya, and H. Hosono, Appl. Phys. Lett. **82**, 823 (2003).

[5.17] K. Tonooka, H. Bando and Y. Aiura, Thin Solid Films. **445**, 327 (2003).

[5.18] K. Tonooka and N. Kikuchi, Thin Solid Films. **515**, 2415 (2006).

[5.19] A. Kudo, H. Yanagi, K. Ueda, H. Hosono, H. Kawazoe, and Y. Yano, Appl. Phys. Lett. **75**, 2851 (1999).

[5.20] J. B. Fedison, T. P. Chow, H. Lu, and I. B. Bhat, Appl. Phys.Lett. **72**, 2841 (1998).

[5.21] S. Majumdar and P. Banerji, J. Appl. Phys. **105**, 043704 (2009).

[5.22] S. Mridha and D. Basak, Semicond. Sci. Technol. **21**. 928 (2006).

[5.23] C.-x. Wang, G.-W. Yang, H.-W.Liu, Y.-H. Han, J.-F. Luo, C.-X. Gao, and G.-T. Zou, Appl. Phys. Lett. **83**, 4854 (2003).

[5.24] A. Ruotolo, C.Y. Lam, W.F. Cheng, K.H. Wong and C.W. Leung, Phys. Rev. B,**76**, 075122 (2007).

[6.1] A. Ohtomo, M. Kawasaki, T. Koida, K. Masubuchi, H. Koinuma, Y. Sakurai, Y. Yoshida, T. Yasuda, and Y. Segawa, Appl. Phys. Lett. **72**, 2466 (1998).

[6.2] S. Sadofev, S. Kalusniak, J. Puls, P. Schafer, S. Blumstengel, and F. Henneberger, Appl. Phys. Lett. **91**, 231103 (2007).

[6.3] T. V. Shubina, A. A. Toropov, O. G. Lublinskaya, P. S. Kop'ev, S.V. Ivanov, A. El-Shaer,M. Al-Suleiman, A. Bakin, A.Waag, A.Voinilovich, E.V. Lutsenko, G. P.Yablonskii, J. P. Bergman, G. Pozina, and B. Monemar, Appl. Phys. Lett. **91**, 201104 (2007).

[6.4] Y. Lin, P. Wu, C. Tsai, C. Liu, Z. Lin, H. Chang, and C. Lee, J. Appl. Phys. **103**, 113709 (2008).

[6.5] M. H. Huang, S. Mao, H. Feick, H. Q. Yan, Y. Y.Wu, H. Kind, E. Weber, R. Russo, and P. Yang, Science **292**, 1897 (2001).

[6.6] D. C. Look, Mater. Sci. Eng. B **80**, 383 (2001).

[6.7] K.W. Liu, J. G. Ma, J.Y. Zhang,Y. M. Lu, D.Y. Jiang, B. H. Li, D. X. Zhao, Z. Z. Zhang, B. Yao, and D. Z. Shen, Solid-State Electron. **51**, 757 (2007).

[6.8] T. Minami, Thin Solid Films **516**, 1314 (2008).

[6.9] K. H.Wong and Y. S. Leung, Thin Solid Films **354**, 52 (1999).

[6.10] S. Choopun, R. D. Vispute,W. Yang, R. P. Sharma, T. Venkatesan, and H. Shen, Appl. Phys. Lett. **80**, 1529 (2002).

[6.11] C. H. Bates,W. B. White, and R. Roy, Science **137**, 933 (1962).

[6.12] L. Zhuang, K. H.Wong, and G. K. H. Pang, Appl. Phys. A **89**, 543 (2007).

[6.13] C. H. Lau, L. Zhuang, and K. H. Wong, Phys. Status Solidi B **244**, 1533 (2007).

[6.14] F. J. Morin, Phys. Rev. **93**, 1199 (1954).

[6.15] W. Shin and N. Murayama, Jpn. J. Appl. Phys., Part 2 **38**, L1336 (1999).

[6.16] J. Narayan, P. Tiwari, X. Chen, J. Singh, R. Chowdhury, and T. Zheleva, Appl. Phys. Lett. **61**, 1290 (1992).

[6.17] M. B. Lee, M Kawasaki, M. Yoshimoto, and H. Koinuma, Appl. Phys. Lett. **66**, 1331 (1995).

[6.18] Y. R. Ryu, T. S. Lee, J. H. Leem, and H. W. White,Appl. Phys. Lett. **83**, 4032(2003).

[6.19] H. Ohta, K. Kawamura, M. Orita, M. Hirano, N. Sarukura, and H. Hosono, Appl. Phys. Lett. **77**, 475 (2000).

[6.20] H. Ohta, H. Mizoguchi, M. Hirano, S. Narushima, T. Kamiya, and H. Hosono, Appl. Phys. Lett. **82**, 823 (2003).

[6.21] K. Tonooka, H. Bando and Y. Aiura, Thin Solid Films. **445**, 327 (2003).

[6.22] K. Tonooka and N. Kikuchi, Thin Solid Films. **515**, 2415 (2006).

[6.23] A. Kudo, H. Yanagi, K. Ueda, H. Hosono, H. Kawazoe, and Y. Yano, Appl. Phys. Lett. **75**, 2851 (1999).

[6.24] Y. R. Ryu, W. J. Kim, and H. W. White, J. Cryst. Growth **219**, 419 (2000).